

# Mitigation Techniques for the Impact of Weather and Atmosphere in Satellite FSO Communications

Nguyen Van Thang

A DISSERTATION

SUBMITTED IN PARTIAL FULFILLMENT OF THE REQUIREMENTS

FOR THE DEGREE OF DOCTOR OF PHILOSOPHY

IN COMPUTER SCIENCE AND ENGINEERING

Graduate Department of Computer and Information Systems

The University of Aizu

2022



© Copyright by Nguyen Van Thang

All Rights Reserved

The thesis titled  
Mitigation Techniques for the Impact of Weather and Atmosphere in Satellite FSO  
Communications


by  
Nguyen Van Thang

is reviewed and approved by

Chief Referee

Professor

PHAM Tuan Anh

*Pham T. Anh* 

Professor

TEI Shigaku

*Zixue Cheng* 

Senior Associate Professor

LI Peng

*Peng Li* 

Senior Associate Professor

LU Guo-Wei

*Lu Guo-Wei* 

The University of Aizu

2022



# Contents

Contents . . . . .	v
List of Figures . . . . .	xi
List of Notations . . . . .	xiv
List of Abbreviations . . . . .	xv
Acknowledgement . . . . .	xvii
Abstract . . . . .	xix
1. Introduction . . . . .	1
1.1 An Overview of Optical Satellite Systems . . . . .	1
1.2 Motivations . . . . .	3
1.3 Original Contributions . . . . .	5
1.4 Dissertation Organization . . . . .	7
2. Background of Study . . . . .	10
2.1 Satellite Communications . . . . .	10
2.1.1 History of Satellite Communications . . . . .	11
2.1.2 Satellite Orbit Classification . . . . .	12
2.1.3 Different Satellite Communication Systems . . . . .	14
2.1.3.1 Inter-Satellite Communications . . . . .	15

2.1.3.2	Satellite-to-High-Altitude Platform (HAP) . . . . .	16
2.1.3.3	Satellite-to-Unmanned Aerial Vehicle (UAV) . . . . .	17
2.1.3.4	Satellite-to-Ground Station (GS) . . . . .	18
2.2	FSO in Satellite Communications . . . . .	19
2.2.1	History and Current Development . . . . .	19
2.2.2	Laser Transmitter . . . . .	21
2.2.3	Photodetectors and Receiver Architectures . . . . .	22
2.2.4	Acquisition, Tracking, and Pointing Mechanisms . . . . .	23
2.2.5	Field of View . . . . .	24
2.2.6	Modulation . . . . .	25
2.2.7	Link Budget . . . . .	26
2.2.8	Operating Wavelength . . . . .	27
2.3	FSO Channel in Satellite Communications . . . . .	28
2.3.1	Vertical Versus Horizontal FSO Channels . . . . .	28
2.3.2	Atmospheric Attenuation . . . . .	29
2.3.3	Geometric and Misalignment Losses . . . . .	32
2.3.4	Cloud Attenuation . . . . .	33
2.3.5	Atmospheric Turbulence Induced Fading . . . . .	35
2.4	Performance Improvement Techniques . . . . .	38
2.4.1	Relay Transmission . . . . .	38
2.4.2	Hybrid FSO/RF . . . . .	40
2.4.3	Rate Adaptation . . . . .	42
2.4.4	Diversity Technique . . . . .	44
2.5	Summaries . . . . .	45
3.	Rate Adaptation for Satellite Hybrid FSO/RF System . . . . .	46
3.1	Introduction . . . . .	47

3.2	System Descriptions . . . . .	50
3.3	Channel Modeling . . . . .	53
3.3.1	Satellite-to-HAP FSO link . . . . .	53
3.3.2	HAP-to-UAV hybrid FSO/RF link . . . . .	54
3.3.2.1	RF channel . . . . .	54
3.3.2.2	FSO channel . . . . .	55
3.4	Rate Adaptation Design . . . . .	60
3.4.1	Adaptive Transmission Schemes . . . . .	60
3.4.2	Performance Analysis . . . . .	64
3.4.3	Conventional Hybrid FSO/RF Design . . . . .	66
3.5	Numerical Results . . . . .	67
3.6	Conclusions . . . . .	73
4.	RIS-UAV Relay Assisted SAGIN . . . . .	75
4.1	Introduction . . . . .	76
4.1.1	Related Work and Motivation . . . . .	78
4.1.2	Major Contributions and Novelty . . . . .	79
4.2	System Description . . . . .	81
4.2.1	Hybrid FSO/RF-based Satellite-HAP-GS System . . . . .	81
4.2.2	Proposal of FSO-based RIS-UAV Relay . . . . .	84
4.2.3	Link Switching and Multi-Rate Adaptation Design . . . . .	85
4.2.3.1	Link Switching Scheme . . . . .	85
4.2.3.2	Multi-Rate Adaptation Design . . . . .	88
4.3	Channel Modeling . . . . .	89
4.3.1	FSO-based Satellite-to-HAP Link . . . . .	89
4.3.2	Hybrid FSO/RF-based HAP-to-GS Link . . . . .	90
4.3.2.1	RF Channel . . . . .	90

4.3.2.2	FSO Channel . . . . .	91
4.3.3	UAV-Assisted HAP-to-GS FSO Link . . . . .	93
4.3.4	End-to-End Channel Statistical Model . . . . .	97
4.4	Performance Analysis . . . . .	99
4.4.1	Transmission Mode Selection Probability . . . . .	99
4.4.2	Performance Metrics . . . . .	102
4.4.2.1	Outage Probability . . . . .	102
4.4.2.2	Average Transmission Rate . . . . .	103
4.4.2.3	Spectral Efficiency . . . . .	103
4.5	Numerical Results and Discussions . . . . .	104
4.5.1	Outage Performance . . . . .	104
4.5.2	Average Transmission Rate and Spectral Efficiency . . . . .	107
4.5.3	Design Guidelines . . . . .	111
4.6	Conclusions . . . . .	113
5.	Site Diversity Technique . . . . .	114
5.1	Introduction . . . . .	114
5.2	Network Descriptions . . . . .	116
5.2.1	Cloud Attenuation . . . . .	117
5.2.2	Atmospheric Turbulence . . . . .	118
5.3	Performance Analysis . . . . .	118
5.3.1	Power Loss . . . . .	118
5.3.2	Link Availability . . . . .	119
5.3.3	Site Diversity Technique . . . . .	119
5.4	Results and Discussions . . . . .	120
5.4.1	Impact of Clouds on Link Availability . . . . .	120
5.4.2	Joint Impact of Clouds and Atmospheric Turbulence . . . . .	120
5.5	Conclusions . . . . .	121



6. Summaries and Future Research . . . . .	123
6.1 Summaries . . . . .	123
6.2 Future Research . . . . .	124
Bibliography . . . . .	127



# List of Figures

1.1	The applications of satellite communications. . . . .	3
1.2	The contributions of the dissertation. . . . .	5
1.3	Dissertation structure. . . . .	7
2.1	Optical satellite communications. . . . .	12
2.2	An example of architecture for space-air-ground integrated network [1].	14
2.3	Experiment system configuration of optical inter-orbit communications [2].	15
2.4	(a) Stratospheric flight terminal with the periscope-type coarse pointer, (b) stratospheric balloon during launch preparations for CAPANINA, and (c) near-infrared photograph of flight terminal below stratospheric balloon [3]. . . . .	16
2.5	Satellite-to-UAV communications: (a) Use cases and (b) UAV classification.	17
2.6	Bidirectional Laser Communication Between Space and Ground Station [4].	18
2.7	Basic diagram of a generic FSO system [5]. . . . .	22
2.8	Block diagram of an ATP mechanism designed for FSO communications [6].	23
2.9	Field of view of a generic optical-communication system defined by its focal length $f$ and photodetector of size $d$ [6]. . . . .	24
2.10	Typical responsivity versus wavelength for silicon (Si), InGaAs, and germanium (Ge) [6]. . . . .	27

2.11	A different channel model comparison between vertical and horizontal FSO links. . . . .	29
2.12	Effect of water vapour, molecular scattering, and aerosol scattering over different optical wavelength [5]. . . . .	30
2.13	Scattering phenomenons: (a) Rayleigh scattering and (b) Mie scattering.	31
2.14	(a) Without misalignment and (b) with misalignment between the center of the optical beam footprint and receiver detector. . . . .	32
2.15	An example of global map of the fraction of sky covered by clouds. . . . .	33
2.16	Relay transmission configuration: (a) Serial relay (b) Parallel relay [7]. . . . .	39
2.17	Hybrid FSO/RF system block diagram. . . . .	40
2.18	An example of the rate adaptation design for FSO-based satellite system.	42
2.19	The flowchart of rate adaption for the hybrid FSO/RF system. . . . .	43
3.1	HAP-assisted satellite network with UAVs. . . . .	48
3.2	The dual-hop satellite-HAP-UAV hybrid FSO–FSO/RF systems including challenge issues (left side) and block diagram (right side). . . . .	51
3.3	An example of the visibility for several cloud types. . . . .	56
3.4	UAV hovering misalignment model. . . . .	58
3.5	Outage performance versus satellite’s transmitted power for different CLWCs at the UAV’s position of 20 m. . . . .	66
3.6	Outage probability versus satellite transmit power and distance from center of Gaussian beam to UAV position with CLWC of 6 mg/m <sup>3</sup> . . . . .	70
3.7	The impact of cloud to average transmission rate of adaptive rate system and fixed rate system. . . . .	70
3.8	The achievable spectrum efficiency versus satellite transmit power in the case of adaptive rate system and fixed rate system. . . . .	71
3.9	Average BER and average transmission rate versus UAV’s position for different values of HAP’s divergence angle. . . . .	71

4.1	The proposal of HAP-based SAGIN using hybrid FSO/RF with temporarily optical RIS-UAV relay solution. . . . .	77
4.2	Integrated space-aerial-terrestrial hybrid FSO/RF system block diagram.	82
4.3	Beam reflect-and-forward by RIS mounted on UAV. . . . .	94
4.4	Selected mode probability vs. CLWC values for different transmission links with $P_t = 11$ dBm, $M_c^{\text{th}} = 10.3$ mg/m <sup>3</sup> , and $N_1 = N_2 = N_3 = 2$ modes. . . . .	101
4.5	Outage performance of the primary FSO-FSO1 link versus CLWC for different satellite's transmitted powers. . . . .	104
4.6	Outage performance of different systems versus CLWC, when $P_t = 7$ dBm.	106
4.7	Outage performance versus GS's aperture radius for different satellite's transmitted powers and HAP's zenith angles. . . . .	107
4.8	Average transmission rate of different systems versus CLWC, when $P_t = 11$ dBm. . . . .	108
4.9	Average transmission rate versus CLWC for (i) fixed rate and (ii) adaptive rate on FSO-FSO2 link, when $P_t = 11$ dBm. . . . .	109
4.10	Average transmission rate versus CLWC for different UAV's altitudes, when $P_t = 11$ dBm. . . . .	110
4.11	Average spectral efficiency of different systems versus CLWC, when $P_t = 11$ dBm. . . . .	111
5.1	Site diversity implementation in Japan [8]. . . . .	115
5.2	Satellite downlinks with multiple ground stations. . . . .	117
5.3	Link availability in Japan during rainy season. . . . .	121
5.4	Link availability (a) without site diversity, (b) with site diversity. . . . .	122

# List of Notations

$\sec(x)$	Corresponding to $\cos^{-1}(x)$ for a scalar $x$
$\mathbb{E}(\cdot)$	The average value
$I_0(\cdot)$	The modified Bessel function of the first kind with order zero
$\mathcal{N}(\mu, \sigma^2)$	A Gaussian distribution with mean $\mu$ and variance $\sigma^2$
$\operatorname{erfc}(x)$	The complementary error function, $\operatorname{erfc}(x) \triangleq \frac{2}{\sqrt{\pi}} \int_x^\infty e^{-t^2} dt$
$\operatorname{erf}(x)$	The error function, $\operatorname{erf}(x) = 1 - \operatorname{erfc}(x)$

# List of Abbreviations

3GPP	3rd Generation Partnership Project
AF	Amplify-and-Forward
AP	Adaptive Power
AR	Adaptive Rate
ARTEMIS	Advanced Relay Technology Mission Satellite
BER	Bit Error Rate
GS	Ground Station
CDF	Cumulative Distribution Function
CSI	Channel State Information
DF	Decode-and-Forward
DLR	German Aerospace Center
ESA	European Space Agency
FSO	Free Space Optics
Gbps	Gigabit- per-second
GEO	Geostationary Orbit
HAP	High Platform Altitude
IM/DD	Intensity Modulation/Direct Detection
ITU	International Telecommunications Union
LEO	Low Earth Orbit
MEO	Medium Earth Orbit
ML	Machine Learning
mmWave	Millimeter Wave
NASA	National Aeronautics and Space Administration
NGSO	Non-GeoStationary Orbit

NICT	National Institute of Information and Communications Technology
OICETS	Optical Inter-orbit Communications Engineering Test Satellite
PHY	Physical Layer
QoS	Quality of Service
RF	Radio Frequency
RIS	Re-configurable Intelligent Surface
SE	Spectral Efficiency
SI	Scintillation Index
SNR	Signal-to-noise Ratio
SOTA	Small Optical TrAnsponder
TBIRD	Terabyte Infrared Delivery
Tbps	Terabit-per-second
UAV	Unmanned Aerial Vehicle
UDN	Ultra-dense Network
VR	Virtual Reality



# Acknowledgement

This dissertation is not only a milestone of my life but also the result of many experiences I have encountered at the University of Aizu from dozens of remarkable individuals who I also wish to acknowledge.

First and foremost, I would like to express my deepest gratitude to my supervisor, Prof. PHAM T. Anh, for his support and constant encouragement throughout my Ph.D. study. I have no way to repay the patience, guidance, and great effort he put into training me, not only with the academic knowledge but also with everything in life, especially the marathon. It is an honor for me to study and research in Computer Communications Laboratory under his supervision.

I would like to extend my special appreciation and thanks to my doctoral dissertation review committee, Prof. TEI Shigaku, Prof. LI Peng, and Prof. LU Guo-Wei for providing insightful comments and suggestions to fulfill my research contributions.

A very special thank to Prof. DANG T. Ngoc, who always gives helpful advice and encourages me during my Ph.D. study. This dissertation would not have been possible without his efforts.

I also would like to extend my special appreciation and thanks to Dr. Thanh V. Pham and Dr. Hoang D. Le, who gave me a lot of valuable suggestions during my study. I really admire their meticulous attitude on research and enjoyed every discussion with them.

My sincere thanks go to my lab mates and members of the Aizu soccer club, whose help in daily life has been a key factor for successfully accomplishing this work.

I gratefully acknowledge the financial support from the University of Aizu, Aizu-wakamatsu Rotary club, SAISUA, Aizu Area Foundation.

Last but certainly not least, I take this opportunity to express my very profound

gratitude to my beloved family for their understanding, patience, support, and many years of selfless love. A special thank to my wife Nguyen Thi Thuy Hang and my son Nguyen Anh Khoi, for all their love and support. There are no word that can illustrate how lucky I am to have them in my life. I dedicate this dissertation to them.

# Abstract

A major challenge of existing telecommunication is how to extend connectivity at a reasonable cost to several billion users who did not have regular Internet access, especially in rural and remote areas where the ground network cannot properly work. In addition, with the data deluge in terms of global services and user equipment, the number of connected devices is expected to surpass 50 billion, which poses stringent burdens on the current telecommunications terrestrial infrastructure. Therefore, developing novel connectivity solutions to fulfill such enormous demands becomes indispensable. A recent trend for boosting terrestrial networks is by enabling connectivity from space. Towards this direction, optical satellite communication has emerged as an essential enabler for serving remote areas and enhancing the capacity of the existing wireless systems. Satellite-based free-space optical (FSO) communications address requirements of the existing wireless networks, such as spectrum scarcity in radio-frequency (RF) spectrum and the restricted coverage of terrestrial networks. The FSO connectives between satellites and Earth, however, are not without challenges. Various issues come from the physical layers, such as atmospheric attenuation, atmospheric turbulence-induced fading, weather-induced disruption, beam misalignment between transmitter (satellites) and receiver (fixed-ground station, moving vehicles). From this perspective, this dissertation aims to provide mitigation techniques that help enhance the performance of satellite-based FSO communication under the impact of weather and atmospheric conditions. In the design of satellite-based FSO systems, cloud blockage is a critical problem since the outage of optical links can severely deteriorate the system's availability. Firstly, driven by the development of pseudo-satellite, as known as a high-altitude platform (HAP), the relay transmission technique is proposed to avoid cloud coverage thanks to the flexible and quick deploy-

ment. Besides, a mirror array constructed by re-configurable intelligent surface (RIS) mounted on the unmanned aerial vehicle (UAV) is proposed to relay signals from HAP to user terminals. Secondly, a well-known technique, namely hybrid FSO/RF system, in terrestrial networks is proposed to use in satellite networks. In fact, FSO and RF are not affected in the same way under cloud attenuation due to their wavelength characteristics. In addition, we propose a rate adaptation design that avoids frequently switching between FSO link and RF link in the hybrid system, leading to improved system outage and maximizing the achievable average transmission rate. We also provide insightful discussions that can be helpful for the practical design of optical satellite communications. Finally, we propose a site diversity technique by linking more than two ground stations receiving the same signal from the satellite to improve the system performance.

# Chapter 1

## Introduction

### 1.1. An Overview of Optical Satellite Systems

Optical communication from space has developed tremendous progress over the years. Multiple companies (Starlink-SpaceX, Lightspeed-Telesat) participate in the optical satellite communication race aimed at establishing satellite-based free-space optical (FSO) to provide global broadband Internet access [9, 10]. For an inter-satellite link between two Low Earth Orbit (LEO) satellites (NFIRE and TerraSar-X), the successful error-free transmission can be achieved 5.6 Gbps [11, 12]. For two-way transmission, i.e., ground-to-satellite (uplink) and satellite-to-ground (downlink), Starlink's median upload and download speed can respectively reach 13.89 Mbps and 97.23 Mbps in 2021 (quarter 1) [13]. In the project TeraByte InfraRed Delivery (TBIRD) between NASA and MIT Lincoln Laboratory, LEO Cubesat is expected to transmit 200 Gbps in the optical downlink so that it could deliver more than 50 Terabytes of information per day to a ground station [14]. On the other hand, optical links are preferable to radio frequency (RF) links for space applications because of using huge optical frequency bands to transmit high data-rate over long distances [15]. In addition, FSO communication does not require any spectrum licensing and therefore, is an attractive prospect for high bandwidth and capacity applications such as high-

speed internet, video-conferencing, live streaming, etc. These enable the combination of FSO and satellite to be a promising solution to future communication networks.

Free space optical (FSO) is a technology that uses laser beam for data transfer over free-space channel. Due to operate in the infrared spectral range, FSO communication systems do not require operating licenses. Currently, the optical wavelength of 850 nm and 1550 nm are widely used in commercial FSO communication since they do not suffer much absorption from the atmosphere. A main requirement of FSO system is line-of-sight propagation owing to the optical beam cannot travel through solid obstacles (e.g., wall, trees). FSO systems can be classified into two types: terrestrial and non-terrestrial (aerial platform, space, and deep-space) [16]. In terrestrial system, FSO links can be established connection car-to-car or between two buildings [17]. In non-terrestrial system, depending on the purpose, FSO system can be implemented in a lot of scenarios. FSO-based satellite can directly deliver the broadband internet to inaccessible area and remote area [18]. FSO-based aerial systems (e.g., ground-to-HAP, HAP-to-HAP, HAP-to-UAV [19]) can quickly set up a temporary network for crowded events or internet of vehicle scenarios. In this dissertation, we focus on the non-terrestrial system.

Nowadays, the traffic demands increase due to the development of various emerging applications such as the Internet of Things (IoT), cloud computing, big data, and technologies for the next generation network [20]. Besides, the various scenarios require wireless access services with high data rates and reliability anywhere on the Earth. The terrestrial network cannot satisfy the issues mentioned above. It is obligatory to exploit the non-terrestrial network to accommodate various services and applications above. Figure 1.1 illustrates an example of the applications of satellite communications. Firstly, the satellite system can enable the *network scalability* due to providing wide coverage. Secondly, satellite systems can guarantee the *ubiquitous services* in inaccessible areas (e.g., desert, ocean, etc.) or underserved areas (e.g., rural and remote areas), where the ground communication system is challenging to deploy due to the expensive cost or impractical to reach. Thirdly, satellite communications

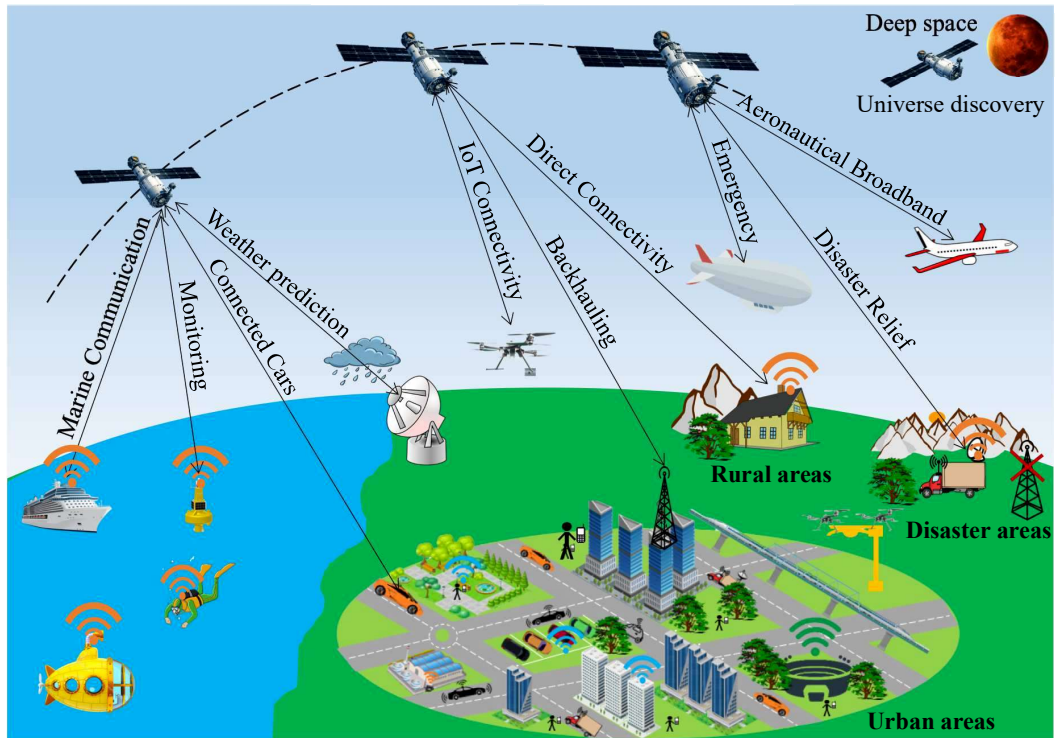


Figure 1.1: The applications of satellite communications.

can remarkably enhance the *network reliability* by offering uninterrupted connections for the areas that the ground network cannot support. For example, satellite communication systems can assist moving platforms (e.g., airplanes, high-speed trains, autonomous cars, etc.) or mission-critical communications (e.g., universe discovery). In addition, climate change is a current major theme of *emergency communications*, therein satellite-based disaster warning systems play a crucial role in predicting the weather and monitoring the Earth's environment, as presented in ITU strategic plan 2020-2023 [21].

## 1.2. Motivations

In recent years, communications from space have emerged as a potential solution for the provision of global vertical Internet access thanks to the advantages such as reasonable cost and service ubiquity. Additionally, the satellite communication race gears up, multiple companies have already declared tremendous plans to develop optical links from space. Several impressive optical from space projects can be listed

as SILEX (GEO-LEO link) transmits data rate of 50 Mbps with the distance of 45000 km in 2001 [22]. FALCON (VLEO-to-VLEO link) offers a high data rate of 2.5 Gbps at the altitude of 130 km in 2010 [23]. Stellar (LEO-to-LEO link) provides a data rate of 100 Mbps with the transmission distance of 1000 km in 2020 [24]. On the one hand, the proliferation of the new platforms has given rise to hybrid layers which combine assets in different altitudes. One such example is the integration of LEO satellite, high-altitude platforms (HAPs), unmanned aerial vehicles (UAVs), and ground stations (GSs) connectivity, where the terminals can seamlessly handover among multiple layers. On the other hand, FSO technology is a promising solution for the development of communication-based vehicles, such as autonomous cars, ships, high-speed trains, HAPs, UAVs, etc. As a result, the combination of satellite networks and FSO communications is expected to be a key enabling technology for future wireless networks.

However, optical communication from space is not without challenges. Depending on the weather and geographical location, various environmental factors such as clouds, atmospheric turbulence, snow, fog, haze, dust, etc., cause severe attenuation in the optical signal. Especially, cloud coverage is one of the critical concerns of satellite-based FSO links. Indeed, the availability of optical links can strongly deteriorate the system performance in the presence of cloud coverage [25]. Another main challenging issue of optical is turbulence-induced fading. The resulting atmospheric turbulence causes random fluctuations in both the amplitude and the phase of the received signal, i.e., channel fading [17]. As a result, the system performance is considerably degraded, especially in long-distance transmissions of about from tens to hundreds of kilometers from space [26]. Additionally, a significant problem comes from the pointing error caused by the random beam misalignment between transmitter (e.g., satellites, HAPs, etc.) and receiver (e.g., UAVs, GSs, etc.). In order to improve the satellite-based FSO system performance for all weather conditions, there has been a surge of interest to address the adverse issues mentioned above. Several innovative physical layer concepts such as site diversity, relay transmission, and hybrid FSO/RF



systems have been explored for the design of next-generation satellite-based FSO systems.

### 1.3. Original Contributions

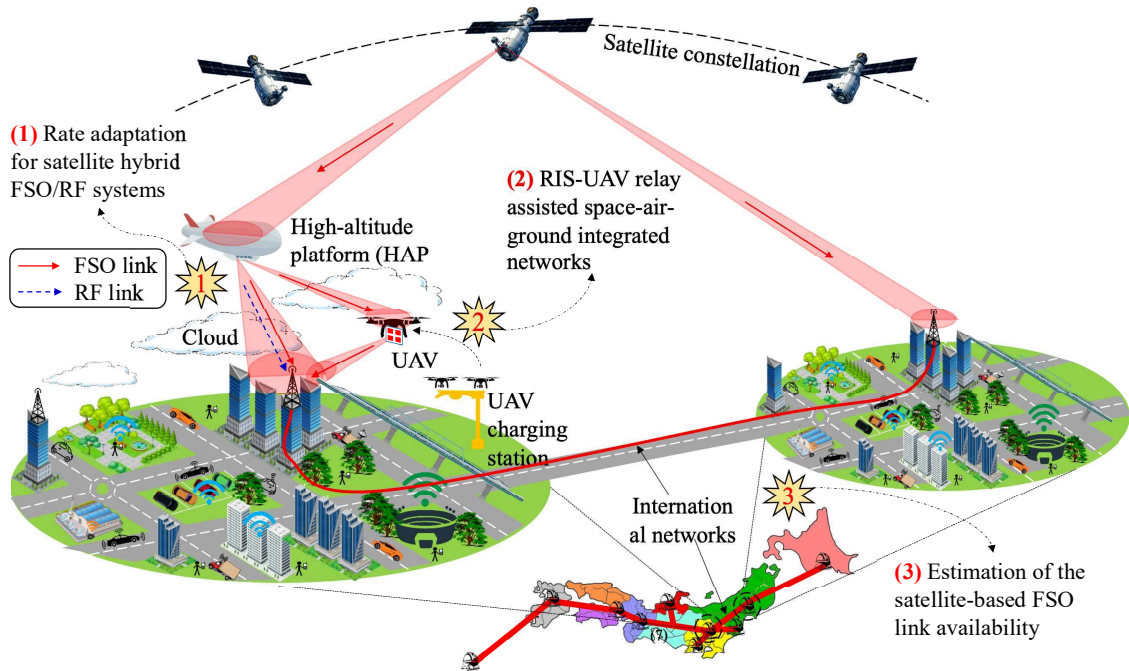


Figure 1.2: The contributions of the dissertation.

FSO-based satellite communications support many scenarios from small-scale networks such as rural areas, remote areas, urban area, etc., to large-scale networks such as a country. Therefore, to implement such system, we need to answer a big question *How to maintain reliable communications under the impact of adverse issues?*. Motivated from that perspective, the scope of the dissertation is **”Mitigation techniques for the impact of weather and atmosphere in satellite FSO communications”**. The primary contributions of the dissertation are shown in Fig. 1.2 and summarized as follow

1. *Firstly*, we design the rate adaptation for HAP-aided relaying optical satellite communication using a hybrid FSO/RF system. For the operation of the adaptive transmission rate, the data rate in each link (FSO or RF) gradually adjust following the channel state fluctuation under a target bit error rate

(BER) constraint. Besides, the optical downlink is analyzed by taking into account many challenging issues including beam spreading loss, cloud attenuation, turbulence-induced fading, and UAV hovering misalignment-induced pointing error. In addition, we also develop a comprehensive evaluation framework that allows obtaining the system performance metrics, including outage probability, average transmission rate, achievable spectrum efficiency, and average bit error rate.

2. *Secondly*, in the HAP-based SAGIN, the primary FSO connection from HAP to the ground station may be blocked by clouds containing high CLWC values. In this case, instead of using a lower-rate backup RF link, the RIS-UAV is deployed to a position with negligible cloud coverage to diversify the FSO-based HAP-to-ground link. Therefore, we propose a novel solution for the hybrid FSO/RF HAP-based SAGIN under the impact of weather and atmospheric conditions. Specifically, an additional unmanned aerial vehicle (UAV) is deployed to diversify the FSO link from the HAP-to-ground station to avoid cloud blockage while maintaining a high-speed connection of the FSO link. A mirror array constructed by re-configurable intelligent surface (RIS), an emerging technology, is mounted on the UAV to reflect the signals from the HAP. The channel model of RIS-UAV takes into account both atmospheric turbulence and hovering-induced pointing errors. Furthermore, we present a novel link switching design with a multi-rate adaptation scheme for the proposed network under different weather and turbulence conditions. Numerical results quantitatively confirm the effectiveness of our proposal. Additionally, we provide insightful discussions that can be helpful for the practical system design of RIS-UAV-assisted HAP-based SAGIN using hybrid FSO/RF links.
3. *Finally*, in the situation, clouds develop to cover a huge area, and the application on the ground needs to meet the requirement of a high-speed connection. Hence, the solution for a large-scale network, e.g., a country, needs to investigate. Site diversity is one of the possible solutions to satisfy the requirement. The site

diversity technique links two or more ground stations receiving the same signal: this way, if the signal is heavily attenuated in one area, another ground station can compensate. It is important to investigate the weather-related issues in different regions in deciding the optical ground station that can communicate reliably with the satellite. Therefore, we provide analysis to estimate the satellite-based FSO link availability considering the two main effects, cloud blockage and turbulence-induced fading. Regarding the cloud attenuation distribution, we obtain the 5-year reanalysis meteorological ERA-Interm database from the European Center for Medium-Range Weather Forecast (ECMWF) [27]. The optical link availability is estimated for several regions in Japan; then, the site diversity techniques are applied to improve the system performance.

## 1.4. Dissertation Organization

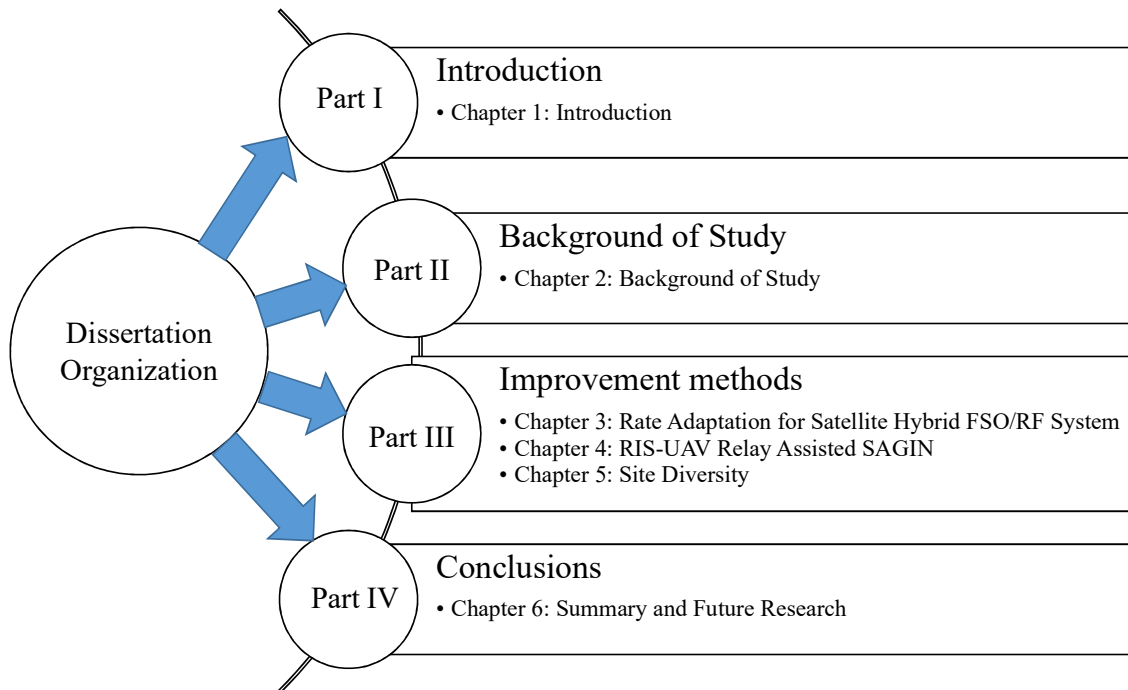


Figure 1.3: Dissertation structure.

The structure of the dissertation is organized as shown in Fig. 1.3. Chapter 1 introduces an overview of optical satellite communications and the original contributions.

In addition, the motivations and original contributions for the issues considered in the dissertation, including site diversity technique, rate adaptation for satellite hybrid FSO/RF system, RIS-UAV relay-assisted SAGIN, are also presented.

Chapter 2 provides the relevant background of the study. Firstly, the history and the current development of FSO-based satellite communication system in Section 2.1. Then, we describe more detail of such system in Section 2.2. Next, we introduce the adverse issues during the satellite-based FSO transmission, including atmospheric attenuation, turbulence-induced fading, cloud attenuation, and pointing error in Section 2.3. In Section 2.4, we introduce several mitigation techniques, including site diversity, relay transmission, and hybrid FSO/RF system. Section 2.5 summarizes the Chapter.

In Chapter 3, we present the proposed rate adaptation design of HAP-assisted relaying optical satellite communication for mobile networks supported by UAV. The relay-assisted satellite hybrid FSO/RF communication description is shown in Section 3.2. In Section 3.3, the FSO and RF channel models are investigated. Next, Section 3.4 presents rate adaptation and analyzes the system performance concerning the average transmission rate, achievable spectrum efficiency, outage probability, and average bit error rate. The discussion on the numerical results is expressed in Section 3.5. Section 3.6 summarizes several critical points of this Chapter.

Chapter 4 propose to deploy an additional UAV equipped with a RIS array in the HAP-based SAGIN to enhance the system performance under the impact of weather conditions. The proposed system, link switching scheme, and rate adaptation design are described in Section 4.2. Section 4.3 presents the channel models for transmission links. Different performance metrics, including outage probability, average transmission rate, and spectral efficiency are analytically derived in Section 4.4. Simulation results are given in Section 4.5. The summary of this Chapter is shown in Section 4.6.

Chapter 5 focuses on the site diversity technique. In particular, the network descriptions is presented in Section 5.2. The performance analysis is presented in Section

5.3. Also, numerical results are given in Section 5.4. We conclude this Chapter in Section 5.5.

Finally, we conclude the dissertation in Chapter 6 with a summary and outlooks on the future research directions.

# Chapter 2

## Background of Study

This Chapter provides a comprehensive view of the history of the development of optical satellite communications. It covers all sub-assemblies of a laser communication transceiver from the flight subsystem to the ground subsystem. This chapter describes the vertical and slant path propagation links and several main challenging issues of FSO-based satellite communications. Then, performance improvement solutions are addressed to mitigate the impact of weather and atmosphere condition, including diversity technique, relay transmission, rate adaptation, and hybrid FSO/RF.

### 2.1. Satellite Communications

Today, optical fiber technology is managing much of the ground access network and backbone network at tens of tera-bit-per-second (Tbps) collective capacity [28]. However, due to expensive costs and/or geological obstacles, optical fiber networks have been inappropriate in inaccessible areas (disaster areas, marine areas, desert areas, etc.) and isolated areas (rural areas, remote areas, etc.). With the mission of global coverage, a communication network from space, where wired communication is not applicable, is necessary [29]. A communication satellite is an artificial satellite responsible for transmitting the signal through a transponder as it creates a channel between the transmitter and the receiver situated at different locations on Earth.

Telecommunications via satellites, HAP, and UAV may bridge this gap and deliver backhaul service coverage to sparsely populated areas. In recent years, optical satellite communication has been rapidly developed as it offers lower system size, mass, and power consumption. Link reliability and availability aside, current communications capacity via airborne and spaceborne platforms now constitutes only a small fraction of those provided by optical fiber networks. However, such platforms equipped with a multitude of Earth-observing sensors and broadband communication systems are experiencing exponential growth in telecom data volumes

### 2.1.1. History of Satellite Communications

On 4 October 1957, the world's first artificial satellite, namely Sputnik, was launched to open the chapter for satellite communications. Since then, more than 12000 artificial satellites have been launched until May 2022, as reported by the United Nations Office of Outer Space Affairs (UNOOSA) [30]. Among the total launched objects, approximately 4800 satellites are currently operational in different orbits around the Earth [31]. Over the past 60 years, satellite technology has demonstrated its usefulness successfully by providing various services such as communications, remote sensing/earth observation, navigation, weather monitoring, and space exploration for defense, civil, and commercial purposes [32]. Several important milestones can be listed in the history of satellite communication such as telephone, television signal from space, military missions, and Internet access from space.

- *Telephone, Television signal*: The first communication satellite is performed in 1962 by Telstar 1 built by Bell Labs, owned by AT&T, and launched by NASA. The satellite relayed the signal across the Northern Hemisphere.
- *Military missions*: Civilians knew the first global positioning system in 1966, thanks to the Defense Advanced Research Project Agency USA. GPS was originally reserved for use by the military.
- *Internet access from space*: A significant enabler of satellite-delivered Internet

has been the opening up of the Ka-band for satellites. In December 1993, Hughes Aircraft Co. filed with the Federal Communications Commission (FCC) for a license to launch the first Ka-band satellite, Spaceway. Until now, a rising number of companies, i.e., SpaceX, OneWeb, Amazon, etc., announced working on internet access using satellite constellations in low Earth orbit. Currently, SpaceX has over 2,300 functioning Starlink satellites in orbit, OneWeb has 648 satellites in orbit, and Kuiper-Amazon has 3236 satellites in orbit. As a result, FSO-based satellite communication is expected to be one of the critical enabling technologies in the future six-generation (6G) wireless networks [33].

### 2.1.2. Satellite Orbit Classification

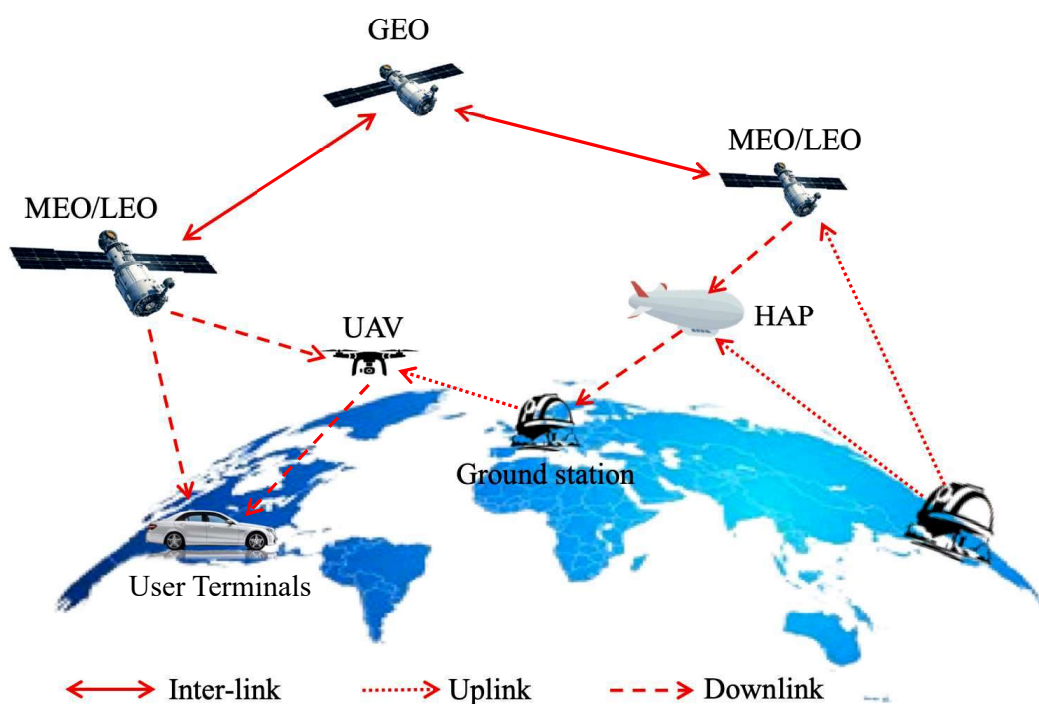


Figure 2.1: Optical satellite communications.

Satellite communications are the results of research efforts in both areas of communications and space technologies whose objective is to achieve ever-increasing ranges and capacities with the lowest possible costs. A satellite communication system is basically composed of a space segment, a control segment, and a ground segment [34]. The *space segment* consists of one or several active satellites organized into a con-



stellation. The *control segment* is also known as tracking, telemetry, and command (TTC) stations. This segment manages the traffic and resources onboard the satellite for communication networks. The *ground segment* contains all the ground stations, and user terminals with fixed or mobile platforms (e.g., high-speed trains, ships, autonomous cars, etc.). Depending on the application and use cases, these stations have different sizes, from a few centimeters to tens of meters. The fundamental aspect of satellite links is illustrated in Fig. 2.1, which includes the inter-link (satellite-to-satellite), uplink (ground-to-satellite), and downlink (satellite-to-ground). There are three basic orbit configurations, which are the trajectory followed by the satellite, including:

- Geostationary orbit (GEO): It situates at an altitude of 35768 km from Earth's surface. GEO satellites match the rotation of the Earth as they travel; so they remain above the same point on the ground. Three GEO satellites can provide global coverage, i.e., 99% of the world population and economic activities except for the polar region [35]. GEO satellites are used for weather data, broadcast TV, etc.
- Medium-Earth orbit (MEO): It has an altitude range from 2000 km to 35768 km above the Earth. Due to its lower altitude than GEO, the MEO constellation typically needs dozens of satellites to offer continuous coverage and real-time communications. MEO satellites are usually used for global position systems (GPS) and other navigation applications.
- Low-Earth orbit (LEO): It has an operational altitude range from 160 km to 2000 km above the Earth's surface. LEO satellites move relatively fast as closer to the Earth; thus, they require a tracking system to maintain communication between satellite and ground stations. Compared to GEO and MEO, LEO is densely populated with thousands of satellites in operation today due to cost-efficiency, lower latency, and less power consumption.

### 2.1.3. Different Satellite Communication Systems

Since the early days of laser development, multiple space agencies in the United States, Europe, and Japan attended to satellite communication race to develop both terrestrial and space communication systems. Space-air-ground integrated network (SAGIN), as the integration of satellite systems, aerial networks, and terrestrial communications, has been becoming an emerging architecture and attracted intensive research interest during the past years. As shown in Fig. 2.2, the SAGIN comprises three main segments: space, air, and ground. These three segments can work independently or inter-operationally, by integrating heterogeneous networks among the three segments, it is straightforward to build a hierarchical broadband wireless network.

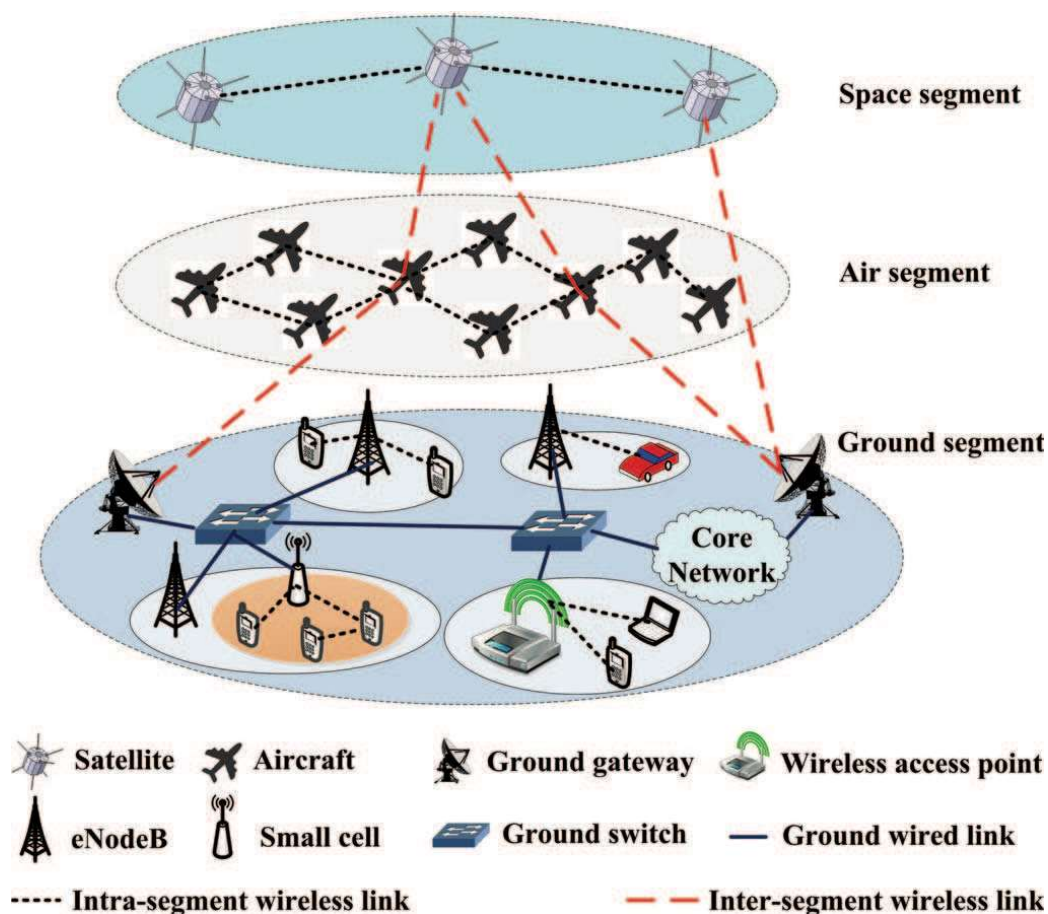


Figure 2.2: An example of architecture for space-air-ground integrated network [1].

## 2.1.3.1. Inter-Satellite Communications

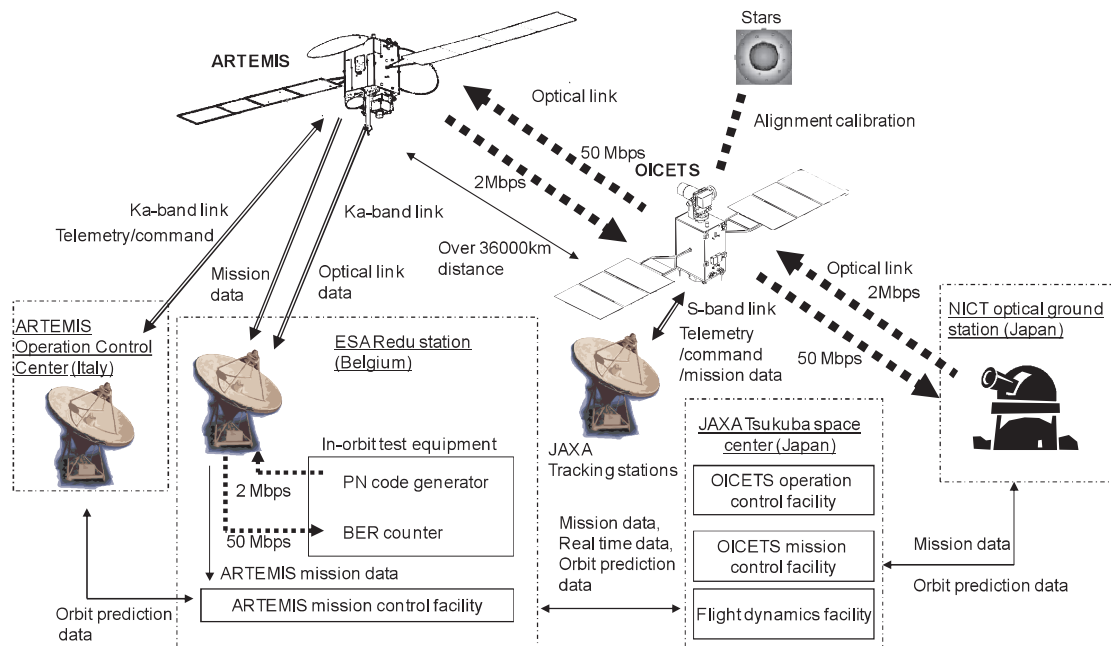


Figure 2.3: Experiment system configuration of optical inter-orbit communications [2].

The space segment, i.e., inter-satellite communications, is composed of satellites and constellations as well as their corresponding terrestrial infrastructures, e.g., ground stations and network operation control centers. These satellites and constellations are in different orbits and with different characteristics. Depending on the altitude, satellites can be classified into three categories: GEO, MEO, and LEO. On the other hand, satellite networks can be categorized into narrowband and broadband according to their channel bandwidth. Narrowband satellite networks refer to the MEO/LEO satellite systems, which mainly provide global users with voice and low-rate data services. A broadband satellite network can offer a high-speed data transmission rate of up to 10 Gbps [36] and is expected to have a capacity of 1000 Gbps by the years 2020 [37] by using a wide band of frequencies that can carry a lot of data. The experiments of optical inter-orbit communications between OICETS and ARTEMIS were conducted collaboratively by Japan and Europe in the period from December 2005 to August 2006, and experimental results were obtained for various orbits. Fig. 2.3 shows the entire experiment link system configuration of optical inter-orbit commu-

nications, including the satellite operation and experimental data flows. Given  $\text{BER} < 10^{-6}$ , the optical forward link (from ARTEMIS to OICETS) achieved the data rate of 2.048 Mbps with the wavelength of 819 nm while the data rate of the return link (from OICETS to ARTEMIS is 49.3724 Mbps with the wavelength of 847 nm.

### 2.1.3.2. Satellite-to-High-Altitude Platform (HAP)

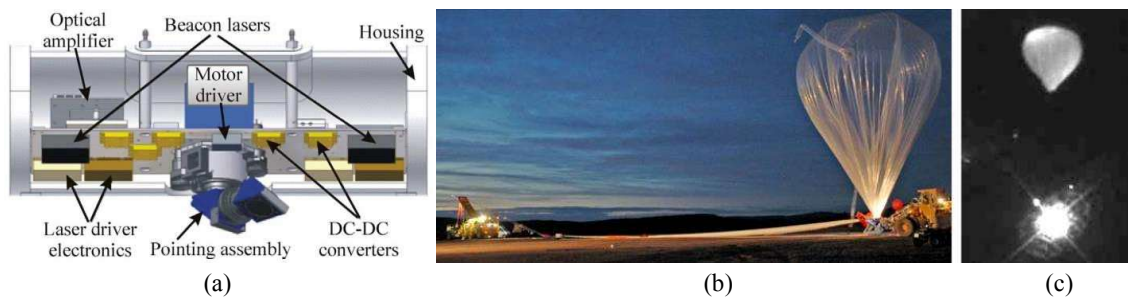


Figure 2.4: (a) Stratospheric flight terminal with the periscope-type coarse pointer, (b) stratospheric balloon during launch preparations for CAPANINA, and (c) near-infrared photograph of flight terminal below stratospheric balloon [3].

Current research also investigates optical communication from or to the high-altitude platform (HAP) [3, 38]. HAPs are aircraft or airships situated well above the clouds at typical heights of 17 to 25 km, where the atmospheric impact on a laser beam is less severe than directly above ground [26]. HAPs are quasi-stationary vehicles that operate in the stratosphere well above civil air routes, jet streams, and clouds, but substantially below orbiting satellites. HAPs are expected to support payloads up to 2000 kg. HAP-based systems offer a number of benefits, like a reduced shadowing from terrain, a wide service coverage area of 200–500 km diameter, rapid deployment, easier maintenance, lower cost than with satellites, and environmental advantages by reducing the need for terrestrial infrastructure or rocket launches, no requirement for space-qualified components (but still some flight qualification). The study in [39] described the European Aeronautic Defence and Space Company (EADS) Astrium-coordinated development of an aircraft terminal in the project Liaison Optique Laser Aeroportee (LOLA) for communication between an aircraft and the geostationary orbit (GEO) satellite ARTEMIS. The LOLA terminal was designed to cope with the

increased difficulty of a moving aircraft. Data were planned to be transmitted at 848 nm and with 50 Mbps to the satellite. Fig. 2.4(a) shows a sketch of the balloon terminal with the 977 nm beacon [40]. Fig. 2.4(b) depicts the preparations for the launch of the stratospheric balloon, and Fig. 2.4(c) shows the payload below the balloon, as seen from the ground station's tracking camera.

### 2.1.3.3. Satellite-to-Unmanned Aerial Vehicle (UAV)

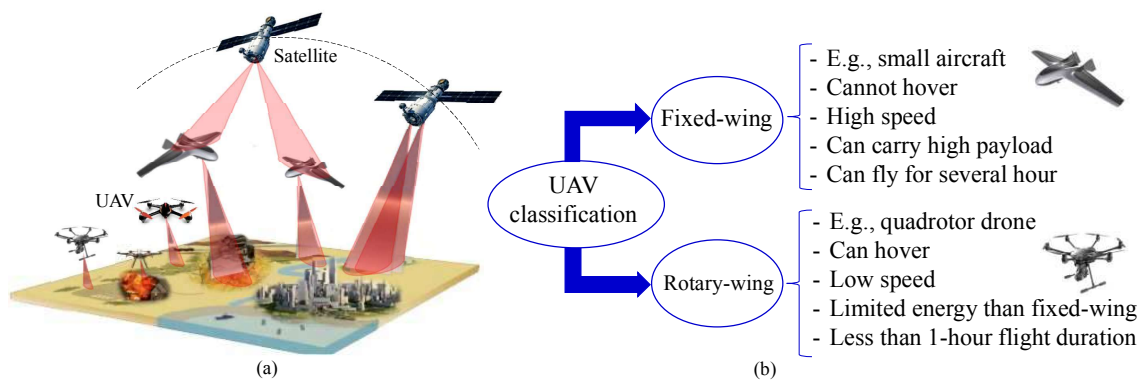


Figure 2.5: Satellite-to-UAV communications: (a) Use cases and (b) UAV classification.

The use of flying platforms such as unmanned aerial vehicles (UAVs), popularly known as drones, is rapidly growing [41, 42]. Thanks to the popularity of LEO satellite, the satellite-to-UAV communications have recently emerged for many applications ranging from fixed Internet access to autonomous such as military missions, delivery services, and even temporary mobile base stations (BS) [18, 43] as shown in Fig. 2.5(a). Depending on the type, UAVs can be categorized into fixed-wing and rotary-wing. Figure 2.5(b) provides an overview of the different types of UAVs, functions, and capabilities. It is worthy to note that the flight time of a UAV depends on several factors such as energy source (e.g., battery, fuel, etc.), type, weight, speed, and trajectory of the UAV. For satellite-to-UAV communication systems, it becomes more crucial to understand the statistical behaviors of the satellite downlink channels when the impact of the atmosphere and weather is severe. Especially in a particular case of a UAV in mobility, it is necessary to take into account the impact of channel misalignment due to the UAV hovering.

### 2.1.3.4. Satellite-to-Ground Station (GS)

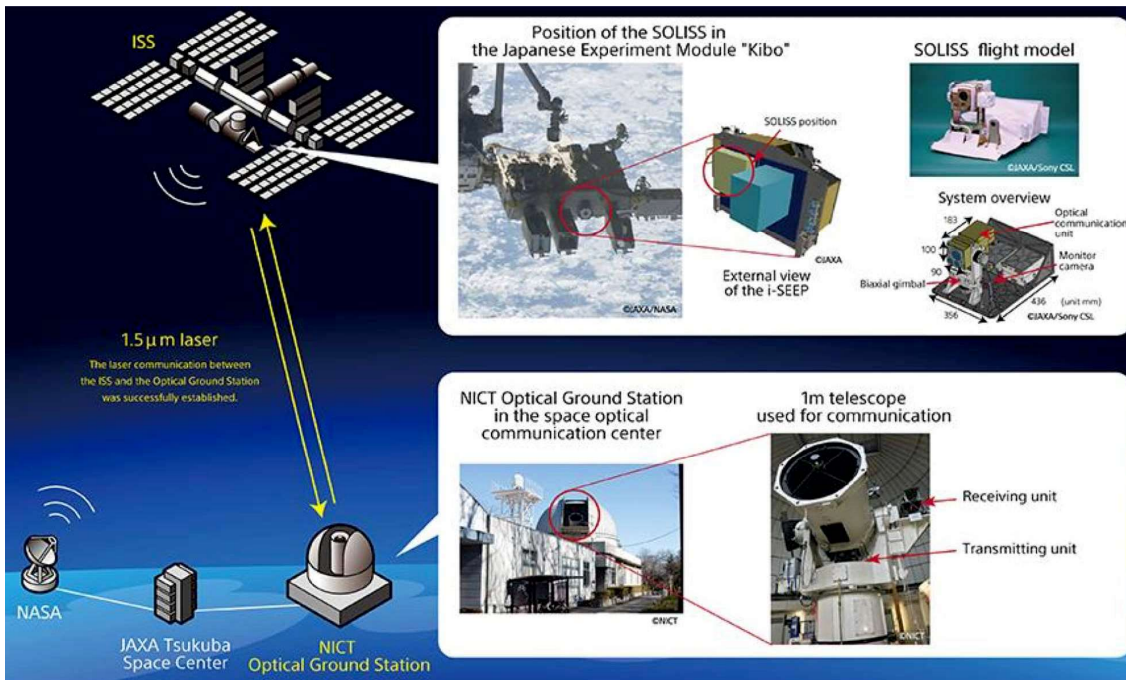


Figure 2.6: Bidirectional Laser Communication Between Space and Ground Station [4].

Fig. 2.6 shows the first success in 2020 in establishing a bidirectional laser communication link between the optical ground station (GS) in Japan and a satellite in International Space Station (ISS) in transmitting high-definition (HD) image data via Ethernet [4]. In satellite-to-ground communication, a GS consists of several components that allow transmission and reception to and from the satellite, amplification of the signals, transformation, and connection to the terrestrial network. The main part of an optical GS is the telescope that sends and receives the satellite signals. The requirement diameter of an optical GS for communications with an LEO satellite is 0.6 to  $>1$  m [5]. Almost optical GSs are located in Japan, Europe, and the United States [44, 45]. The large telescope diameter has a beneficial impact on the link budget for the downlink, as the receiver gain increases with the receiver diameter. For the uplink, the transmitter size is limited by turbulence, especially pointing accuracy. The beam wander cannot be minimized when transmitting and receiving through different apertures. Hence, the divergence needs to cope with all the beam wander movements to ensure that the uplink reaches the satellite most of the time.

## 2.2. FSO in Satellite Communications

In recent years, wireless communications have witnessed an unprecedented explosion. From cellular networks to satellite links, unguided telecommunications have enabled countless new services, firmly established as a basic part of the current information society. In particular, free-space optical (FSO) communication, despite its recent emergence, provides a number of advantages that allow the materialization of completely-new applications such as quantum communications, as well as the promise to revolutionize traditional applications like satellite communications. FSO technology can be applied in a wide variety of scenarios, from crosslinks to up-and-downlinks between satellites, aircraft, ships, and ground-standing or mobile terminals.

### 2.2.1. History and Current Development

The first laser communication systems were shown in space in the 1990s, it is recently that the technology and economics of satellite-based FSO systems have combined with the need for more bandwidth to push them into operation. Revolutions assisted by multiple space agencies pave the way for commercial use of FSO technology [35], which is planned to develop future communication network architectures. Table 2.1 summarizes historic milestones in optical satellite communications technology demonstrations and most recently operational deployments. With innovations in laser communication optical assemblies along with advancements in optical fiber technology that is directly applicable to laser communications, cost flight systems are expected in the near future. The cost of the flight transceiver is driven primarily by those required for flight qualification. Volume manufacturing of light-qualified laser communication systems remains a challenge that will likely be facilitated through automated integration and testing. Lower cost ground stations with a diameter of 0.6 to 1 meter are also of prime interest. Toward this goal, commercial entities are aiming at providing ground communication station networks commercially throughout the globe.

Table 2.1: Optical Satellite Communication Links Successfully Performed [5].

Year	Project	Link	Max. Data Rate (Gbps)	Organization and Notes
1981	AFTS	Airplane		McDonnell Douglas
1991	TALC	Plane-submarine		GTE
1992	GOPEX	Ground to deep space	N/A	Laser beam pointing from ground to a satellite in deep space
1995	LCE	GEO-ground	0.001	National Institute of Information and Comm. Tech. (NICT, Japan), Jet Propulsion Laboratory JPL/NASA, Duplex links
1996	RME	Space relay		Ball Aerospace
2001	GeoLITE	GEO-Ground	>1	Lincoln Lab. (USA). Duplex
2001	SILEX	LEO-GEO	0.05	European Space Agency. Duplex
2002	ALEX	GEO-Air	>1	Lincoln Lab. Duplex links to GeoLITE
2005	LUCE	LEO-LEO, LEO-Ground	0.05	JAXA (Japan), OICETS spacecraft
2006	LOLA	Air-GEO	0.05	France; Duplex links to SILEX
2008	LCTSX	LEO-LEO, LEO-Ground	5.5	DLR/TESAT-Spacecom (Germany). Coherent detection
2013	Alphasat	LEO-GEO	1.8	European Space Agency (ESA)
2013	LLCD	Moon-Earth	0.622	NASA/Lincoln Lab./JPL
2014	Sentinel-A	LEO-GEO	1.8	Operational use from satellites
2014	OPALS	LEO-Earth	0.175	NASA/JPL
2014	SOTA	LEO-Earth	0.01	NICT
2016	EDRS-A	LEO-GEO	1.8	ESA
2016	OSIRISV2	LEO-Earth	1	DLR
2017	Sentinel-2	LEO-GEO	1.8	ESA
2020 (plan)	LCRD	GEO-Earth, Earth-GEO	1.244	NASA Goddard Space Flight Center



### 2.2.2. Laser Transmitter

The transmitter is often the key contributor to the transceiver's overall power budget and transmitter efficiency can significantly affect the design of an optical terminal. The optical output power level that the transmitter has to provide is the product of the receiver input power required for the specific data rate at a certain signal quality, the channel loss, and the gains and losses of the telescopes and the optical systems of the two terminals. In a free-space system, the transmitter has to provide the transmit power for the entire signal path so that much higher output power levels than in terrestrial systems may be necessary. A brief overview of transmitters for free-space data transmission systems is provided in Table 2.2.

Table 2.2: Overview of Transmitters for Free-Space Data Transmission Systems [5].

System type	Coherent						Non-coherent		
Ref.	[46]	[46]	[47]	[48]	[47, 48]		[49]	[50]	
Name	Terra-SarN-Fire	EDRS	EDRS	Facebook	Facebook	LEO-net			LCRD
Application	LEO-LEO	LEO-GEO	ground-GEO	HAP-HAP	HAP-ground	LEO-LEO	ground-LEO	GEO-ground	GEO-LEO
Link range (km)	6000	45000	39000	250	50	6000	39000	39000	N/A
Modulation	BPSK	BPSK	BPSK	16 QAM	16 QAM	N/A	DPSK	DPSK	DPSK
Wavelength (nm)	1064	1064	1064	1550	1550	1064	1550	1550	1550
Data rate (Gbps)	5.6	2.8	2.8	100	1000	10+	100	40	1.24
Output Power (W)	1	5	50	1	0.1	4	40×4×10	16×0.2	0.5
Operation remark	Tested 1st gen.	Active 2nd gen.	Active	Tested	Tested	Assumed	Study	Study	Planned

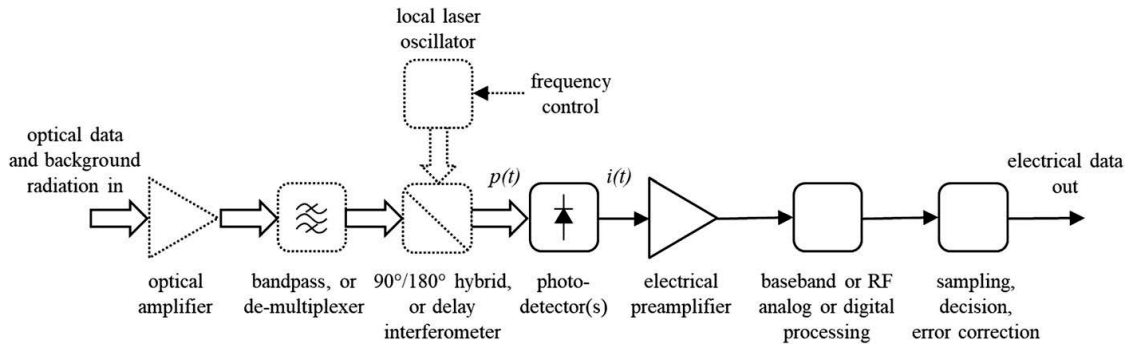


Figure 2.7: Basic diagram of a generic FSO system [5].

### 2.2.3. Photodetectors and Receiver Architectures

Figure 2.7 shows the generic block diagram of a receiver for digitally modulated data. In its simplest form, the receiver comes without the dashed subunits. The detection process is in general hampered by background radiation inadvertently received by the optical antenna. Hence, an optical bandpass filter centered at the carrier wavelength  $\lambda$  is usually implemented to reduce the adverse effects of background radiation on signal detection. The filter passes the optical data signal that is converted into electrical current  $i(t)$  using a photodetector. Electrical amplification and baseband processing is followed by sampling, decision, and forward error correction (FEC) decoding. This type of receiver, in which the information-bearing electrical signal current is linearly proportional to the optical signal power  $p(t)$  at the detector, is called a direct detection receiver. One may achieve a considerable improvement in receiver sensitivity by including a low-noise optical pre-amplifier. Alternatively, one may use a coherent receiver in which the single-frequency radiation of a local oscillator (LO) laser is superimposed and mixed with the optical input signal upon square-law detection. The photodetector then generates—among other terms—an electrical signal directly proportional to the optical field<sup>1</sup> of the optical input signal. The electrical signal is centered at the frequency difference between the optical input signal and the local laser light. Coherent receivers offer not only improved receiver sensitivity compared to direct detection without optical pre-amplification but also the possibility to readily detect signals that are modulated in phase or frequency.

### 2.2.4. Acquisition, Tracking, and Pointing Mechanisms

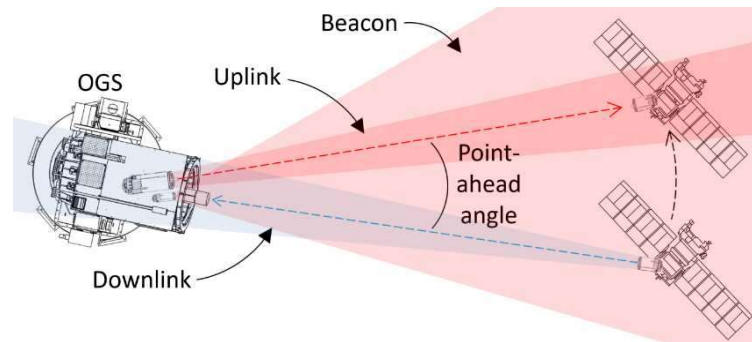


Figure 2.8: Block diagram of an ATP mechanism designed for FSO communications [6].

In the case of long transmission distance, the optical beam reaching the Earth has a size of around one terrestrial diameter. This great directivity demands a high pointing accuracy. After the acquisition, when both terminals establish the line of sight to each other, the procedure to keep pointing and tracking are several orders of magnitude more complex than with RF. In RF, the pointing accuracy is in the order of milliradians in the Ka-band, whereas a deep-space optical link would typically require sub-micro radian accuracy. To keep a stable line of sight, it is necessary to use some reference to the other end. This can be achieved by a laser transmitted as a beacon from the ground terminal if the satellite is close to the earth, or celestial references if it is in deep space. Fig. 2.8 shows the main elements in a typical near-to-Earth link. To initiate the acquisition, the beacon is transmitted with divergence as wide as the uncertainty zone where the satellite is predicted to be according to its orbital elements. Afterward, the space system searches for the beacon, looking at the predicted direction of the optical GS and transmitting its downlink towards the beacon at a different wavelength or polarization, once it has been found. Lastly, the OGS can transmit a beam much narrower than the beacon by using the downlink reference in a close loop. Alternatively, scanning algorithms can be implemented, where both terminals scan angularly the counter partner.

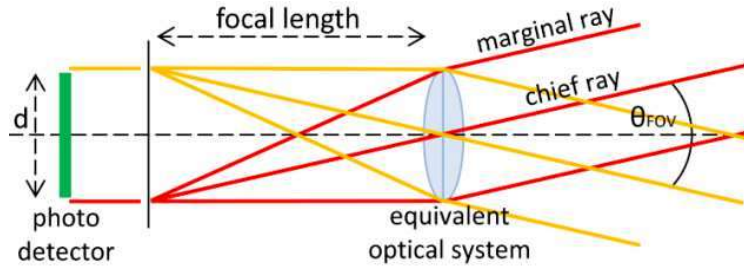


Figure 2.9: Field of view of a generic optical-communication system defined by its focal length  $f$  and photodetector of size  $d$  [6].

### 2.2.5. Field of View

The field of view (FoV) describes the angular extent that the object plane shows in the image plane of an optical system. FoV depends not only on the characteristics of the optical system but also on the photodetector that captures the light of that system. Fig. 2.9 shows the FoV  $\theta_{FoV}$  of a generic optical system characterized by its equivalent focal length  $f$  and the size  $d$  of a photodetector in the image plane. Fig. 2.9 represents the convergence of two collimated beams on the equivalent focal plane of the receiving system, describing the widest angle for a given photodetector size  $d$  and a focal length  $f$ . The chief ray (going through the center of the optical system) and the marginal ray (going through the edges of the aperture) describe completely the collimated beams going through an optical system. The FoV  $\theta_{FoV}$  assuming a circular detector can be deduced by

$$\theta_{FoV} = 2\text{atan}\left(\frac{d}{2f}\right), \quad (2.1)$$

This equation shows that the FoV is proportional to the detector size and inversely proportional to the focal length, which is determined by the chief ray. If the optical satellite system has to operate during the day under strong sky radiance, small detector size and long focal length should be considered (which requires a better pointing accuracy) in order to minimize the background noise.

### 2.2.6. Modulation

The simplest way to modulate an optical signal consists in turning the transmitter's laser On-Off Keying (OOK). This is an intensity binary-level modulation that allows using direct detection, which is the most common technique due to its simplicity: Intensity Modulation/Direct Detection (IM/DD). These receivers convert the optical signal directly to an electrical current by using detectors following the square law, meaning that the electric output is proportional to the square of the amplitude of the electric field recovering directly the original intensity-modulated signal. Pulse Position Modulation (PPM) is a variation of OOK, with less spectral efficiency but much more energy efficiency. It finds a good application when the spacecraft energy resources are scarce and the losses are high, i.e. low photon flux links, such as in deep space. Together with single-photon receivers, PPM is the optimum solution for photon-starved channels with data rates under  $\approx$ Gbps. This modulation allows encoding more than one bit per pulse by dividing the duration of each sequence of  $n$  bits into  $M = 2n$  slots, corresponding to  $m$  symbols. When each pulse is sent, it is placed in one of the slots, defining the symbol to transmit.

Coherent demodulation consists in combining the received signal with a local oscillator in the optical domain so that the surface of the photodiode receives a mixture of both signals. For a coherent detector to work properly, it is essential that the local laser matches in frequency and phase to the received signal. When that condition is met, this scheme improves background-noise rejection because the received signal is amplified after mixing it with the local oscillator, resulting in a higher SNR. Currently, coherent detection based on analog optical phased-lock-loop is applied operationally in inter-satellite links. The high sensitivity of this reception technology allows transmission over large distances (LEO to GEO). For the satellite to ground links, adaptive optics at the receiver are required for either achieving a high-heterodyne efficiency when mixing the received signal with the local oscillator or for coupling into a single-mode fiber. Both approaches have similar requirements and depend on the relation between the receiver aperture diameter and the atmospheric coherent length, i.e. the

Fried parameter [51].

### 2.2.7. Link Budget

Table 2.3: Link-budget calculation for LEO-to-ground mission [52].

Transmitted power $P_T$ (dBm)	15.40
Transmitting gain $G_T$ (dB)	85.08
Transmitter loss $L_T$ (dB)	1.97
Pointing loss $L_P$ (dB)	5.70
Free-space loss $L_S$ (dB)	259.06
Atmospheric loss $L_A$ (dB)	2.66
Receiving gain $G_R$ (dB)	126.14
Receiver loss $L_R$ (dB)	7.40
Received power $P_R$ (dBm)	-50.18

The link budget is the key method to determine the overall performance of an optical satellite system under a set of operating conditions. The link budget is given by

$$P_R = P_T G_T L_T L_P L_S L_A L_R G_R, \quad (2.2)$$

where the received power  $P_R$  to the transmitted power  $P_T$ , the transmission and reception gain  $G_T$  and  $G_R$ , the losses of the transmitter  $L_T$  and the receiver  $L_R$ , the atmospheric losses  $L_A$ , the pointing losses  $L_P$  and the free-space losses  $L_S$ .

Table 2.3 shows an example of a basic link-budget calculation for the LEO-to-ground SOTA mission carried out by NICT (Japan) [52]. The conditions of this link budget are as follows: the telescope's elevation is  $30^\circ$  for a link distance of 1,107 km between the  $\approx 600$  km SOTA orbit and the NICT's OGS in Koganei (Tokyo, Japan) during the pass on December 9th, 2015; the operating wavelength is 1549 nm; the receiver's aperture is 1 m; the optical signal is coupled into multi-mode optical fiber; and the transmitter, receiver and pointing losses are based on experimental measurements. As in the report, the received power measured in an experiment with the same conditions as in the link budget the calculation was  $-51.30$  dBm. Since there are many factors affecting any link-budget calculation, a common practice is taking a few dBs as link margin.

### 2.2.8. Operating Wavelength

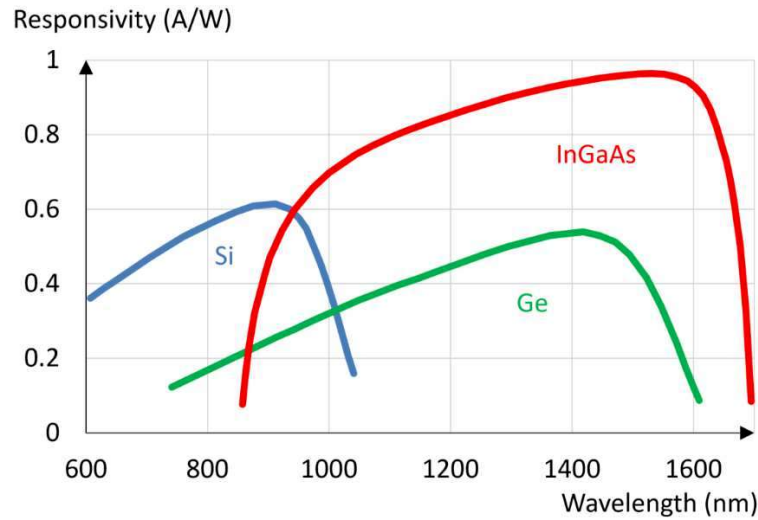


Figure 2.10: Typical responsivity versus wavelength for silicon (Si), InGaAs, and germanium (Ge) [6].

Operating wavelength is easy to understand and how important choice is in an FSO-based satellite link. The shorter the wavelength, the higher the antenna gain and the lower the free-space losses are. Hence, from the geometrical point of view, shorter wavelengths are preferable (the same consideration is valid for increasing the transmitting and/or receiving aperture in terms of improving the delivery of power due to geometrical reasons: In the first case, the beam divergence gets reduced, and in the second case, more signal can be gathered). However, the strength of intensity fluctuations due to atmospheric turbulence increases with  $\lambda^{-7/6}$ , the atmospheric attenuation increases with  $\lambda^{-2}$ , and the scattering attenuation and sky radiance increase with  $\lambda^{-4}$ . Therefore, if the signal must go through the atmosphere, shorter wavelengths provide a larger scintillation with a stronger impact on the sky radiance.

Currently, there are three important regions where the FSO-based satellite system operates. The most popular regions are around  $1.064\mu\text{m}$  and especially  $1.55\mu\text{m}$  if the laser beams propagate through the atmosphere because of their better behavior. Furthermore, there is plenty of technology available at  $1.55\mu\text{m}$  from optical-fiber communications, the attenuation is lower and the responsivity of InGaAs photodetectors shows a good behavior as shown in Fig. 2.10. From the eye-safety point-of-view,

$1.55\mu\text{m}$  is preferred because the eye fluids absorb these wavelengths before being focused on the retina.  $1.064\mu\text{m}$  has been developed mainly for inter-satellite links, where eye safety is not an issue and there is no atmosphere in the channel. This shorter wavelength takes advantage of lower beam divergence and bigger antenna gain while having available the NdYAG technology, especially suitable for coherent communication. When the receiver's noise is an issue, e.g. in quantum communications, wavelengths in the band of 800 nm–900 nm can be preferred, taking advantage of the good responsivity of silicon photodetectors, which are less noisy than InGaAs and germanium [6].

## 2.3. FSO Channel in Satellite Communications

The optical beam launched from the satellite is affected by various unpredictable environmental factors before arriving at the receiver, which can be the ground station, vehicle, etc. These factors are dependent on the weather and geographical location. In this dissertation, we describe several major limitations including atmospheric attenuation, atmospheric turbulence, geometric loss, misalignment loss, and cloud attenuation.

### 2.3.1. Vertical Versus Horizontal FSO Channels

Operating over the free-space medium, the performance of terrestrial FSO systems is significantly affected by atmospheric conditions and pointing error as shown in Fig. 2.11. On the one hand, it is the power loss due to absorption and scattering by particles (e.g. water droplets, dust, and snow) in the air. This essentially limits the coverage of the systems. On the other hand, it is the random fluctuation of transmitted optical power (intensity) caused by atmospheric turbulence and pointing error. Compared to the terrestrial scenario, FSO-based satellite links experience lower noise and impairment [53]. However, the ultra long range of the links is a critical impairment for optical satellite links. This is because the longer the transmission distance, the higher the transmission power, size, mass, and cost. In addition, alignment of



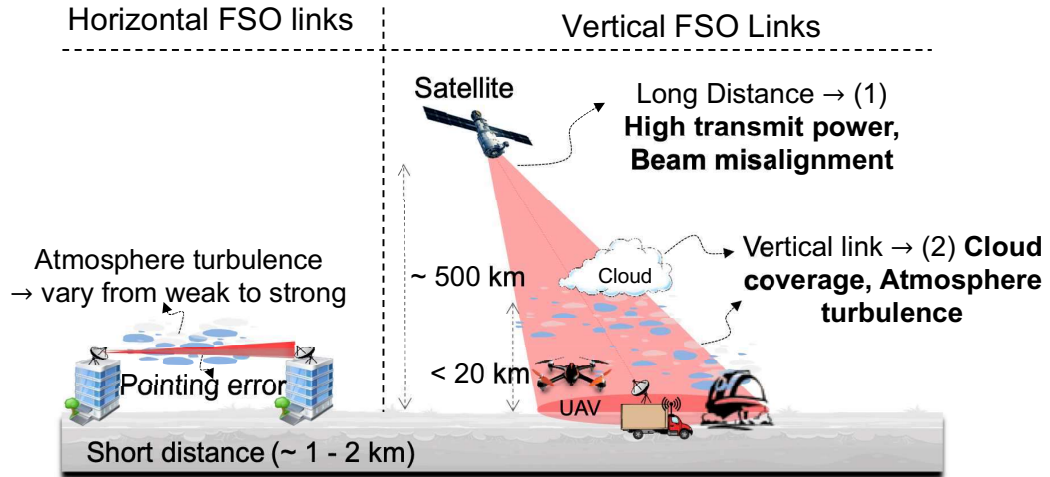


Figure 2.11: A different channel model comparison between vertical and horizontal FSO links.

the transmit and receive antennas must be maintained due to the vibration and the continuous movement of satellites/UAVs/High-speed trains/autonomous cars. Moreover, the weather effect, e.g. clouds which are usually ignored in consideration for terrestrial networks, is a key challenging issue for FSO-based satellite communication networks. Following sections, we discuss in more detail FSO transmission limitations for vertical networks.

### 2.3.2. Atmospheric Attenuation

Optical signals from the satellite to the ground propagate through the atmosphere composed of gas molecules and aerosol particles. These particles absorb the laser beam energy, causing an optical power loss, and light scattering, which changes the propagation of incident light from its initial direction. To describe a power transmission loss mechanism, the Beer-Lambert law is used as a function of the propagation distance [54]

$$P_r = P_t \exp(-\delta(\lambda)d), \quad (2.3)$$

where  $P_t$  and  $P_r$  are the transmitted optical power and received optical power, respectively.  $d$  is the FSO transmission distance,  $\lambda$  is the optical wavelength.  $\delta(\lambda)$

is the total attenuation coefficient of the atmosphere at wavelength  $\lambda$  and it can be expressed as [55]

$$\delta(\lambda) = \alpha_m + \alpha_a + \beta_m + \beta_a \quad (2.4)$$

where  $\alpha_m$  is the molecular absorption coefficient ( $N_2$ ,  $O_2$ ,  $H_2$ ,  $H_2O$ ,  $CO_2$ ,  $O_3$ , etc., please refer to the structure and the composition of the atmosphere).  $\alpha_a$  are the absorption coefficient of the aerosols (fine solid or liquid particles) present in the atmosphere (ice, dust, smoke, etc.).  $\beta_m$  is the Rayleigh scattering coefficient resulting from the interaction of light with particles of size smaller than the wavelength.  $\beta_a$  is the Mie scattering coefficient, it appears when the incident particles are of the same order of magnitude as the wavelength of the transmitted wave [56].

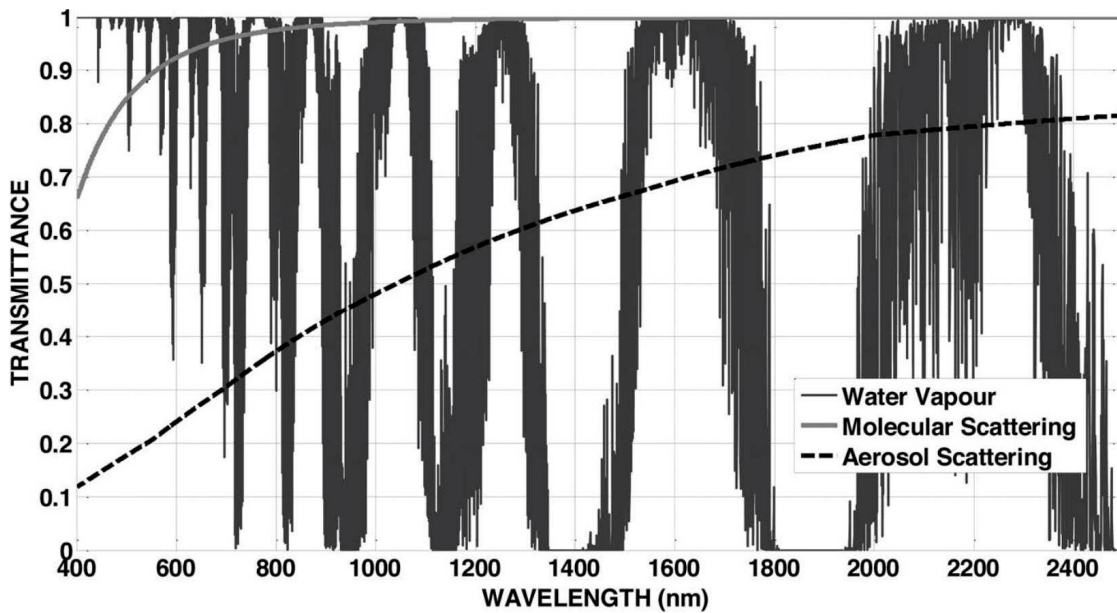


Figure 2.12: Effect of water vapour, molecular scattering, and aerosol scattering over different optical wavelength [5].

Absorption occurs when a photon of radiation is absorbed by a gaseous molecule ( $\alpha_m \gg \alpha_a$ ) of the atmosphere that converts the photon into kinetic energy [26]. Atmospheric absorption is wavelength-dependent, leading to having a range of wavelengths with minimal absorption. For that reason, most FSO systems are designed to operate in the windows of 780 - 850 nm and 1520 - 1600 nm due to the absorption is less than 0.2 dB/km [57]. Figure 2.12 depicts the effect of water vapour, molecular

scattering, and aerosol scattering over the optical wavelength range of 400 nm - 2500 nm by using the MODTRAN simulation [5]. The simulation result is analyzed over a horizontal path of 10 km at sea level. From this result, we can see that the wavelength of the FSO system should be carefully selected in the **atmospheric transmission window**, i.e., 850 nm, 1300 nm, and 1550 nm, to maintain a minimal absorption.

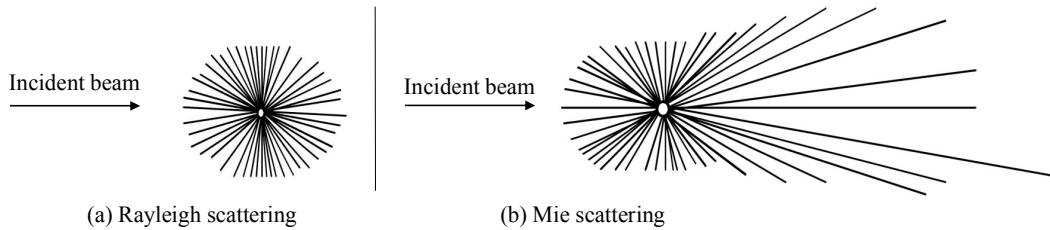


Figure 2.13: Scattering phenomena: (a) Rayleigh scattering and (b) Mie scattering.

Light scattering occurs when the radiation propagates through certain air molecules and particles. Scattering is strongly wavelength-dependent, but there is no loss of energy like in absorption [26]. Depending on the characteristic size of the particles, denoted as  $r$  and the wavelength, one description is given as  $x_0 = \frac{2\pi r}{\lambda}$ , which helps to distinguish the light scattering as follow:

- *Rayleigh scattering* ( $x_0 \ll 1$ ) caused by air particles that are small in comparison with the wavelength (see Fig. 2.13a). The shorter wavelengths are scattered much more than longer wavelengths. Fortunately, FSO systems operating in the longer wavelength, hence, the impact of Rayleigh scattering on the transmission signal can be neglected.
- *Mie scattering* ( $x_0 \approx 1$ ) occurs for atmospheric particles about the size of the wavelength. Unlike Rayleigh scattering, Mie scattering is concentrated in the forward direction as shown in Fig. 2.13b. FSO system severely suffers from fog, haze, and pollution particles which are major contributors to Mie scattering process. For example, the optical power loss can reach 350 dB/km in very dense fog conditions [57].
- *Geometric scattering* ( $x_0 \gg 1$ ) is mentioned if the particle size is much larger than the wavelength (i.e., more than about 10 times). For the Geometric scat-

tering, rain and snow are the main scatters, and FSO transmission is relatively unaffected [58].

### 2.3.3. Geometric and Misalignment Losses

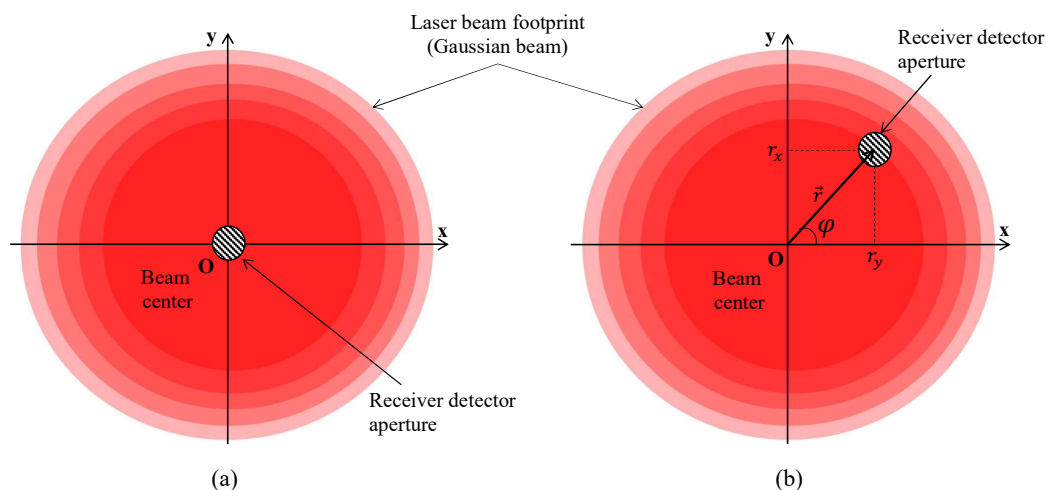


Figure 2.14: (a) Without misalignment and (b) with misalignment between the center of the optical beam footprint and receiver detector.

As the optical beam propagates through the atmosphere, a beam divergence is caused by diffraction near the receiver aperture. Some fraction of the transmitted beam will not be collected by the receiver and that will cause beam geometrical loss. This loss can be calculated given the divergence angle, the link distance, and the receiver lens aperture size. In calculating the geometric loss, an important factor is the optical wave propagation model. For vertical FSO transmissions, a good approximation is to consider a Gaussian profile for the beam intensity [26]. When a Gaussian beam has a relatively large divergence, its statistical properties are close to the case of a point source. In such a case, the approximations of plane or spherical wave can effectively be used [58].

In general, an optical source with narrow beam divergence is preferable. The narrow beam divergence, however, causes the link to fail if there is a slight misalignment between transmitter and receiver. Misalignment occurs in practice mostly due to beam wander, building sway, satellite vibration, UAV hovering, or error in the track-

ing system. An example of the misalignment loss is depicted in Fig. 2.14, in which the cases of without and with the misalignment between the centers of optical beam footprint and receiver detector are shown in Fig. 2.14(a) and (b), respectively. In the situation using Gaussian beam, the misalignment further increases the geometric loss. In the short range communications (i.e., less than one kilometer), the use of spatially partially coherent Gaussian beams has been further proposed to mitigate the misalignment-induced pointing error [59]. For a long distances, i.e., the optical satellite communication, the use of automatic pointing and tracking mechanism at the receiver becomes necessary to allow the beam well focused at the receiver detector.

### 2.3.4. Cloud Attenuation

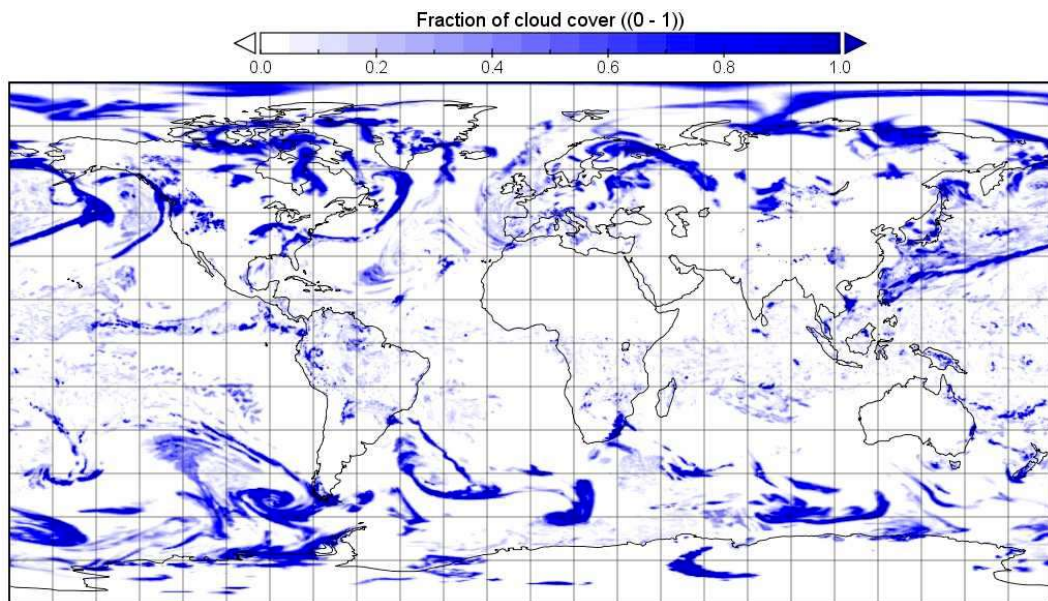


Figure 2.15: An example of global map of the fraction of sky covered by clouds.

Clouds are a visible aggregate of minute droplets of water or particles of ice or a mixture of both floating in the air. They form mostly when moist warm air is ascending to the sky then cooled down. The earth's surface is 50% covered with clouds at any given time which leads to strongly impact to the optical satellite communications. The study of clouds and their effects was advancing [60], the need of a more comprehensive classification was growing. The latest, namely International Cloud Atlas, categorized into four main types based on the altitude of the cloud's base from the

ground:

- *High-level clouds*: The altitude is approximately between 5 and 13 km at mid-latitudes. In this level, clouds consist of ice crystals. Cloud types include: Cirrus, Cirrostratus, and Cirrocumulus.
- *Mid-level clouds*: The height is 2 - 7 km at mid-latitudes. Clouds present with primarily made of water droplets and ice crystals. Cloud types in this category include: Altocumulus, Altostratus, and Nimbostratus.
- *Low-level clouds*: The height is less than 2 km at mid-latitudes. Clouds mainly composed of water droplets. Cloud types include: Cumulus, Cumulonimbus, Stratus, and Stratocumulus.
- *Vertically developed clouds*: Turbulent structures generated through either thermal convection and usually associated with precipitation. Typical clouds type are Cumulus (Cu) and Cumulonimbus (Cb).

In this dissertation, the focus will be on the clouds with high water content near the ground such as stratus, Stratocumulus, Cumulus, and so on. That is because clouds that are forming at other altitudes would consist mostly of ice particles, which is much greater than the optical wavelength, and therefore the attenuation would be negligible. In clouds, the size of air particles approximate optical wavelengths; the attenuation is significant due to the Mie scattering phenomenon. Hence, cloud attenuation is one of the major problems lies in attenuation of the laser beam. The cloud attenuation is proportional to the wavelength and depends on the profile of the liquid water content (i.e., the mass of liquid water present in the unit volume of air) across the propagation path. The optical properties of the atmosphere are deeply affected by the concentration and size. Specifically, the presence of opaque clouds may occasionally disrupt the signal or completely block the optical signal from satellite. These intermittent blockages can last from few seconds to several hours depending on the geographical location and season. Clouds offers significant attenuation as high

as tens of dB and therefore require necessary actions to combat the signal loss due to cloud coverage.

**Cloud Coverage:** Understanding the distribution of cloud coverage plays an essential role in planning and designing the FSO-based satellite communication systems for global connectivities. In fact, the cloud coverage distribution depends on the latitude, climate, season, and environment (e.g., land or sea). Figure 2.15 illustrates a global map of cloud coverage at a specific time. This map are drawn from the numerical weather prediction (NWP) data produced by ECMWF [27]. Here, the fraction of cloud cover data is depicted with spatial resolution of  $0.75^\circ \times 0.75^\circ$  pixel. Additionally, clouds are more frequent over marine pixels due to the availability of sea water. For example, the average total cloud coverage exceeds 0.5 in about 80% of marine pixels and in 60% of continental pixels, respectively.

### 2.3.5. Atmospheric Turbulence Induced Fading

Under clear atmosphere conditions, the atmospheric attenuation can be negligible [58], but we are faced to another adverse effect known as fading. Inhomogeneities in the temperature and the pressure of the atmosphere, the atmospheric turbulence causes random fluctuations in both the amplitude and the phase of the received optical signal. Atmospheric turbulence is mainly characterized by three parameters: the inner scales  $l_0$  (order of millimeters) , the outer scales  $L_0$  (order of meters), and the index of refraction structure parameter  $C_n^2$ , widely known as turbulent strength. Normally, the outer scale is approximated as  $L_0 \rightarrow \infty$  as it has a negligible impact on turbulence in practice [26]. On the other hand, the inner scale  $l_0$  has a significant influence on the turbulence [58]. The refraction structure parameter  $C_n^2$  is altitude-dependent and is larger at lower altitudes due to the more significant heat transfer between the air and the surface [26]. Typical values for  $C_n^2$  vary from  $10^{-17} \text{ m}^{-2/3}$  (weak regime) to  $10^{-13} \text{ m}^{-2/3}$  (strong regime). Its variations depend on the location and time that can attain four orders of magnitude in daytime and almost constant in nighttime.

Laser beams experience three effects under turbulence: (1) beam wander, (2) beam spreading, and (3) beam scintillation.

- *Beam wander:* For the beam in the presence of large cells of turbulence compared to the beam diameter, the beam can be deflected randomly through the changing refractive index cells. Although wavelength-dependence is weak, the longer wavelengths is less beam wander than the shorter wavelengths. In the context of the satellite communications, beam wander is the main concern in uplink due to the beam size smaller than the turbulence cell [26].
- *Beam spreading:* When the size of turbulent cell is smaller than the beam size, the beam spreading needs to consider. In this case, the incoming laser beam is diffracted and scattered independently, resulting in distortion of the received wavefront.
- *Beam scintillation:* If the size of turbulence cell is of the order beam size, then the eddies will act like lens that will focus and de-focus the incoming beam. This will lead to redistribution of signal energy resulting in temporal and spatial irradiance fluctuations of the received signal. these intensity fluctuation of the received signal is known as scintillation. Of the three turbulence effects, FSO systems might be most affected by scintillation.

The atmosphere with the heaviest concentration of particles extends to 20 km above the Earth's surface. Hence, the downlink optical beam from the satellite propagates through the turbulence atmosphere only in the final part of the transmission path. In this case, the turbulence-induced beam wander can be ignored since the turbulence cell is of the order beam size. Hence, the optical power losses due to turbulence in the downlink are likely to be dominated by the scintillation effect, which causes the signal power fluctuation leading to the significant deterioration of system performance. To quantify the fluctuation resulting from atmospheric turbulence, the scintillation index



(SI) is frequently used in the literature and can be defined as

$$\sigma_I^2 = \frac{\mathbb{E}[I^2]}{\mathbb{E}[I]^2} - 1, \quad (2.5)$$

where  $I$  is the intensity of the received optical wave and  $\mathbb{E}[\cdot]$  denotes the expected value. Based on  $\sigma_I^2$ , the turbulence strength define weak, moderate, and strong correspond to  $\sigma_I^2 < 1$ ,  $\sigma_I^2 \approx 1$ , and  $\sigma_I^2 > [26]$ .

While SI provides a characterization of the turbulence strength, full statistical characterization has been further investigated in the literature and several statistical channel models have been proposed for the distribution of turbulence-induced fading in FSO system in general, in optical satellite communication in particular. The doubly-stochastic scintillation model is the Gamma-Gamma distribution [26, 61] which has gained a wide acceptance in the current literature. In Gamma-Gamma model, the received intensity  $I$  is considered as the product of two independent Gamma random variables  $X$  and  $Y$ , which represent the irradiance fluctuations arising from large- and small-scale turbulence, respectively. The probability density function (PDF) of atmospheric turbulence coefficient,  $I$ , can be expressed as

$$f_I(I) = \frac{2(\alpha\beta)^{\frac{\alpha+\beta}{2}}}{\Gamma(\alpha)\Gamma(\beta)} I^{\frac{\alpha+\beta}{2}-1} K_{\alpha-\beta}\left(2\sqrt{\alpha\beta I}\right) \quad (2.6)$$

where  $K_{\alpha-\beta}(\cdot)$  is the  $(\alpha - \beta)$ -th order modified Bessel function of the second kind,  $\Gamma(\cdot)$  is the Gamma function.  $\alpha$  and  $\beta$  represent the effective numbers of large- and small-scale turbulence cells and can be calculated via  $\sigma_R^2 \approx \sigma_I^2$  as follow

$$\alpha = \left[ \exp\left(\frac{0.49\sigma_R^2}{\left(1 + 1.11\sigma_R^{12/5}\right)^{7/6}}\right) \right]^{-1} \quad (2.7)$$

$$\beta = \left[ \exp\left(\frac{0.51\sigma_R^2}{\left(1 + 0.69\sigma_R^{12/5}\right)^{5/6}}\right) \right]^{-1} \quad (2.8)$$

where  $\sigma_R^2$  is the Rytov's variance. For the slant propagation path, the Rytov's variance

can be calculated in case of plane wave as

$$\sigma_R^2 = 2.25k^{\frac{7}{6}}[\sec(\zeta)]^{\frac{11}{6}} \int_{h_0}^H C_n^2(h) (h - h_0)^{\frac{5}{6}} dh \quad (2.9)$$

where  $k = \frac{2\pi}{\lambda}$  is the optical wave number,  $\zeta$  is the zenith angle,  $h_0$  is the height of the optical receiver, and  $H$  is the altitude of the optical transmitter.  $C_n^2(h)$  is the refractive-index structure parameter at the height,  $h$ , above the earth's surface. The Hufnagel Valley Boundary (HVB) is widely used to model  $C_n^2(h)$  and can be given by [57]

$$\begin{aligned} C_n^2(h) = & 0.00594 \frac{v_{wind}^2}{729} (10^{-5}h)^{10} \exp\left(-\frac{h}{1000}\right) \\ & + 2.7 \times 10^{-16} \exp\left(-\frac{h}{1500}\right) + B \exp\left(-\frac{h}{100}\right) \end{aligned} \quad (2.10)$$

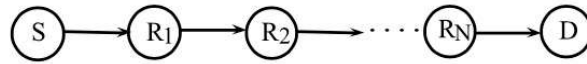
where  $v_{wind}$  is the root-mean square of the wind speed,  $C_n^2(0)$  is the turbulent strength at the ground level.

## 2.4. Performance Improvement Techniques

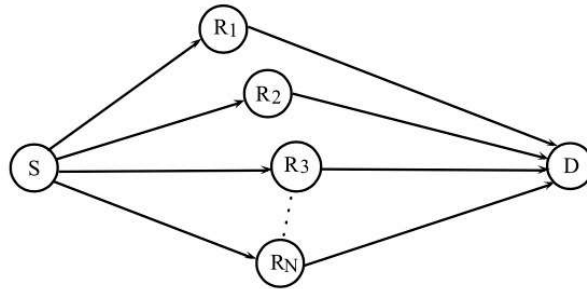
The impact of weather and atmosphere causes degradation in the quality of the received optical signal, which deteriorates the optical satellite system performance, such as outage probability, bit error rate, average transmission rate, and achievable spectrum efficiency. In order to improve the reliability of the FSO system for different atmosphere and weather conditions, various types of mitigation techniques are employed. In this section, we mainly address mitigation techniques at the physical layer including site diversity technique, relay transmission, and hybrid FSO/RF system.

### 2.4.1. Relay Transmission

Relay-assisted transmission is an effective solution for counteract the effect of the



(a) Serial relaying configuration



(b) Parallel relaying configuration

Figure 2.16: Relay transmission configuration: (a) Serial relay (b) Parallel relay [7].

weather and atmosphere. Figure 2.16 describes a relay transmission configuration including two main types: (a) serial relay and (b) parallel relay. Notably, in serial relay configuration, a signal from the source is consecutively transmitted to the destination through  $N$  relay nodes. In parallel relay configuration, the source is equipped with a multi-laser transmitter with each of the lasers pointing out to a corresponding relay node. The receiver combines all of the signals from  $N$  relay nodes to recover the original data. In both serial and parallel configurations, there are three techniques to forward the signal at relay node including: amplify-and-forward, decode-and-forward, and reflect-and-forward

- *Amplify-and-forward (AF)*: The relay amplifies both received signal and noise before forwarding to the destination.
- *Decode-and-forward (DF)*: The relay decodes and regenerates the received signal before forwarding to the destination.
- *Reflect-and-forward*: In this scheme, relay does not amplify or regenerate the signal. The relay quickly forwards the received signal to the destination by reflecting with the help of re-configurable intelligent surface (RIS).

For optical satellite communications, the main advantage of HAP are easier and faster deployment than satellite, medium operational costs, easy maintenance, and

environmental friendliness. HAP is proposed to act as a relay station to forward the high-capacity optical data through the atmosphere to the ground [3, 62]. Since HAPs are located at a cloud-free altitude, they are capable of providing reliable links between HAPs and between HAPs and satellites. In the context of satellite-to-ground systems, HAP splits the system into two parts: (i) satellite-to-HAP link where the attenuation is equal to optical beam spreading loss and (ii) HAP-to-ground link, which is affected by the weather and atmospheric conditions. DF and AF are two relaying schemes that are normally implemented at HAP [63–68].

Recently, a RIS can be mounted on a flexible UAVs, which can dynamically adapt its deployment position [69–72]. The combination of UAV and RIS offers an attractive solution for HAP-based SAGIN using hybrid FSO/RF in the presence of cloud coverage. Besides the flexible deployment, it requires less complex additional hardware than conventional relay nodes (i.e., using AF or DF at the UAV). RIS use non-mechanical, fine beam-steering devices that consist of one-dimensional array of ten of thousands of long thin electrodes to manipulate the amplitude or phase pattern of a light beam [73]. The refractive index of liquid crystal on top of a pixel electrode layer can be controlled to deflect the beam toward the intended direction with the desired angle.

### 2.4.2. Hybrid FSO/RF

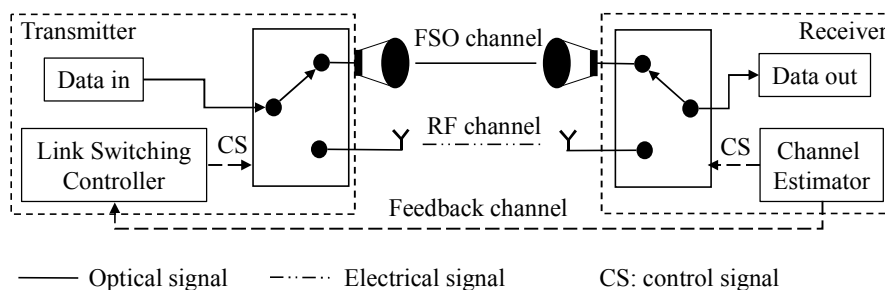


Figure 2.17: Hybrid FSO/RF system block diagram.

The weather and atmosphere conditions severely affect the optical satellite system. These effects can lead to link failures or poor performance. Therefore, it is wise to pair

an FSO system with an RF system called a hybrid FSO/RF system. FSO channel and RF channel exhibit complementary characteristics to atmosphere and weather effects. In particular, FSO performance degrades significantly due to atmospheric turbulence and cloud but is not sensitive to rain [74–76]. In contrast, the RF link is considerable susceptibility to rain, but it is indifferent to turbulence and cloud. Therefore, FSO and RF transmission systems are good candidates for joint deployment to provide reliable high-data-rate wireless transmission solutions.

Figure 2.17 describes the hybrid FSO/RF system block diagram. There are several practical transmission schemes for hybrid FSO/RF systems, such as single switching-based hybrid FSO/RF transmission schemes, hybrid FSO/RF systems with adaptive combining.

- *Single switching-based hybrid FSO/RF transmission [64, 77–79]:* To keep the receiver implementation simple and lower power consumption at the receiver, the transmission occurs only on one of the links at a time. In fact, the implementation is widely adopted in commercially available hybrid FSO/RF products [58]. For the purpose of transmitting high data rate, the FSO link is given a higher priority and used for transmission whenever its link is acceptable. When the FSO link becomes unacceptable, the system will resort to the RF link.
- *Hybrid FSO/RF transmission with adaptive combining [65, 80–82]:* In this scheme, the FSO link is used as long as its link quality is acceptable. When the FSO link's quality becomes unacceptable, the system activates the RF link and applies the combining scheme (i.e., maximum ratio combining (MRC) [65], equal gain combining (EGC), selection combining (SC) [82]) on signals received from both FSO and RF links [83]. When the quality of FSO link alone becomes acceptable again, the RF link is deactivated to save power.

The key point of hybrid FSO/RF system is the estimation the channel conditions at the receiver side so that the transmitter can adapt/switch relative to the current channel state. As shown in Fig. 2.17, the channel estimator is implemented at

the receiver to estimate the channel state information (CSI) for both FSO and RF links. The CSI reflects the information regarding the received SNRs. In practice, CSI is assumed to be reliable since a strong error correction code can be used in the feedback channel [84]. Based on the available CSIs, the link selection is controlled by link switching controller as depicted in Fig. 2.17.

### 2.4.3. Rate Adaptation

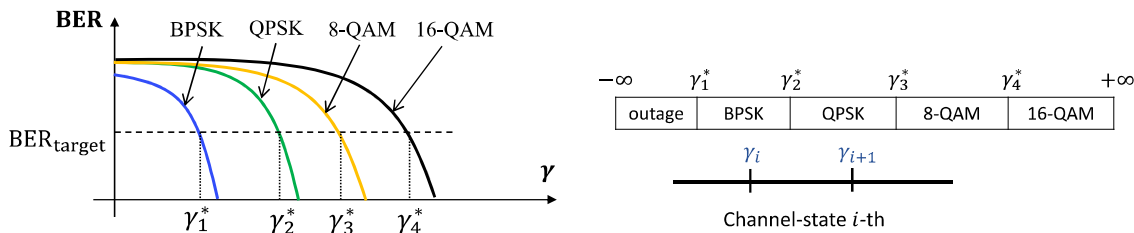


Figure 2.18: An example of the rate adaptation design for FSO-based satellite system.

The aim of the rate adaptation is to maximize the data rate over the wireless channels while satisfying a predefined quality of service (QoS), i.e., a target bit error rate (denoted as  $BER_0$ ). The key idea of the rate adaptation is to estimate the channel conditions at the receiver side and feed this channel estimate back to the transmitter using an RF feedback channel so that the transmitter can be adapted relative to the channel conditions. Besides, the temporal coherence times of the considered FSO link (order of tens of milliseconds) are relatively long compared with the time slot duration, including data transmission and feedback time (order of several milliseconds) [67]. Due to the slowly time-varying nature of fading channels, channel state information (CSI) is still up-to-date information when arriving at the destination.

An example of rate adaptation design for an FSO-based satellite system is illustrated in Fig. 2.18. To support the adaptive rate in each link, for the sake of simplicity, we employ adaptive modulation. The subcarrier  $M$ -ary quadrature amplitude modulation ( $M$ -QAM) scheme with a fixed symbol rate  $R_f$  for  $m$  possible transmission modes of the FSO link. To facilitate the data transmission using rate adaptation, the channel is modeled by multiple states defined by a range

of received signal-to-noise ratios (SNR). In particular, the range of received SNR over FSO transmission is partitioned into  $m + 1$  set of non-overlapping intervals:  $\{(-\infty, \gamma_1^*), [\gamma_1^*, \gamma_2^*), \dots, [\gamma_m^*, \infty)\}$  as shown in Fig. 2.18. Corresponding to each intervals, the transmission mode is selected for FSO link if the instantaneous SNR  $\gamma \in [\gamma_i^*, \gamma_{i+1}^*)$  with  $i \in \{1, 2, \dots, m\} = \{2\text{QAM}, 4\text{QAM}, \dots, 2^m\text{QAM}\}$ .

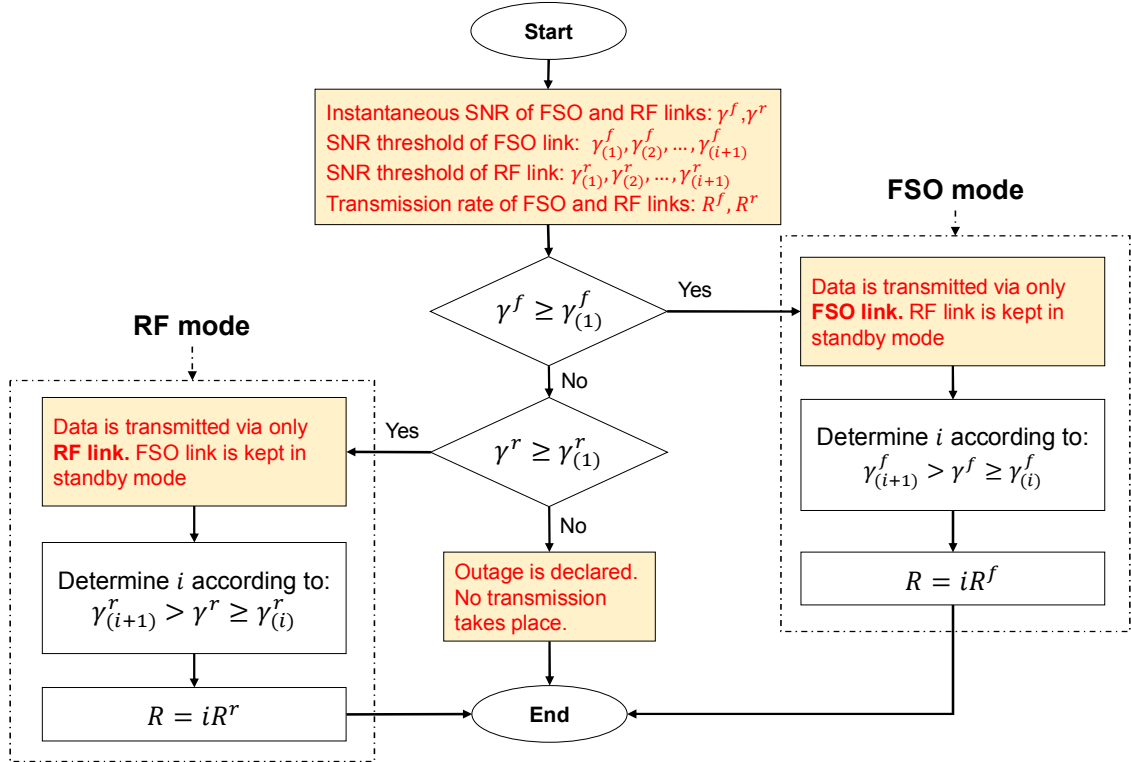


Figure 2.19: The flowchart of rate adaption for the hybrid FSO/RF system.

The operation of rate adaptation for hybrid FSO/RF system is shown in Fig. 2.19. At the start, the instantaneous SNRs of FSO and RF links, denoted as  $\gamma^f$  and  $\gamma^r$ , are estimated. In addition, the SNR thresholds of the FSO and RF links, and the transmission rate of FSO and RF links are predefined at the channel estimator. FSO link is given priority in our study; therefore, the channel estimator firstly compares the instantaneous SNR of the FSO link to the SNR threshold of the FSO link. If the instantaneous SNR of the FSO link is greater than the SNR threshold of the FSO link, the data will be transmitted via the FSO link, and the RF link will be kept in standby mode. Next, the proposed algorithm helps to determine  $i$ -index which directly decides the transmission rate of FSO link (or modulation order). Otherwise,

the channel estimator checks the RF link. If the instantaneous SNR of the RF link is greater than the SNR threshold of the RF link. The data is transmitted via the RF link, and the FSO link is kept in standby mode. The  $i$ -index is determined similarly with the FSO mode. In the case of both the instantaneous SNRs of the FSO and RF links are smaller than these thresholds, the outage will be declared. In the situation of system outage, no transmission takes places to avoid the high error rate.

In our proposed algorithm, the link switching between FSO mode and RF mode is designed to counteract the weather effect, which strongly impacts the optical satellite system. Hence, the decision link switching depends on the conditions of the weather-related issue. To avoid frequent link switching, a timer is used to assist the decision-making of link switching. When the FSO channel gets worse, the timer will be turned on to count how long the instantaneous SNR of the FSO links is below the predefined threshold. If the time is higher than a set time, the link switching mechanism will be executed, and the RF link will be selected. For example, on a sunny day, there is no cloud in the sky; the atmospheric turbulence is strong due to the inhomogeneity between temperature and pressure on the ground. The set time for the timer can be the order of milliseconds. On a cloudy day with weak turbulence, the set time for the timer can be the order of ten seconds due to the slowly changing cloud coverage. After making a decision, the channel estimator sends a feedback signal (relates to select FSO or RF link to transmit the data or system outage) to the source. Depending on the transmission distance between the source and the destination, the feedback time can be estimated. For example, the speed of light approximates  $3 \times 10^8$  (m/s) and the transmission distance is 500 km, then, the feedback time can be estimated as  $1.67 \times 10^{-3}$  s.

#### 2.4.4. Diversity Technique

Site diversity technique is one of the techniques used to improve the link availability of satellite communications by limiting weather effects, particularly those caused by cloud coverage. A diversity scheme is typically required when using laser communi-



cations from the satellite. The downlink transmissions of satellites cover very large areas, that will have different weather. The site diversity technique consists of linking two or more ground stations receiving the same signal: this way, if the signal is heavily attenuated in one area, another ground station can compensate for it. For example, cloud coverage area often have a horizontal length of no more than a few kilometers, if we put the ground stations at a sufficient distance the possibility of cloud coverage in the downlink signal will be reduced. Site diversity systems have been known to minimize disruption of the optical link.

## **2.5. Summaries**

In this chapter, we briefly described the relevant background of the study, focusing on the issues from the physical layer. We showed the main challenging issues on the satellite-based FSO links, including the atmospheric attenuation, atmospheric turbulence, geometric and misalignment losses, and cloud attenuation. Then, we introduced several mitigation techniques which help to improve optical satellite communications, such as site diversity technique, relay transmission, and hybrid FSO/RF system.

# Chapter 3

## Rate Adaptation for Satellite

### Hybrid FSO/RF System

This Chapter<sup>1</sup> addresses the design of hybrid free-space optical/radio frequency (FSO/RF) systems for a high-altitude platform (HAP)-aided relaying satellite communication for mobile networks supported by unmanned aerial vehicle (UAV). While prior work primarily focused on fixed-rate design, which frequently switches between FSO and RF lead reduced the system performance, we propose a rate adaptation design that gradually adjusts the data rate in each link when its channel state fluctuates, under a target bit error rate (BER) constraint. The proposed design's downlink performance is analyzed, taking into account many challenging issues, including beam spreading loss, cloud attenuation, statistical behaviors of the atmospheric turbulence in the dual-hop channel, and pointing misalignment due to the UAV hovering. Different performance metrics are analytically derived based on channel modelings, including outage probability, average transmission rate, and achievable spectrum efficiency. In addition, the average system BER, which satisfies the design constraint, is also numerically obtained. The results quantitatively confirm the effectiveness of our proposed system

---

<sup>1</sup>The content of this Chapter was presented in part in

1. Thang V. Nguyen *et. al.*, "On the Design of Rate Adaptation for Relay-Assisted Satellite Hybrid FSO/RF Systems," IEEE Photonics Journal, Vol. 14, No. 1, pp. 1-11, Feb. 2022.

under the impact of UAV hovering misalignment and atmospheric-related issues like clouds and turbulence.

## 3.1. Introduction

According to the International Telecommunication Union (ITU) report in 2019, half of the world population did not have regular Internet access [85]. The main barriers come from a lack of infrastructure and affordability. Satellite communications have recently emerged as a complementary solution to bridge the gap by offering Internet connectivity at a reasonable cost, and ubiquitous coverage [86]. For example, Starlink presently offers Internet access from space with a fee of 99 USD per month (unlimited data); download speed varies from 50 to 150 Mbps depending on the location [87].

As satellite communication is susceptible to weather-related issues (e.g., clouds, rain, atmospheric turbulence), it is still challenging to increase the data rate and the coverage area. A promising solution is to use a high-altitude platform (HAP), which is a quasi-stationary vehicle located at a cloud-free atmospheric altitude from 17 to 25 km above the earth's surface [3]. Thanks to unique properties, such as quick deployment, low maintenance cost, and broader coverage, the development of HAP-assisted satellite can further improve the scalability of the 5G network and beyond [88–90]. In a HAP-assisted satellite network, a swarm of HAP can be deployed to cover a vast area, e.g., approximately 100 km as expected by Softbank [91]. Besides, HAP can be a stand-alone system to provide a stable connection to a remote area, temporary link to emergencies situations, such as a natural disaster, as described in Fig. 3.1. Furthermore, unmanned aerial vehicles (UAVs) as mobile base stations can further enhance the Internet connectivity provision as they can flexibly adjust their positions based on the demand on the ground. The UAV-mounted mobile base station solution has gained significant interest in both academic, and industry [92,93]. In case of natural disaster, UAVs can promptly give warnings, rapidly assist rescue and temporarily recover the operation of damaged communication networks [92].

In the considered network, HAP functions as a relay station between the satellite and

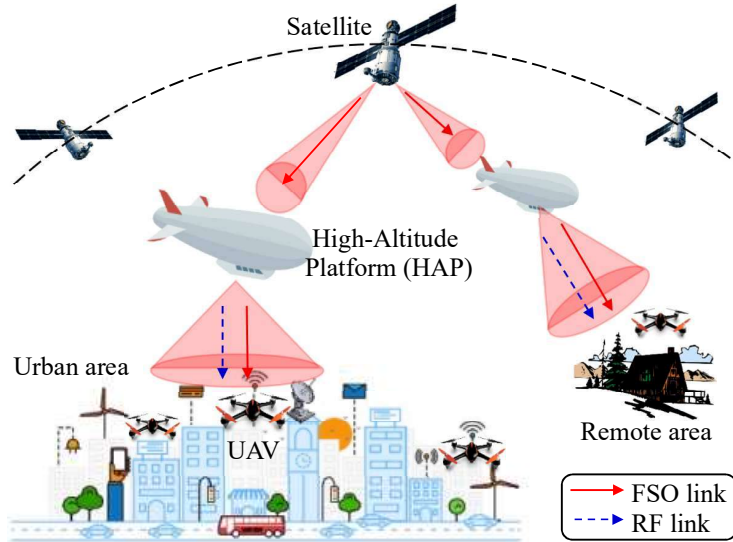


Figure 3.1: HAP-assisted satellite network with UAVs.

UAVs. The system, therefore, consists of two links: (1) a satellite-to-HAP and (2) HAP-to-UAV links. As the HAP situates in the stratosphere, which is less susceptible to atmospheric turbulence and clouds, we employ a free-space optical (FSO) link from satellite to HAP for a high-speed connection. In the second hop between HAP and UAVs, the FSO link may face weather-related issues such as clouds, snow, haze, rain, atmospheric turbulence, etc., which reduce link availability and limit the link distance [94]. In addition, multiple UAVs can be supported by one HAP; UAVs' locations are therefore not necessarily in the center of the optical beam. Also, UAVs can be in mobility; the optical link outage may occur because of the combined effect of beam misalignment and UAV hovering. Therefore, a hybrid FSO/RF system is proposed, in which the FSO link is prioritized higher. The RF is used as a backup link when the optical channel condition is insufficient to maintain the high data rate. As a matter of fact, the dual-hop relay-assisted FSO and hybrid FSO/RF communications have been well studied for terrestrial networks [95–97]. In the satellite networks, the current state-of-the-art of hybrid FSO/RF systems for relay-assisted satellite communication focuses on fixed users [63–65,68,98]. In particular, in [63], the authors studied the downlink satellite-HAP-ground with the assumption of gamma-gamma turbulence channel model for FSO link and Rician distribution for RF link.

The impact of pointing error and atmospheric attenuation was not included in the study. The hybrid FSO/RF for uplink ground-HAP-satellite scenarios was considered in [64], in which the RF channel was also modeled by Rician distribution. The combined channel model for the FSO link was taken into account free space loss, atmospheric turbulence, and beam wander induced pointing error. In both [63,64], the single-threshold-based scheme was used to switch between RF and FSO links. The adaptive-combining-based switching scheme was used for integrated satellite-HAP-ground with hybrid FSO/RF system in both cases of uplink and downlink [65, 98]. The maximal-ratio-combining of FSO and RF links was implemented at the receiver when the RF link was transmitted simultaneously with the FSO link. Nevertheless, all previous work did not consider the case of mobile users, such as UAV-mounted mobile base stations, which are being considered for irregular, unexpected events, including sports events, natural disasters, and emergencies. In addition, the adaptive rate hybrid FSO/RF system was recently applied for the downlink satellite-HAP-ground [68]. With the help of the rate adaptation, the hybrid FSO/RF system can avoid frequently switching between FSO link and RF link, leading to enhancing the system performance.

In this paper, we, therefore, attempt to provide a comprehensive design and an insightful evaluation of dual-hop satellite-HAP-UAV hybrid FSO/RF systems with rate adaptation for mobile users, which can be summarized as follows:

- *Firstly*, we propose a multi-rate design for the integrated downlink satellite-HAP-UAV with the help of hybrid FSO/RF systems to counteract the effect of transmission media. As the role of the relay node, the amplified and forward scheme is implemented at HAP thanks to its cost-effectiveness and simple hardware requirements.
- *Secondly*, a number of performance metrics, including the end-to-end outage probability, average transmission rate, and achievable spectrum efficiency, have been derived considering various atmospheric-related issues. Specifically, the Rician distribution is used to model the RF channel. The FSO channel is

modeled by taking into account the atmospheric turbulence, which is modeled by Gamma-Gamma distribution, cloud attenuation, beam spreading loss, and UAV hovering misalignment. The Monte-Carlo simulation verifies the accuracy of the theoretical model.

- *Finally*, from the perspective of practical design, the insightful numerical results are discussed to quantify the effect of transmission media on the dual-hop satellite-HAP-UAV hybrid FSO/RF system. To this end, we have demonstrated the effectiveness of the proposed system compared with the conventional ones.

The rest of this Chapter is organized as followed. The relay-assisted satellite hybrid FSO/RF communication system description is shown in Section 3.2. In Section 3.3, the FSO and RF channel models are investigated. Next, Section 3.4 presents rate adaptation and analyzes the system performance concerning the average transmission rate, achievable spectrum efficiency, outage probability, and average bit error rate. The discussion on the numerical results is expressed in Section 4.5. Finally, the critical points of our work are concluded in Section 4.6.

## 3.2. System Descriptions

Figure 3.2 describes a block diagram of dual-hop satellite-HAP-UAV with an FSO system at first hop and hybrid FSO/RF system at the second hop. In the considered system, the satellite is a source node. The HAP is a relay node that amplifies the received signal from the satellite then forwards it to the destination. The UAV-mounted base station is a destination node. At the transmitter, the data is modulated by a quadrature amplitude modulation (QAM) modulator, and the output signal can be expressed as

$$s_n(t) = A_{nI}g(t) \cos(2\pi f_r t) - A_{nQ}g(t) \sin(2\pi f_r t), \quad (3.1)$$

where  $g(t)$  is the pulse shaping function,  $f_r$  is the sub-carrier frequency,  $0 \leq t \leq T$  with  $T$  is the interval time of the QAM symbol,  $A_{nI} = \{2n - 1 - I\}_{n=1}^I$  and  $A_{nQ} =$

### 3.2 System Descriptions

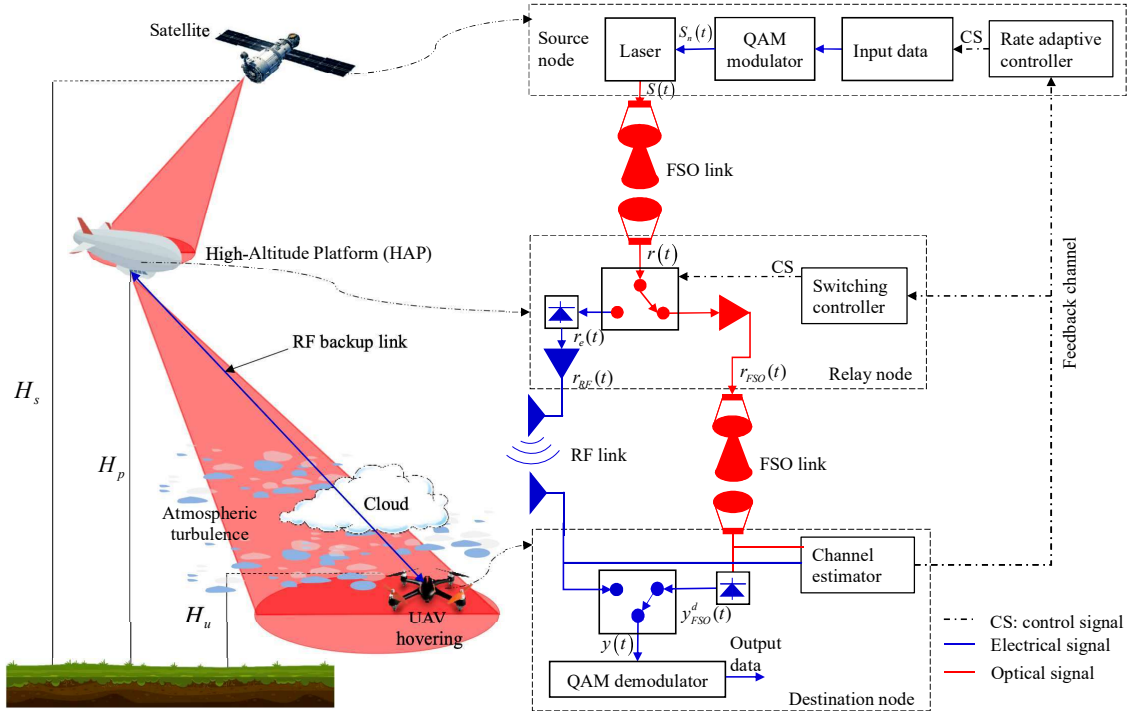


Figure 3.2: The dual-hop satellite-HAP-UAV hybrid FSO-FSO/RF systems including challenge issues (left side) and block diagram (right side).

$\{2n - 1 - Q\}_{n=1}^Q$  are the amplitude of the information signal belong to in-phase and quadrature, respectively. Then, the electrical QAM signal is used to modulate the intensity of optical beam to generate the SC-QAM optical signal, which can be shown as

$$s(t) = P_t [1 + m s_n(t)], \quad (3.2)$$

where  $P_t$  is the transmitted power at the satellite,  $m$  is the modulation index. At the HAP, i.e., relay node, the optical aperture collects the optical signals then forwards them to an optical switch. Based on channel state information (CSI), the signal is decided to transmit RF or FSO link in the next state. If the RF link is selected, the optical signal is converted to the electrical signal by photodiode then amplify before transmitting to the destination node. If the FSO link is chosen, the optical signal is amplified and directly forward to the ground station. The representative of the output signal of the relay node can be expressed as

**For RF link:**

$$r_r(t) = G_{\text{RF}} [\eta h_{\text{SR}} P_t m s_n(t) + \eta n_{\text{b1}} + n_{\text{re.hap}}], \quad (3.3)$$

**For FSO link:**

$$r_f(t) = G_{\text{F}} [h_{\text{SR}} s(t) + n_{\text{b1}}], \quad (3.4)$$

where  $\eta$  is the optical-to-electrical coefficient,  $h_{\text{SR}}$  is the beam spreading loss at the first hop,  $n_{\text{b1}}$  is the background noise, and  $n_{\text{re.hap}}$  is the receiver noise,  $G_{\text{RF}}$  is the electrical amplifier gain,  $G_{\text{F}}$  is the optical amplifier gain. Based on CSI, the FSO link will be activated if the channel quality is good. Otherwise, the RF link will be applied if the channel condition is poor. The received signal at the ground station can be expressed as

**For RF link:**

$$y_r(t) = h_{\text{RF}} G_{\text{RF}} \eta h_{\text{SR}} P_t m s_n(t) + h_{\text{RF}} G_{\text{RF}} \eta n_{\text{b1}} + h_{\text{RF}} G_{\text{RF}} n_{\text{re.hap}} + n_{\text{re}}. \quad (3.5)$$

**For FSO link:**

$$y_f(t) = h_{\text{FSO}} \eta G_{\text{F}} h_{\text{SR}} P_t m s_n(t) + \eta h_{\text{FSO}} G_{\text{F}} n_{\text{b1}} + \eta n_{\text{b2}} + n_{\text{rec}}, \quad (3.6)$$

where  $h_{\text{RF}}$  and  $h_{\text{FSO}}$  are the channel coefficient of the RF link and the FSO link, respectively.  $n_{\text{re}}$  and  $n_{\text{rec}}$  are receiver noise. For convenient,  $G_{\text{RF}}^2 = \frac{1}{(P_t m h_{\text{SR}})^2 + (\sigma_{\text{b1}})^2}$  and  $G_{\text{F}}^2 = \frac{1}{(P_t m h_{\text{SR}})^2 + (\sigma_{\text{b1}})^2}$ , the SNR at the destination node, denoted as  $\gamma_f^{e2e}$  for FSO-FSO link and  $\gamma_r^{e2e}$  for FSO-RF link, can be given as

**For FSO-RF link:**

$$\begin{aligned} \gamma_{e2e}^r &= \frac{(h_{\text{RF}} G_{\text{RF}} \eta h_{\text{SR}} P_t m)^2}{(h_{\text{RF}} G_{\text{RF}} \eta \sigma_{\text{b1}})^2 + (h_{\text{RF}} G_{\text{RF}} \sigma_{\text{re.hap}})^2 + (\sigma_{\text{re}})^2}, \\ &= \frac{\gamma_1 \gamma_{2,\text{RF}}}{\gamma_1 + \gamma_{2,\text{RF}} + 1}. \end{aligned} \quad (3.7)$$



**For FSO–FSO link:**

$$\begin{aligned}\gamma_{e2e}^f &= \frac{(h_{\text{FSO}}\eta G_{\text{F}}h_{\text{SR}}P_{\text{t}}m)^2}{(h_{\text{FSO}}\eta G_{\text{F}}\sigma_{\text{b1}})^2 + (\eta\sigma_{\text{b2}})^2 + (\sigma_{\text{rec}})^2}, \\ &= \frac{\gamma_1\gamma_{2,\text{FSO}}}{\gamma_1 + \gamma_{2,\text{FSO}} + 1}.\end{aligned}\quad (3.8)$$

where  $\gamma_1 = \frac{(P_{\text{t}}mh_{\text{SR}})^2}{(\sigma_{\text{b1}})^2}$  is the SNR of FSO link at the first hop. In the second hop,  $\gamma_{2,\text{RF}} = \frac{(\eta h_{\text{RF}})^2}{(h_{\text{RF}}G_{\text{RF}}\sigma_{\text{re.hap}})^2 + (\sigma_{\text{re}})^2}$  is the SNR of the RF link. And,  $\gamma_{2,\text{FSO}} = \frac{(\eta h_{\text{FSO}})^2}{(\eta\sigma_{\text{b2}})^2 + (\sigma_{\text{rec}})^2}$  is the SNR of FSO link at the second hop.

### 3.3. Channel Modeling

The integrated satellite-HAP-UAV system considered in this Chapter contains two hops: (1) satellite-to-HAP using FSO links, and (2) HAP-to-UAV using hybrid FSO/RF links. This section investigates the challenging factors for each hop separately.

#### 3.3.1. Satellite-to-HAP FSO link

Due to the relative motion between satellite and HAP, unfortunately, the Doppler effect may affect received signals. Nevertheless, the existing receiver design for optical satellite communication is able to deal with the Doppler frequency shift as reported in [99, 100]. Hence, the effect of Doppler can be negligible in our work. On the other hand, the impact of clouds and atmospheric turbulence on laser beam can be ignore since HAP situates at cloud-free altitude (i.e., 17-25 km) as described above. Besides, an optical Gaussian beam is diverged by some amount over the path from the satellite to HAP. The divergence loss is computed as the ratio between the fraction of collected power of HAP's aperture and the area of beam footprint. For a single beam, the divergence loss can be approximately calculated as

$$L_{\text{geo}} \approx A_0 \exp\left(-\frac{2\rho^2}{w_{\text{deq}}^2}\right), \quad (3.9)$$

where  $w_{deq}^2 = w_d^2 \frac{\sqrt{\pi} \operatorname{erf}(v)}{2v \exp(-v^2)}$  is the equivalent beam waist, in which  $w_d = w_0 \sqrt{1 + \varepsilon \left( \frac{\lambda d_1}{\pi w_0^2} \right)^2}$  is the beam waist at the distance  $d_1$ , which is given by  $d_1 = (H_s - H_p)/\cos(\xi_s)$  in which  $H_s$  is the altitude of the satellite,  $H_p$  is the height of the HAP, and  $\xi_s$  is the zenith angle of the satellite,  $w_0 = (2\lambda)/(\pi\theta_s)$  is the beam waist at  $d_1 = 0$  with  $\theta_s$  is the divergence angle of the satellite,  $\varepsilon = \left( 1 + 2 \frac{w_0^2}{\rho_0^2(d_1)} \right)$ , and  $\rho_0(d_1) = (0.55 C_n^2 k_w^2 d_1)^{-3/5}$  is the coherence length [101]. In this study, we assume that active tracking between the satellite and the HAP is perfect, then the detector of HAP is located at the center of beam footprint (i.e.,  $\rho = 0$ ). Hence,  $A_0 = [\operatorname{erf}(v)]^2$  corresponds to the fraction of the collected power at  $\rho = 0$  with  $v = \frac{a\sqrt{\pi}}{w_d\sqrt{2}}$  is the ratio between aperture radius and beam-width, in which  $a$  is the radius of detector.

### 3.3.2. HAP-to-UAV hybrid FSO/RF link

#### 3.3.2.1. RF channel

The Rician distribution is used to model the RF channel due to line-of-sight (LOS) transmission between HAP and UAV. The channel coefficient of the RF link can be given as  $h_{RF} = g_1 h_r$ , where  $g_1$  and  $h_r$  denote the average power gain and fading gain of the RF link, respectively. The power gain of the RF link can be expressed as

$$g_1 \text{ (dB)} = G_T + G_R - L_F - L_A - L_c, \quad (3.10)$$

where  $G_T$  and  $G_R$  are the transmit and receive antenna gains, respectively.  $L_A$  denotes the gaseous atmosphere loss [64].  $L_F = 20 \log_{10} \left( \frac{4\pi d_2}{f_r} \right)$  is the free space loss from the HAP to UAV, in which  $f_r$  is the frequency for RF link, and  $d_2 = (H_p - H_u)/\cos(\xi_p)$  is the transmission distance from HAP to UAV with HAP's zenith angle of  $\xi_p$ , and  $H_u$  is the altitude of UAVs.

*Cloud effects:* As introduced by ITU-P840 [102], the cloud attenuation model is based on Rayleigh scattering suitable for frequencies up to 200 GHz, and it is expressed as

$$L_c = d_c \alpha_1, \quad (3.11)$$

where  $L_c$  is the attenuation due to effect of cloud, in which  $d_c = d_z / \cos \xi_p$  is the signal path propagation in clouds, in which  $d_z$  is the considered length of clouds.  $\alpha_1 = K_c M_c$  is the specific attenuation within clouds in which  $K_c$  ((dB/km)/(g/m<sup>3</sup>)) is the specific attenuation coefficient,  $M_c$  (g/m<sup>3</sup>) is the cloud liquid water content [102].

*Rician fading model:* Due to LOS between HAP and UAV, and following [103, 104], the fading gain is then modeled by Rician distribution with the probability density function (PDF) and cumulative density function (CDF) of the SNR received at the destination can be given respectively by

$$f_{\gamma_{2,RF}}(\gamma_{2,RF}) = \frac{K+1}{\bar{\gamma}_{RF}} I_0 \left( 2\sqrt{\frac{K(K+1)\gamma_{2,RF}}{\bar{\gamma}_{RF}}} \right) \times \exp \left[ -\frac{(K+1)\gamma_{2,RF}}{\bar{\gamma}_{RF}} - K \right]. \quad (3.12)$$

$$F_{\gamma_{2,RF}} = 1 - Q_1 \left( \sqrt{2K}, \sqrt{\frac{2(K+1)}{\bar{\gamma}_{RF}} \gamma_{2,RF}} \right), \quad (3.13)$$

where  $Q_1(\cdot, \cdot)$  is the Marcum  $Q_1$ -function,  $K$  is the Rician factor which reflects the relative strength of the direct LOS path component of fading coefficient.  $\bar{\gamma}_{RF}$  is the average SNR of the RF link.

#### 3.3.2.2. FSO channel

For the downlink from HAP to UAV, the mathematical model of channel coefficient is expressed as  $h_{FSO} = h_c h_a h_p$  in which  $h_c$  is the cloud attenuation,  $h_a$  is turbulence-induced fading, and  $h_p$  is UAV hovering-induced fading.

*Cloud effects:* In the optical downlink, atmospheric attenuation is severe due to scattering, which is caused by clouds [25, 57, 105, 106]. Clouds result from the condensation of water vapors above the earth's surface and may occasionally disrupt the signal or completely block the optical signal from HAP to UAV. Besides, optical wavelength, which operates in THz band corresponds to the range of wavelength from 0.8 to 2  $\mu m$ , is about the same particle size of water vapors. Hence, the scattering phenomenon

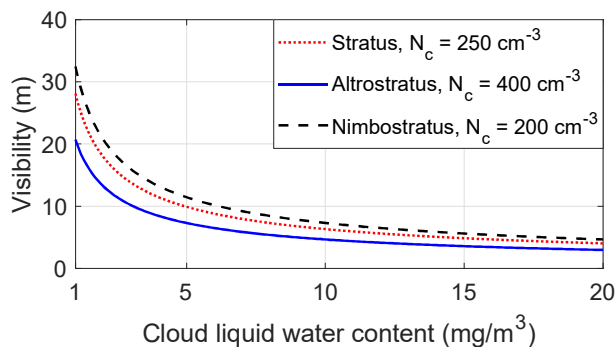


Figure 3.3: An example of the visibility for several cloud types.

occurs on the beam propagation, leading to decrease visibility significantly and signal power [25,106]. In this model, the visibility can be determined based on cloud droplet number concentration  $N_c$  and cloud liquid water content  $M_c$  as followed [107]

$$V = \frac{1.002}{(N_c \times M_c)^{0.6473}}. \quad (3.14)$$

The cloud effects on the visibility is illustrated in Fig. 3.3 for various cloud types such as stratus ( $N_c = 250 \text{ cm}^{-3}$ ), altostratus ( $N_c = 400 \text{ cm}^{-3}$ ), and nimbostratus ( $N_c = 200 \text{ cm}^{-3}$ ). The figure reveals that visibility decreases rapidly when the CLWC grows up. Following the Beer-Lambert law, the cloud attenuation can be expressed [25]

$$h_c = \exp(-\alpha_2 d_c), \quad (3.15)$$

where  $d_c$  is the distance regarding scattering phenomena happen.  $\alpha_l$  is the attenuation coefficient and can be expressed as

$$\alpha_2 = \frac{3.91}{V [km]} \left( \frac{\lambda [nm]}{550} \right)^{-q}, \quad (3.16)$$

where  $q$  is the coefficient, which is given by Kim's model [25].

*Turbulence-induced fading:* The Gamma-Gamma distribution is used for modeling the turbulence from weak regime to strong regime. The PDF of the turbulence coefficient

can be expressed

$$f_{h_a}(h_a) = \frac{2(\alpha\beta)^{\frac{\alpha+\beta}{2}}}{\Gamma(\alpha)\Gamma(\beta)} h_a^{\frac{\alpha+\beta}{2}} K_{\alpha-\beta}\left(2\sqrt{\alpha\beta h_a}\right), \quad (3.17)$$

where  $\Gamma(\cdot)$  is the gamma function and  $K_v(\cdot)$  is the  $v$ -th order modified Bessel function of the second kind. In addition,  $\alpha$  and  $\beta$  can be found in [57], which is the function of Rytov variance,  $\sigma_R^2$ , and for the plane wave,  $\sigma_R^2$  can be given as

$$\sigma_R^2 = 2.25k_w^{7/6} \sec^{11/6}(\xi_p) \int_{H_u}^{H_p} C_n^2(h) (h - H_u)^{5/6} dh, \quad (3.18)$$

where  $k_w = 2\pi/\lambda$  is the optical wave number. Based on Hufnagel-Valley model [57], the variation of refractive index structure parameter  $C_n^2(h)$  according to the altitude  $h$  can be written as

$$C_n^2(h) = 0.00594 \left(\frac{v_{wind}}{27}\right)^2 (10^{-5}h) \exp\left(-\frac{h}{1000}\right) + 2.7 \times 10^{-16} \exp\left(-\frac{h}{1500}\right) + C_n^2(0) \exp\left(-\frac{h}{100}\right), \quad (3.19)$$

where  $C_n^2(0)$  is the ground turbulence level varying in the range of  $10^{-17}\text{m}^{-2/3}$  (weak turbulence regime) to  $10^{-13}\text{m}^{-2/3}$  (strong turbulence regime), and  $v_{wind}$  (m/s) is the root mean squared wind speed with typical value of 21 m/s [57].

*UAV hovering misalignment model:* Pointing error is mainly caused by the wind pushing the UAV around its operating position shown in Fig. 3.4. The HAP, on the contrary, is assumed to remain stable as it is located at a much higher altitude where there is little wind. The hovering results in a change of position of the UAV aperture. Note that the UAV's position is not necessarily in the center of the beam footprint for the purpose of serving multiple UAVs at the same time. Let  $r$  be the radial vector from the beam center to the UAV's initial position. Due to the wind, UAV hovers around  $r_h$  radial to another position. Consequently, the actual position can be a  $r_{pe}$  radial distance from the beam footprint, and it can be expressed in the coordinate

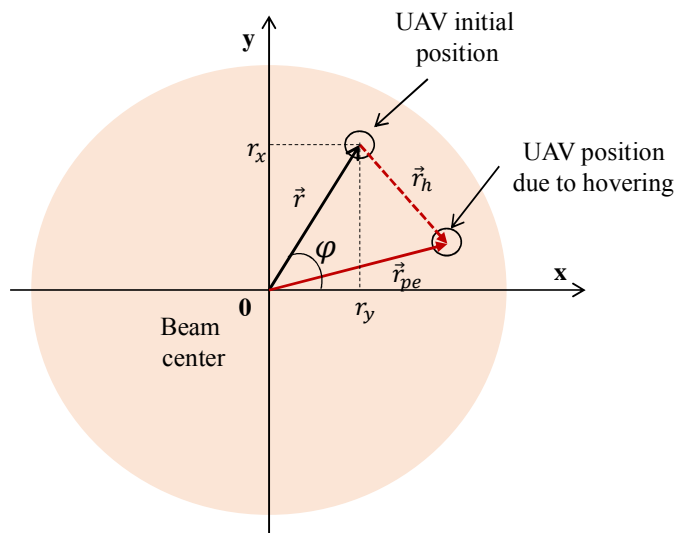


Figure 3.4: UAV hovering misalignment model.

plane as followed

$$r_{pe}(x_{r_{pe}}, y_{r_{pe}}) = \begin{cases} x_{r_{pe}} = r_x + x_{r_h} = \|r\| \sin(\varphi) + x_{r_h}, \\ y_{r_{pe}} = r_y + y_{r_h} = \|r\| \cos(\varphi) + y_{r_h}, \end{cases} \quad (3.20)$$

where  $\|\cdot\|$  is the norm of a vector,  $x_{r_h}$  and  $y_{r_h}$  are zero-mean Gaussian random variables (RVs) with variance  $\sigma_p^2$ . Besides,  $x_{r_{pe}}$  and  $y_{r_{pe}}$  are two statistically independent Gaussian RVs as  $x_{r_{pe}} \sim \mathcal{N}(r_x, \sigma_p^2)$  and  $y_{r_{pe}} \sim \mathcal{N}(r_y, \sigma_p^2)$ . As reported in [19], the variance of  $x_{r_{pe}}$  and  $y_{r_{pe}}$  are the same and equal  $\sigma_p^2$ , the PDF of radial displacement  $r_{pe}$  follows Rician distribution

$$f_{r_{pe}}(r_{pe}) = \frac{r_{pe}}{\sigma_p^2} \exp\left[-\frac{(r_{pe}^2 + r^2)}{2\sigma_p^2}\right] I_0\left(\frac{r_{pe}r}{\sigma_p^2}\right), \quad (3.21)$$

where  $I_0(\cdot)$  is the modified Bessel function of the first kind with order zero,  $\sigma_{pe}^2$  is the jitter variance. By considering the Gaussian beam, the UAV hovering misalignment coefficient can be expressed as

$$h_{pe} = B_0 \exp\left(-\frac{2r_{pe}^2}{w_{zeq}^2}\right), \quad (3.22)$$

### 3.3 Channel Modeling

where  $B_0 = [\text{erf}(v_2)]^2$  is the fraction of the collected power by UAV's detector at  $r_{pe} = 0$ .  $w_{zeq}^2 = \frac{\sqrt{\pi}\text{erf}(v_2)}{2v_2 \exp(-v_2^2)} w_z^2$  is the equivalent beam-width,  $v_2 = \frac{a_2 \sqrt{\pi}}{w_z \sqrt{2}}$  in which  $a_2$  is the radius of detector,  $w_z \approx w_{z0} \sqrt{1 + \varepsilon_2 \left( \frac{\lambda d_2}{\pi w_{z0}^2} \right)^2}$  is the beam waist at the distance  $d_2$ ,  $w_{z0}$  is the beam waist at  $d_2 = 0$ ,  $\varepsilon_2 = \left( 1 + 2 \frac{w_{z0}^2}{\rho_{z0}^2(d_2)} \right)$ , and  $\rho_{z0}(d_2) = (0.55 C_n^2 k_w^2 d_2)^{-3/5}$  is the coherence length. As derived in [19, 108], the PDF of pointing error  $h_{pe}$  can be expressed as

$$f_{h_p}(h_p) = \frac{w_{deq}^2}{4A_0\sigma_p^2} \exp\left(-\frac{r^2}{2\sigma_p^2}\right) \left(\frac{h_p}{A_0}\right)^{\frac{w_{deq}^2}{4\sigma_p^2}} \times I_0\left(\frac{r}{\sigma_p^2} \sqrt{-\frac{w_{deq}^2}{2} \ln\left(\frac{h_p}{A_0}\right)}\right), \quad (3.23)$$

*Joint PDF and CDF of combined channel:* After mathematical manipulation, the joint distribution of the channel coefficient  $h_{FSO}$  can be expressed as

$$\begin{aligned} f_{h_{FSO}}(h_{FSO}) &= \sum_{i=1}^n 4x_i w_i \frac{(\alpha\beta)^{\frac{\alpha+\beta}{2}}}{\Gamma(\alpha)\Gamma(\beta)} \exp\left(-\frac{r^2}{4\sigma_p^2}\right) \left(\frac{1}{A_0 h_c}\right)^{\frac{\alpha+\beta}{2}} I_0\left(\frac{r x_i}{\sigma_p}\right) \\ &\times \exp\left[\frac{4x_i^2 \sigma_p^2 (\alpha + \beta)}{w_{zeq}^2}\right] K_{\alpha-\beta}\left(2\sqrt{\frac{\alpha\beta h_{FSO}}{A_0 h_c} \exp\left(\frac{8x_i^2 \sigma_p^2}{w_{zeq}^2}\right)}\right) h_{FSO}^{\frac{\alpha+\beta}{2}-1}. \end{aligned} \quad (3.24)$$

where  $x_i$  and  $w_i$  are the weights and the zeros of the Hermite polynomial, respectively. As reported in [19], the PDF of received SNR of FSO channel from HAP to UAV can be expressed

$$\begin{aligned} f_{\gamma_{2,FSO}}(\gamma_{2,FSO}) &= \sum_{i=1}^n 2x_i w_i \frac{(\alpha\beta)^{\frac{\alpha+\beta}{2}}}{\Gamma(\alpha)\Gamma(\beta)} \exp\left(-\frac{r^2}{2\sigma_p^2}\right) k_{pe}^{\frac{\alpha+\beta}{2}} \\ &\times \exp\left[\frac{2x_i^2 \sigma_p^2 (\alpha + \beta)}{w_{Leq}^2}\right] I_0\left(\frac{r\sqrt{2}x_i}{\sigma_p}\right) \left(\frac{1}{\gamma_{2,FSO}}\right)^{\frac{\alpha+\beta}{4}} \\ &\times K_{\alpha-\beta}\left(2\sqrt{\alpha\beta k_{pe} \sqrt{\frac{\gamma_{2,FSO}}{\gamma_{2,FSO}}} \exp\left(\frac{4x_i^2 \sigma_p^2}{w_{Leq}^2}\right)}\right) \gamma_{2,FSO}^{\frac{\alpha+\beta}{4}-1}. \end{aligned} \quad (3.25)$$

By applying [109, Eq.(8.4.23)], [110, Eq. (26)], and after several mathematical manipulations, the CDF of the SNR of FSO link can be shown as in Eq. (3.26), in which the value of  $k_{pe}$  can be found in [19].

$$\begin{aligned}
F_{\gamma_{2,FSO}}(\gamma_{2,FSO}) &= \sum_{i=1}^n 2x_i w_i \frac{(\alpha\beta)^{\frac{\alpha+\beta}{2}}}{\Gamma(\alpha)\Gamma(\beta)} \exp\left(-\frac{r^2}{2\sigma_p^2}\right) k_{pe}^{\frac{\alpha+\beta}{2}} \\
&\times \exp\left[\frac{2x_i^2\sigma_p^2(\alpha+\beta)}{w_{Leq}^2}\right] I_0\left(\frac{r\sqrt{2}x_i}{\sigma_p}\right) \left(\frac{\gamma_{2,FSO}}{\bar{\gamma}_{2,FSO}}\right)^{\frac{\alpha+\beta}{4}} \\
&\times G_{1,3}^{2,1}\left[\alpha\beta k_{pe} \exp\left(\frac{4x_i^2\sigma_p^2}{w_{Leq}^2}\right) \sqrt{\frac{\gamma_{2,FSO}}{\bar{\gamma}_{2,FSO}}}\left|\begin{matrix} 1 - \frac{\alpha+\beta}{2} \\ \frac{\alpha-\beta}{2}, \frac{-\alpha+\beta}{2}, -\frac{\alpha+\beta}{2} \end{matrix}\right.\right]. \quad (3.26)
\end{aligned}$$

### 3.4. Rate Adaptation Design

This section focuses on the design of rate adaptation for our proposed systems. Several performance metrics are then derived in our analysis, including outage probability, average transmission rate, achievable spectrum efficiency, and average bit error rate.

#### 3.4.1. Adaptive Transmission Schemes

The purpose of the adaptive multi-rate scheme is to maximize the data rate over the wireless channels while satisfying a predefined quality of service (QoS). To support the data-rate selection, a channel estimator is designed at the destination (i.e., UAVs) to estimate the channel state information (CSI) for both FSO and RF links, as illustrated in Fig. 3.2. The CSI reflects the information regarding the selection of both transmission rates and links based on the estimated received SNRs. In our study, for the sake of simplicity in the analysis, the feedback channel carrying CSI information is assumed to be reliable<sup>2</sup>. In addition, the temporal coherence times of considered FSO [111] and RF [112] links, i.e., in the order of tens of milliseconds, are relatively long in comparison with the time slot duration, including the data transmission and feedback time (order of several milliseconds). Due to the slowly time-varying nature of fading channels, CSIs are still up-to-date information when arriving at the HAP and satellite. Based on the available CSIs, the selection of data rate and link for transmissions are controlled by the satellite's rate-adaptive controller and HAP's switching controller, respectively.

<sup>2</sup>In practice, a strong error correction code can be used in the feedback channel [84].



In our system design, the high-speed FSO link is considered as a primary link, while the RF link is used as a backup when the quality of the FSO link becomes unacceptable, e.g., due to the strong turbulence or cloud coverage. The design of rate adaptation is applied for both FSO and RF links to increase the data rate while satisfying a pre-defined QoS, i.e., a targeted bit error rate (denoted as  $\text{BER}_0$ ). We adopt the subcarrier  $M$ -array quadrature amplitude modulation ( $M$ -QAM) scheme with a fixed symbol rate of  $R_f$  for  $m$  possible transmission modes of the FSO link. Similarly, the  $N$ -QAM scheme is also applied to the RF link with a fixed symbol rate of  $R_r$  for  $n$  possible transmission modes. To facilitate the data transmission using rate adaptation, the channel is modeled by multiple states defined by a range of received signal-to-noise ratio (SNR). In particular, the range of received SNRs over FSO transmission is partitioned into  $m + 1$  set of non-overlapping intervals:  $\{(-\infty, \gamma_{e2e}^{f(1)}), [\gamma_{e2e}^{f(1)}, \gamma_{e2e}^{f(2)}), \dots, [\gamma_{e2e}^{f(m)}, +\infty)\}$ , in which the transmission mode  $i$ -th is selected for FSO link if the instantaneous SNR  $\gamma_{e2e}^f \in [\gamma_{e2e}^{f(i)}, \gamma_{e2e}^{f(i+1)})$  with  $i \in \{1, 2, \dots, m\}$ . To avoid a high error rate, no FSO transmission is allowed when  $\gamma_{e2e}^f < \gamma_{e2e}^{f(1)}$ . In this case, the RF link using  $n$  transmission modes is activated.<sup>3</sup> The range of received SNRs over RF transmission is divided into  $n + 1$  set of non-overlapping intervals:  $\{(-\infty, \gamma_{e2e}^{r(1)}), [\gamma_{e2e}^{r(1)}, \gamma_{e2e}^{r(2)}), \dots, [\gamma_{e2e}^{r(n)}, +\infty)\}$ , in which the transmission mode  $j$ -th is selected for RF link if the instantaneous SNR  $\gamma_{e2e}^r \in [\gamma_{e2e}^{r(j)}, \gamma_{e2e}^{r(j+1)})$  with  $j \in \{1, 2, \dots, n\}$ ; no RF transmission is allowed to avoid high error rate when  $\gamma_{e2e}^r < \gamma_{e2e}^{r(1)}$ . If both the FSO and RF links happen to be in standby mode (i.e.,  $\gamma_{e2e}^f < \gamma_{e2e}^{f(1)}$  and  $\gamma_{e2e}^r < \gamma_{e2e}^{r(1)}$ ), the hybrid FSO/RF system goes into outage. In summary, the data bit rate for each link changes for every transmission mode and is given as

$$R = \begin{cases} R_f \log_2 M, & \text{if } \gamma_{e2e}^{f(i)} \leq \gamma_f < \gamma_{e2e}^{f(i+1)}, & \text{FSO link,} \\ R_r \log_2 N, & \text{if } \gamma_{e2e}^{r(j)} \leq \gamma_r < \gamma_{e2e}^{r(j+1)}, & \text{RF link,} \\ 0, & \text{if } \gamma_{e2e}^f < \gamma_{e2e}^{f(1)}; \gamma_{e2e}^r < \gamma_{e2e}^{r(1)}, & \text{Outage,} \end{cases}$$

---

<sup>3</sup>Whenever the quality of the FSO link becomes acceptable, the system switches back to this link, and the RF link is put on the standby mode.

where  $M = 2^i$  with  $i \in \{1, 2, \dots, m\}$  and  $N = 2^j$  with  $j \in \{1, 2, \dots, n\}$ . What remains now is to determine the SNR threshold levels for both FSO and RF transmissions. These threshold levels are obtained based on the fact that the BER for each transmission mode satisfies the targeted  $\text{BER}_0$ . Specifically, for a link using  $\mathcal{K}$ -QAM modulation, it is formulated as [113]

$$\text{BER}(\mathcal{K}, \gamma) \cong 0.2 \exp \left[ -\frac{3\gamma}{2(\mathcal{K}-1)} \right] \triangleq \text{BER}_0, \quad (3.27)$$

where  $\mathcal{K} = M$  and  $\gamma = \gamma_{e2e}^{f(i)}$  for the FSO link, while  $\mathcal{K} = N$  and  $\gamma = \gamma_{e2e}^{r(j)}$  for the RF link. From (3.27), the SNR threshold levels for FSO and RF links can be obtained as

$$\gamma = \frac{-2(\mathcal{K}-1)}{3} \ln(5\text{BER}_0). \quad (3.28)$$

An example of rate adaptation design for hybrid FSO/RF system is illustrated in Table 3.1, in which  $m = n = 3$  transmission modes for FSO and RF links.

Table 3.1: An example of rate adaptation design for hybrid FSO/RF systems.

		RF (active): Backup Link			FSO (active): Primary Link		
		1	2	3	1	2	3
Transmission Mode		BPSK	QPSK	8-QAM	BPSK	QPSK	8-QAM
Modulation		BPSK	QPSK	8-QAM	BPSK	QPSK	8-QAM
Data Rate	0	$2R_r$	$3R_r$	$4R_r$	$2R_f$	$3R_f$	$4R_f$
Thresholds (dB)	<b>FSO</b>	Outage of FSO $(-\infty, \gamma_{e2e}^{f(1)})$					
	<b>RF</b>	Outage of RF $(-\infty, \gamma_{e2e}^{r(1)})$	$[\gamma_{e2e}^{r(1)}, \gamma_{e2e}^{r(2)})$	$[\gamma_{e2e}^{r(2)}, \gamma_{e2e}^{r(3)})$	$[\gamma_{e2e}^{r(3)}, +\infty)$	$[\gamma_{e2e}^{f(1)}, \gamma_{e2e}^{f(2)})$	$[\gamma_{e2e}^{f(2)}, \gamma_{e2e}^{f(3)})$

### 3.4.2. Performance Analysis

1) *Outage probability*: The outage occurs when the system moves to the zero-rate mode, in which no data is transmitted to avoid the high error rate. The outage probability is then defined as [95]

$$\begin{aligned} P_{\text{out}} &= \int_0^{\gamma_{e2e}^{f(1)}} f_{\gamma_{e2e}^f}(\gamma_{e2e}^f) d\gamma_{e2e}^f \int_0^{\gamma_{e2e}^{r(1)}} f_{\gamma_{e2e}^r}(\gamma_{e2e}^r) d\gamma_{e2e}^r \\ &= F_{\gamma_{e2e}^f}(\gamma_{e2e}^f) F_{\gamma_{e2e}^r}(\gamma_{e2e}^r), \end{aligned} \quad (3.29)$$

where  $\gamma_{e2e}^{f(1)}$  and  $\gamma_{e2e}^{r(1)}$  are the outage thresholds for corresponding FSO and RF links, adopted in Table 3.1 by the SNR thresholds of lowest transmission modes for such links.  $F_{\gamma_{e2e}^r}(\gamma_{e2e}^r)$  and  $F_{\gamma_{e2e}^f}(\gamma_{e2e}^f)$  are respectively the CDFs of end-to-end for the dual-hop of FSO-RF and FSO-FSO, which are expressed as

**For FSO-RF link:**

$$F_{\gamma_{e2e}^r}(\gamma_{e2e}^r) = \Pr\left(\frac{\gamma_1 \gamma_{2,\text{RF}}}{\gamma_{2,\text{RF}} + 1} < \gamma_{e2e}^r\right) = F_{\gamma_{2,\text{RF}}}\left(\frac{\gamma_{e2e}^r}{\gamma_1 - \gamma_{e2e}^r}\right). \quad (3.30)$$

**For FSO-FSO link:**

$$F_{\gamma_{e2e}^f}(\gamma_{e2e}^f) = \Pr\left(\frac{\gamma_1 \gamma_{2,\text{FSO}}}{\gamma_{2,\text{FSO}} + 1} < \gamma_{e2e}^f\right) = F_{\gamma_{2,\text{FSO}}}\left(\frac{\gamma_{e2e}^f}{\gamma_1 - \gamma_{e2e}^f}\right). \quad (3.31)$$

2) *Average transmission rate*: The average transmission rate, which is an essential parameter in adaptive multi-rate systems, can be determined as

$$\bar{R} = \sum_{k=1}^N p_k R_k, \quad (3.32)$$

where  $N$  is the total modes. Since the transmission rate of each link is fixed, the link switching threshold is designed based on targeted BER, then the fixed  $M$ -QAM is used. Mode probability is defined as the probability that  $k$ -th mode is selected; then it can be calculated as

**For FSO-RF link**

$$\begin{aligned}
 p_k^{RF} &= \int_0^{\gamma_{e2e}^{f(1)}} f_{\gamma_{e2e}^f}(\gamma_{e2e}^f) d\gamma_{e2e}^f \int_{\gamma_{e2e}^{r(j)}}^{\gamma_{e2e}^{r(j+1)}} f_{\gamma_{e2e}^r}(\gamma_{e2e}^r) d\gamma_{e2e}^r \\
 &= \left[ 1 - F_{\gamma_{e2e}^f}(\gamma_{e2e}^{f(1)}) \right] \left[ F_{\gamma_{e2e}^r}(\gamma_{e2e}^{r(j+1)}) - F_{\gamma_{e2e}^r}(\gamma_{e2e}^{r(j)}) \right]. \quad (3.33)
 \end{aligned}$$

**For FSO-FSO link**

$$p_k^{FSO} = \int_{\gamma_{e2e}^{f(i)}}^{\gamma_{e2e}^{f(i+1)}} f_{\gamma_{e2e}^f}(\gamma_{e2e}^f) d\gamma_{e2e}^f = F_{\gamma_{e2e}^f}(\gamma_{e2e}^{f(i+1)}) - F_{\gamma_{e2e}^f}(\gamma_{e2e}^{f(i)}). \quad (3.34)$$

3) *Spectrum efficiency*: As the system is in the state  $k$ -th, each transmitted symbol carries  $R_k$  information bits. We suppose that a Nyquist pulse shaping filter with the bandwidth  $B = 1/R_0$ . Then, the achievable spectral efficiency, defined as the data rate per unit bandwidth, is given by

$$S_{\text{eff}} = \frac{1}{R_0} \sum_{k=1}^N p_k R_k. \quad (3.35)$$

4) *Average bit error rate (ABER)*: The ABER is defined as the ratio of the average number of erroneously received bits over the total average number of transmitted bits, which is expressed by

$$\text{ABER} = \frac{\text{Total erroneous bits}}{\text{Total transmitted bits}} = \frac{\sum_{k=1}^N R_k p_k \text{BER}_k}{\sum_{k=1}^N R_k p_k}, \quad (3.36)$$

where  $R_k$  is the transmission rate at state  $k$ -th,  $\text{BER}_k$  is the bit error rate of selecting mode  $k$ -th over fading channel, which can be determined as

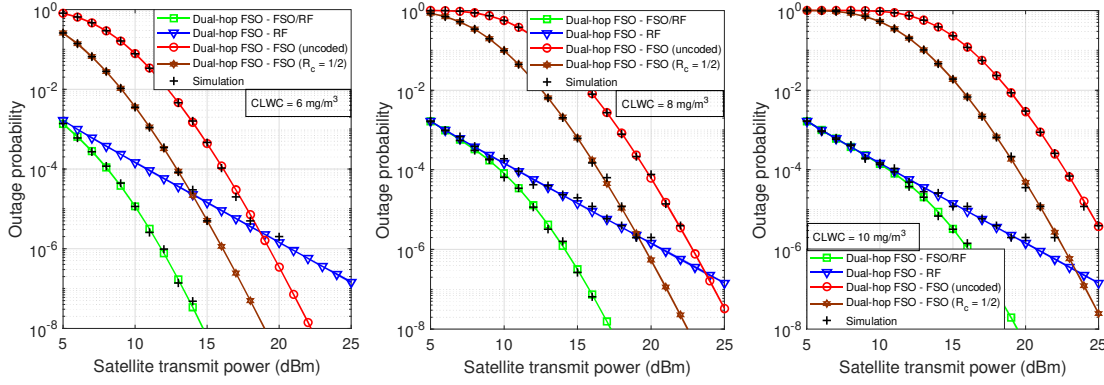


Figure 3.5: Outage performance versus satellite's transmitted power for different CLWCs at the UAV's position of 20 m.

### For FSO-FSO link

$$\text{BER}_{fso} = \frac{1}{p_k^{FSO}} \int_{\gamma_{e2e}^{f(k)}}^{\gamma_{e2e}^{f(k+1)}} \text{BER}(M, \gamma_{e2e}^f) f_{\gamma_{e2e}^f}(\gamma_{e2e}^f) d\gamma_{e2e}^f. \quad (3.37)$$

### For FSO-RF link

$$\text{BER}_{rf} = \frac{1}{p_k^{RF}} \int_{\gamma_{e2e}^{f(k)}}^{\gamma_{e2e}^{f(k+1)}} \text{BER}(N, \gamma_{e2e}^r) f_{\gamma_{e2e}^r}(\gamma_{e2e}^r) d\gamma_{e2e}^r. \quad (3.38)$$

where  $\text{BER}(M, \gamma_{e2e}^f)$  and  $\text{BER}(N, \gamma_{e2e}^r)$  are given in Eq. (3.27).

### 3.4.3. Conventional Hybrid FSO/RF Design

In conventional hybrid FSO/RF systems, the transmission rate of each link is fixed, where the link switching mechanism is based on a predefined  $\text{BER}_0(M, \gamma)$ . In other words, the system works on two modes: FSO and RF ones. It is supposed that a fixed  $M$ -QAM and  $N$ -QAM are used for FSO and RF modes, respectively. The SNR thresholds for such FSO and RF links obtained from (4.33) are, then, expressed as  $\gamma_{e2e}^{f(i)}$  and  $\gamma_{e2e}^{r(j)}$ , where  $i = \log_2(M)$  and  $j = \log_2(N)$ .

The primary FSO link is selected when  $\gamma_{e2e}^f \in [\gamma_{e2e}^{f(i)}, \infty)$ ; otherwise the system

switches to operate on the backup RF link with  $\gamma_{e2e}^r \in [\gamma_{e2e}^{r(j)}, \infty)$ . Therefore, the average transmission rate for such systems can be written as

$$\bar{R}_{\text{fix}} = p^{FSO} R_f + p^{RF} R_r, \quad (3.39)$$

where  $R_f$  and  $R_r$  are respectively the data bit rate of FSO and RF modes. In addition, the FSO and RF mode probabilities, denoted by  $p^{FSO}$  and  $p^{RF}$ , are defined as

$$\begin{cases} p^{FSO} &= \int_{\gamma_{e2e}^{f(i)}}^{\infty} f_{\gamma_{e2e}^f}(\gamma_{e2e}^f) d\gamma_{e2e}^f = F_{\gamma_{e2e}^f}(\gamma_{e2e}^{f(i)}), \\ p^{RF} &= (1 - p^{FSO}) F_{\gamma_{e2e}^r}(\gamma_{e2e}^{r(j)}). \end{cases} \quad (3.40)$$

On the other hand, the average BER for conventional hybrid FSO/RF systems is expressed as

$$\text{ABER}_{\text{fix}} = \frac{R_f p^{FSO} \text{BER}_{fso} + R_r p^{RF} \text{BER}_{rf}}{R_f p^{FSO} + R_r p^{RF}}, \quad (3.41)$$

where  $\text{BER}_{fso}$  and  $\text{BER}_{rf}$  are defined as

$$\begin{cases} \text{BER}_{fso} &= \int_{\gamma_{e2e}^{f(i)}}^{\infty} \text{BER}(M, \gamma_{e2e}^f) f_{\gamma_{e2e}^f}(\gamma_{e2e}^f) d\gamma_{e2e}^f, \\ \text{BER}_{rf} &= \int_{\gamma_{e2e}^{r(j)}}^{\infty} \text{BER}(N, \gamma_{e2e}^r) f_{\gamma_{e2e}^r}(\gamma_{e2e}^r) d\gamma_{e2e}^r. \end{cases} \quad (3.42)$$

## 3.5. Numerical Results

In this section, we present selected numerical results to demonstrate the advantages of our proposed adaptive hybrid FSO/RF design in the scenario of space-air-ground networks. Notably, we highlight the effectiveness of our proposed systems by comparing performance metrics analyzed in Section 3.4 with those of conventional systems, i.e., adaptive dual-hop FSO-FSO, adaptive dual-hop FSO-RF, and fixed-rate dual-hop FSO-hybrid FSO/RF designs. To this purpose, the sets of transmission modes

using  $M$ -QAM modulation with  $M \in \{2, 4, 8, 16, 32, 64, 128\}$  for FSO links and  $N$ -QAM modulation with  $N \in \{2, 4, 8, 16, 32\}$  for RF links<sup>4</sup> are adopted for the adaptive multi-rate design. For the sake of comparison, 32-QAM modulation is given for RF links, while different  $M$ -QAM modulations are considered for FSO links in the conventional fixed-rate systems. The parameters used in the analysis, unless otherwise noted, are given in Table 4.3.

Monte Carlo simulations using MATLAB are also provided to validate the analytical results. Using the system parameters outlined in Table 4.3, the simulation is done by using a discrete-event simulator. The details of simulation process are described as follows. *Regarding the FSO transmission*, with a given value of  $C_n^2(0)$ , we generate  $10^6$  independent coefficients of  $h_a$ , which have the Gamma-Gamma distribution as given in (3.17). In addition, for a given UAV's hovering jitter variance  $\sigma_p^2$ , we generate  $10^6$  independent RVs  $x_{r_{pe}}$  and  $y_{r_{pe}}$ . Then, using generated RVs  $x_{r_{pe}}$  and  $y_{r_{pe}}$ , we generate  $10^6$  independent coefficients of  $h_p$  from (3.23). Since the path loss ( $h_c$ ) is deterministic, it is generated using relations in (3.15). We then obtain  $10^6$  independent values of UAV-based FSO channel coefficient ( $h_{FSO}$ ) from  $h_{FSO} = h_c h_a h_p$  used to derive the FSO channel SNR  $\gamma_{2,FSO}$  as well as  $\gamma_{e2e}^f$  from (3.8). *As for the RF transmission*, given the Rician factor  $K$ , we generate  $10^6$  independent channel SNR  $\gamma_{2,RF}$  based on (3.12), which is used to derive  $\gamma_{e2e}^r$  from (3.7). Finally, using the obtained  $10^6$  independent values of  $\gamma_{e2e}^f$  and  $\gamma_{e2e}^r$ , the performance metrics based on Monte Carlo simulation can be found.

We first analyze the effectiveness of our proposed dual-hop FSO-hybrid FSO/RF adaptive systems by comparing with the conventional adaptive ones, including dual-hop FSO-FSO and dual-hop FSO-RF, in terms of outage performance, over a range of satellite's transmitted power in Fig. 3.5. Here, in addition to the uncoded dual-hop FSO-FSO system, we consider an additional transmission mode using BPSK with a coding rate of 1/2 as the lowest mode [114], which results in a lower outage threshold,

---

<sup>4</sup>It is worth noting that more transmission modes result in better performance while the system complexity is increased. As FSO is the primary link, the number of RF modes is, therefore, selected to be less than the FSO ones.



Table 3.2: System Parameters

Name	Symbol	Value
<b>LEO Satellite</b>		
LEO satellite altitude	$H_s$	530 km
Divergence angle	$\theta_{sat}$	15 $\mu$ rad
Optical wavelength	$\lambda$	1550 nm
RF frequency	$f_r$	2 GHz
FSO symbol rate	$R_f$	500 Msps
RF symbol rate	$R_r$	100 Msps
<b>High Altitude Platform (HAP)</b>		
HAP altitude	$H_p$	20 km
HAP aperture radius	$r_{hap}$	10 cm
Zenith angle	$\xi_p$	60°
Divergence angle	$\theta_{hap}$	1.5 mrad
<b>Unnamed Aerial Vehicle (UAV)</b>		
UAV altitude	$H_u$	100 m
Hovering jitter variance	$\sigma_p^2$	0.9 m
UAV aperture radius	$r_{uav}$	5 cm
Detector responsivity	$\mathcal{R}$	0.9
Noise standard deviation	$\sigma_n$	10 <sup>-7</sup> A/Hz
Gaseous atmosphere losses	$L_A$	5.4 × 10 <sup>-3</sup> dB/km
Receiver noise bandwidth	$BW$	74.8 dBHz
System noise temperature	$T_N$	17.6 dBK
Noise figure	$N_F$	2 dB
<b>Other Parameters</b>		
Targeted BER	$BER_0$	10 <sup>-5</sup>
Number of cloud concentrations	$N_c$	250 cm <sup>-3</sup>
Considered length of clouds	$d_z$	2 km
Turbulence at ground level	$C_n^2(0)$	10 <sup>-13</sup> m <sup>-2/3</sup>
Rician factor	$K$	6 dB

for such a system. Also, different cloud conditions, i.e., CLWC = 6 mg/m<sup>3</sup>, CLWC = 8 mg/m<sup>3</sup>, and CLWC = 10 mg/m<sup>3</sup>, which are the critical concerns, especially for FSO links, are investigated.

There are two remarkable observations here. *Firstly*, when the CLWC increases, the outage performance of dual-hop FSO-FSO systems is significantly deteriorated, even with the one using the strong coding scheme. While a minimal change is witnessed for dual-hop FSO-RF ones. The reason is that the impact of clouds is much more severe in FSO systems as the optical wavelength is smaller than the typical cloud droplet size values [99]. Contrary to optical bands, the wavelengths of RF ones are often larger

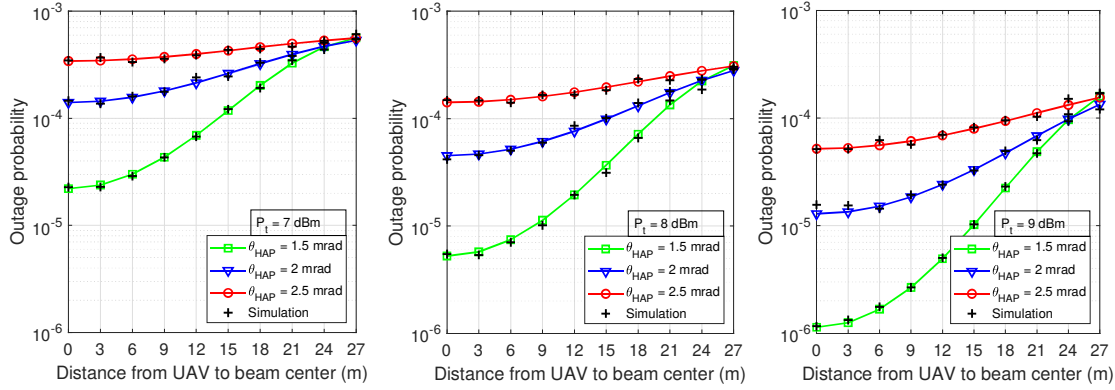


Figure 3.6: Outage probability versus satellite transmit power and distance from center of Gaussian beam to UAV position with CLWC of  $6 \text{ mg/m}^3$ .

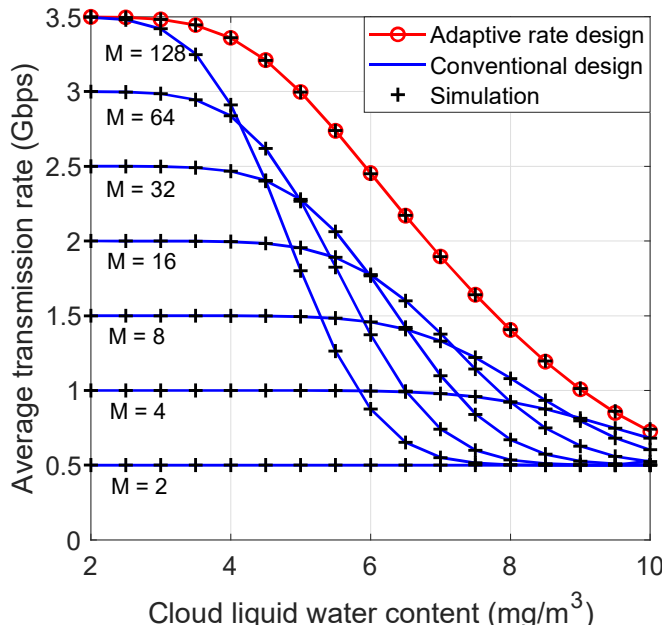


Figure 3.7: The impact of cloud to average transmission rate of adaptive rate system and fixed rate system.

than the size of cloud droplets, resulting in a very low attenuation caused by clouds on such links [102]. In addition, with high values of the satellite's transmitted power, the dual-hop FSO-FSO systems, however, can maintain a better performance than dual-hop FSO-RF ones in less severe cloud conditions, e.g.,  $\text{CLWC} = 6 \text{ mg/m}^3$  and  $\text{CLWC} = 8 \text{ mg/m}^3$ . *Secondly*, as is expected, our proposed dual-hop FSO-hybrid FSO/RF systems can provide a significant performance improvement over the conventional ones in different cloud conditions, thanks to inheriting both FSO and RF benefits.

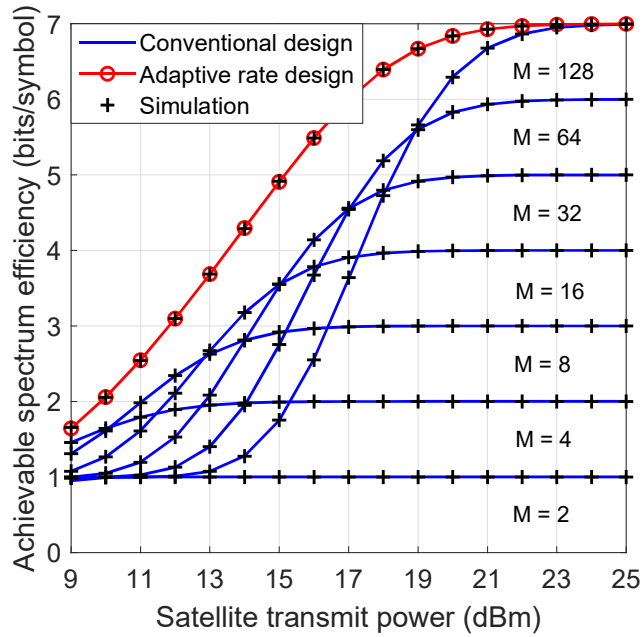


Figure 3.8: The achievable spectrum efficiency versus satellite transmit power in the case of adaptive rate system and fixed rate system.

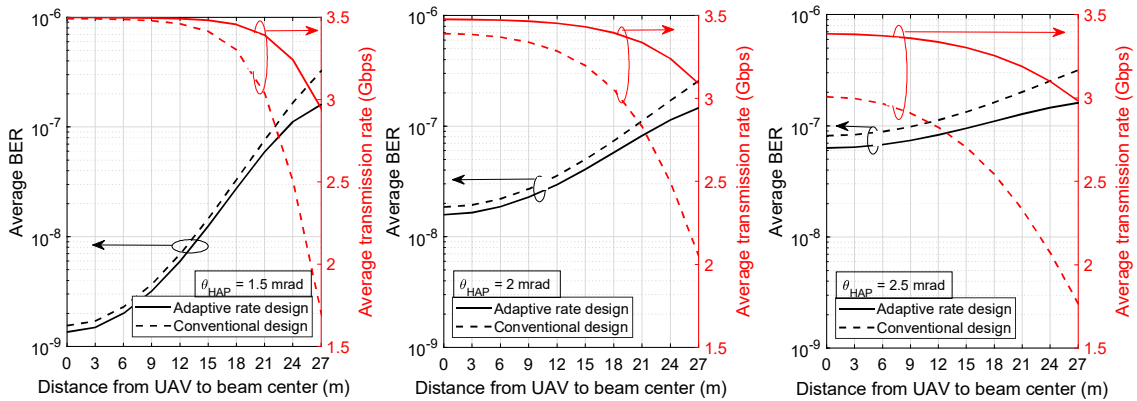


Figure 3.9: Average BER and average transmission rate versus UAV's position for different values of HAP's divergence angle.

Also, in this figure, the analytical results closely follow the simulated ones, which confirms the correctness of the model and analysis.

In Fig. 3.6, we investigate the outage performance in terms of beam footprint size provided by the HAP-based relaying node, when  $CLWC = 6 \text{ mg/m}^3$ . Also, different satellite's transmitted powers, i.e.,  $P_t = 7 \text{ dBm}$ ,  $8 \text{ dBm}$ , and  $9 \text{ dBm}$ , and HAP's divergence angles, i.e.,  $\theta_{HAP} = 1.5 \text{ mrad}$ ,  $2 \text{ mrad}$ , and  $2.5 \text{ mrad}$ , are taken into account. This is a vital performance metric to determine the system operational coverage area.

For instance, when  $\theta_{\text{HAP}} = 1.5$  mrad, to retain a target outage performance level of below  $10^{-4}$ , the operational area of UAVs should be within 15 m, 19 m, 24 m, for  $P_t = 7$  dBm, 8 dBm, and 9 dBm, respectively. In addition, the highly directional beam is obtained for smaller HAP's divergence angles, resulting in a better outage performance. Such smaller HAP's divergence angles, nevertheless, restrict the system operational areas, leading to the high outage probability at the edge of the beam footprint. As a result, there exists a tradeoff between the operational areas and system performance in the selection of HAP's divergence angles.

Next, we further analyze the advantages of our proposed adaptive multi-rate design compared to the conventional systems with fixed-rate schemes. Specifically, Fig. 3.7 investigates the achievable data rate over a range of CLWCs, when  $P_t = 15$  dBm. Obviously, compared to the fixed-rate scheme, the adaptive multi-rate design could offer considerably better performance under the impact of cloud coverage. This fact can be explained from two remarkable points: (i) the systems with high modulation order could maintain a high maximum achievable data rate in less severe cloud conditions; (ii) the performance of such systems using high modulation order is significantly degraded in more severe cloud conditions, in which low modulation order is preferable in this situation, leading to the limitation of maximum achievable data rate. As a result, systems using a fixed-rate scheme may not be efficient in time-varying channels, and adaptive multi-rate design would be the promising solution. For example, when  $\text{CLWC} = 6 \text{ mg/m}^3$ , our proposed adaptive system can achieve 2.45 Gbps of data rate, while the fixed-rate one could only retain the data rate of 1.77 Gbps, 1.45 Gbps, 1.37 Gbps, 0.99 Gbps, and 0.5 Gbps with 32-QAM, 8-QAM, 64-QAM, 128-QAM, 2-QAM modulations used for the FSO links, respectively. The outperformance of the proposed adaptive multi-rate design over the conventional fixed-rate one can also be observed in Fig. 3.8 in which variations in achievable spectrum efficiency performance with different values of the satellite's transmitted power when  $\text{CLWC} = 6 \text{ mg/m}^3$ . For instance, when  $P_t = 20$  dBm, our proposed design can achieve the spectrum efficiency of 6.8 bits/symbol, while they are only 6.2 bits/symbol, 5.8 bits/symbol, 4.9

bits/symbol, 4 bits/symbol, 3 bits/symbol, 2 bits/symbol, 1 bits/symbol for respectively 128-QAM, 64-QAM, 32-QAM, 16-QAM, 8-QAM, 4-QAM, 2-QAM with the fixed-rate one.

Finally, we highlight the effectiveness of our proposed adaptive design by comparing the average BER performance with that of conventional fixed-rate one, over a range of beam footprint sizes, as illustrated in Fig. 3.9. Also,  $P_t = 20$  dBm, CLWC =  $6 \text{ mg/m}^3$ , and different HAP's divergence angles, i.e.,  $\theta_{\text{HAP}} = 1.5$  mrad, 2 mrad, and 2.5 mrad, are considered. It is noted that the obtained results of BER are based on their exact-form expressions found in (3.36) and (3.41) for respectively the proposed and conventional designs. As expected, our proposed design offers a lower average BER performance compared to the conventional one, even with higher achievable data-rate transmissions. This phenomenon is due to the fact that the objective of adaptive multi-rate design is to maximize the data rate over the time-varying turbulence-induced fading channels while satisfying a pre-defined Quality of Service (QoS), i.e., a targeted BER. Moreover, using this figure, we can decide the operational range of UAVs to maintain a targeted BER performance by selecting a proper HAP's divergence angle parameter, which is an especially essential parameter for mobile users. For example, to retain a level of BER performance of below  $10^{-7}$ , the operational area of UAVs should be within 24 m, 22 m, and 17 m for  $\theta_{\text{HAP}} = 1.5$  mrad, 2 mrad, and 2.5 mrad, respectively.

## 3.6. Conclusions

We have proposed the adaptive hybrid FSO/RF design and a comprehensive analytical framework for the performance of HAP-aided relaying satellite communications for mobile networks supported by UAVs. For hybrid FSO/RF channels, the Rician distribution was adopted for RF links. At the same time, several factors were taken into account on FSO links, including atmospheric turbulence modeled by the Gamma-Gamma distribution, the cloud coverage, and the UAV hovering-induced pointing misalignment. Several system performance metrics, including outage probability, av-

verage transmission rate, and achievable spectrum efficiency, were analytically derived. Through the numerical results, there are several concluding remarks: (i) Our proposed system could offer a significant performance improvement compared to the existing designs in the scenario of integrated downlink satellite-HAP-ground/vehicles, i.e., adaptive design (dual-hop FSO-FSO and dual-hop RF-RF) and fixed-rate design (dual-hop FSO-hybrid FSO/RF); (ii) Our results could support the proper parameter selection for practical mobile users, i.e., beam size provided by HAP and satellite's transmitted power; and (iii) the correctness of our analytical model was confirmed by the Monte Carlo simulations, in which the excellent agreement between theoretical results and simulated ones was validated.

Our study could be a generalized framework for relay-based satellite-assisted vehicular networks, with UAVs and other vehicles, e.g., high-speed trains and autonomous cars. Future work would be interesting to investigate other adaptive schemes, i.e., power adaptation, which is especially essential to save energy consumption in the domain of satellite and/or vehicular networks.

# Chapter 4

## RIS-UAV Relay Assisted SAGIN

This Chapter<sup>5</sup> studies the satellite-ground integrated network (SAGIN) using hybrid FSO/RF links, and unmanned aerial vehicle (UAV), high altitude platform (HAP) as relaying nodes. SAGIN has been widely envisioned as a promising network architecture for 6G. In the SAGINs, high altitude platform (HAP)-aided relaying satellite systems using hybrid free-space optics (FSO)/radio-frequency (RF) communications have recently attracted research efforts worldwide. Nevertheless, the main drawback of hybrid FSO/RF systems is the restricted bandwidth of the RF connection, especially when the FSO one is blocked by cloud coverage. This chapter explores a novel solution for the hybrid FSO/RF HAP-based SAGIN under the impact of weather and atmospheric conditions. Specifically, an additional unmanned aerial vehicle (UAV) is deployed to diversify the FSO link from the HAP-to-ground station to avoid cloud blockage while maintaining a high-speed connection of the FSO link. A mirror array constructed by re-configurable intelligent surface (RIS), an emerging technology, is mounted on the UAV to reflect the signals from the HAP. The channel model of RIS-UAV takes into account both atmospheric turbulence and hovering-induced pointing errors. Furthermore, we present a novel link switching design with a multi-rate

---

<sup>5</sup>The content of this Chapter was presented in part in

1. Thang V. Nguyen *et. al.*, “On the Design of RIS-UAV Relay-Assisted Satellite-Aerial-Ground Integrated Network,” *In Revision*.

adaptation scheme for the proposed network under different weather and turbulence conditions. Numerical results quantitatively confirm the effectiveness of our proposal. Additionally, we provide insightful discussions that can be helpful for the practical system design of RIS-UAV-assisted HAP-based SAGIN using hybrid FSO/RF links. Monte Carlo simulations are also performed to validate the accuracy of theoretical derivations.

## 4.1. Introduction

Recently, with the advance of the Internet of Things (IoTs), relying solely on the traditional terrestrial networks can no longer meet the exploding requirements of high-speed and reliable network access at any time and anywhere on the earth, in consideration of its limited coverage and network capacity. This has aroused widespread concern in the academia and industry on the air-ground coordination [88]. Thanks to the popularity of low Earth orbit (LEO) satellites, the satellite-aerial-ground integrated network (SAGIN) has been widely envisioned as a promising network architecture for future sixth-generation (6G) wireless communications [89].

In the SAGIN, high-altitude platform (HAP)-based relaying and free-space optical (FSO) communications are expected as the key technologies for extending the area coverage and the provision of extremely high-speed connectivities, respectively. The HAPs, which can be airships and balloons, operate at altitudes of 17-25 km, where the impact of weather is negligible. With the benefits of flexible deployment, cost-effectiveness, easy maintenance, and expansive coverage, HAPs have been widely considered as relaying nodes to enhance the scalability of satellite systems [90]. On the other hand, FSO communication has established a reputation for itself as capable of delivering extremely high-speed data services over long distances without exhausting radio frequency (RF) resources [3]. HAP-based SAGIN using FSO communications can be considered for a wide range of applications, e.g., Internet of vehicles, post-disaster emergency communications, and vertical backhaul solutions.

While the FSO link can be reliably maintained for the first hop of satellite-to-HAP,



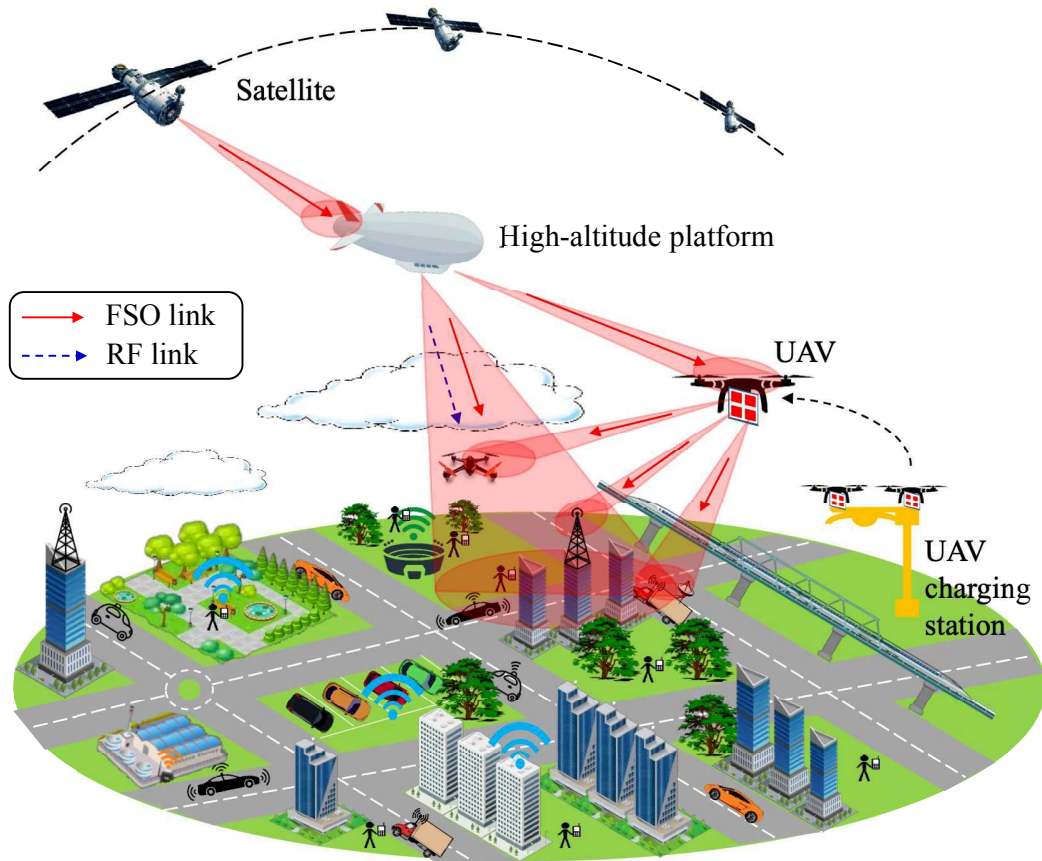


Figure 4.1: The proposal of HAP-based SAGIN using hybrid FSO/RF with temporarily optical RIS-UAV relay solution.

it is challenging for the FSO connection on the second hop of HAP-to-ground station under the impact of weather and atmospheric conditions. The primary concerns of such links are the cloud coverage and atmospheric turbulence, which pose various challenges to the design and performance of the SAGIN. To tackle this issue, an efficient solution is to use the hybrid FSO/RF scheme for the second hop of the HAP-to-ground station, where the RF link serves as a backup link in case of FSO link failure [115]. This is because the RF link is less subject to atmospheric turbulence and clouds. For example, the impact of atmospheric turbulence and heavy rain on the corresponding FSO and RF links is drastically, but these factors rarely happen simultaneously. As a result, two links can function in a complementary manner.

### 4.1.1. Related Work and Motivation

Driven by the potential of the hybrid FSO/RF scheme, its implementation has been extensively studied in terrestrial networks [115] and recently extended to the HAP-based SAGIN [63–67]. Particularly, Swaminathan *et. al.* analyzed the performance of downlink SAGIN using HAP-based relay station with hybrid FSO/RF links [63]. The authors in [64] investigated the performance of hybrid FSO/RF uplink for the HAP-based SAGIN, assuming Gamma-Gamma fading turbulence with pointing errors for the FSO link and shadowed-Rician fading for the RF link. In [65], the authors analyzed the performance of dual-hop SAGIN-based hybrid FSO/RF systems, both uplink and downlink, using an adaptive combining-based switching scheme. A novel HAP-assisted downlink SAGIN using hybrid FSO/RF communications was introduced in [66], in which the best HAP node was selected among multiple HAP nodes for relaying signals from the satellite. Different from [63–66], where decode-and-forward (DF) relaying scheme with constant data-rate transmissions were considered, the authors presented the design of rate adaptation hybrid FSO/RF links for HAP-based SAGIN using amplify-and-forward (AF) relaying scheme [67].

The major drawbacks of HAP-based SAGIN using the hybrid FSO/RF scheme are, nonetheless, the lower data rate, even with the new millimeter-wave (MMW) frequency bands, compared to that of FSO and the additional latency due to the optical/electrical and electrical/optical conversions. This fact is clearly indicated in the presence of cloud coverage, where the FSO link may be blocked, and the backup RF link is used more frequently [67]. An attractive solution for such a network scenario is to quickly deploy an additional unmanned aerial vehicle (UAV) as a relay node to diversify the FSO-based HAP-to-ground link in case of cloud blockage. Furthermore, a re-configurable intelligent surface (RIS) array [116], an emerging technology, can be carried by the UAV to reflect the incoming light from HAP and ensure that the transmitted light points to the ground station.

The combination of UAV and RIS offers an attractive solution for HAP-based SAGIN using hybrid FSO/RF in the presence of cloud coverage. Besides the flexible deploy-

ment, it requires less complex additional hardware than conventional relay nodes (i.e., using AF or DF at the UAV). Figure 5.2 illustrates the HAP-based SAGIN using FSO/RF over clouds, where the RIS-UAV is temporarily deployed to a position with negligible (or without) cloud coverage. It is worth mentioning that the relevant studies are still in the early stage, where few works on FSO-based RIS-UAV relays have been recently reported in [69–71]. In these studies, the UAV carrying RIS array serves as a relay station for FSO-based terrestrial networks between two buildings in the presence of a blockage. To our best knowledge, the studies considering RIS-assisted UAV relay in the SAGIN, and HAP-based SAGIN using hybrid FSO/RF in this particular case, have not been available in the literature. For such network scenarios, a proper design of a link-switching scheme, especially with rate adaptation for different links, is a critical issue under different weather and atmospheric conditions. This plays an essential role in practical system deployment. As a result, it is of importance and necessity to provide a comprehensive design framework for HAP-based SAGIN using hybrid FSO/RF incorporating the FSO-based RIS-UAV relay in the presence of cloud coverage.

### 4.1.2. Major Contributions and Novelty

This chapter offers a complete design and insightful analysis of FSO-based RIS-UAV relay-assisted SAGIN under the impact of different weather and atmospheric conditions. The key contributions of this chapter are summarized as follows.

*C<sub>1</sub>: It is a proposal of quick deployment of the UAV carrying RIS array as a relay station for HAP-based SAGIN using hybrid FSO/RF in the presence of clouds.*

In the HAP-based SAGIN, the primary FSO connection from HAP to ground station may be blocked by clouds containing high cloud liquid water content (CLWC) value [25]. In this case, instead of using a lower-rate backup RF link, the RIS-UAV is deployed to a position with negligible (or without) cloud coverage to diversify the FSO-based HAP-to-ground link. For this situation, the determination of time for deploying RIS-UAV is especially important as it is related to the tradeoff of achievable

data rate and energy consumption of the UAV. This can be determined based on the predefined CLWC value. This practical issue, nonetheless, has not been addressed in the literature on FSO-based RIS-UAV, e.g., [69–71].

*C<sub>2</sub>: We propose a multi-rate system design of HAP-based SAGIN incorporating the FSO-based RIS-UAV relay, where a new link-switching scheme is presented.*

In our proposal, the AF scheme is employed at HAP thanks to its cost-effectiveness and simple hardware requirements. In addition, the adaptive multi-rate transmission is considered for different links to reduce the frequent link switching. Different from the design in [67], a new link-switching scheme, considering the SAGIN with primary FSO-hybrid FSO/RF links and temporary FSO-based RIS-UAV link, is introduced, which is based on the specific condition of atmospheric turbulence and cloud.

*C<sub>3</sub>: From the proposed system design, we develop a comprehensive analytical framework that allows obtaining the system performance metrics, including outage probability, average transmission rate, and spectral efficiency.*

For the HAP-based SAGIN using hybrid FSO/RF links, the FSO channel is modeled, taking into account the atmospheric turbulence described by the Gamma-Gamma distribution, weather effect with cloud attenuation, and beam spreading loss. Additionally, the Rician fading model is considered for the RF channel. Regarding the FSO-based RIS-UAV links, derive the statistical model that considers the combined effects of atmospheric turbulence-induced fading and the RIS-UAV hovering-induced pointing error. More importantly, capitalizing on the obtained probability density functions (PDFs), we derive the performance metrics in the closed-form expressions.

*C<sub>4</sub>: We provide insightful numerical results into the detailed impacts of weather conditions on the performance of the proposed network scenario. Furthermore, a design guideline is also provided, which can be helpful for the practical design of UAV-assisted SAGIN using hybrid FSO/RF schemes.*

Monte Carlo simulations are performed to validate the correctness of the analytical model. In addition, we also highlight the effectiveness of our proposal by comparing the existing state-of-the-art systems.

It is noteworthy that an essential novelty of the work is the complete solution for HAP-based SAGIN that we set up by jointly considering the hybrid FSO/RF techniques together with a temporarily optical RIS-UAV-based relay, and a new link-switching scheme between them to counteract the impact of cloud and atmospheric conditions. The remainder of the Chapter is organized as follows. The proposed system, link switching scheme, and rate adaptation design are described in Section 4.2. Section 4.3 presents the channel models for transmission links. Different performance metrics, including outage probability, average transmission rate, and spectral efficiency are analytically derived in Section 4.4. Simulation results are given in Section 4.5. Finally, we conclude the chapter in Section 4.6.

## 4.2. System Description

In this section, we first describe the hybrid FSO/RF-based satellite-HAP-ground station (GS) system. Then, a proposal of FSO-based RIS-UAV relay for our considered system in case of cloud blockage is introduced. Finally, we present the design of link switching and rate adaptation schemes for our proposed system.

### 4.2.1. Hybrid FSO/RF-based Satellite-HAP-GS System

Figure 4.2 illustrates the hybrid FSO/RF-based, HAP-assisted satellite-to-GS system. In our considered system, the HAP is a relay node for the satellite-to-GS link, which employs the fixed-gain amplify-and-forward (AF) scheme. The FSO transmission is used for the link from the satellite to HAP. In addition, the hybrid FSO/RF one, using a switching scheme, is employed for the HAP-to-GS link, where FSO and RF are considered as the primary and backup links, respectively.

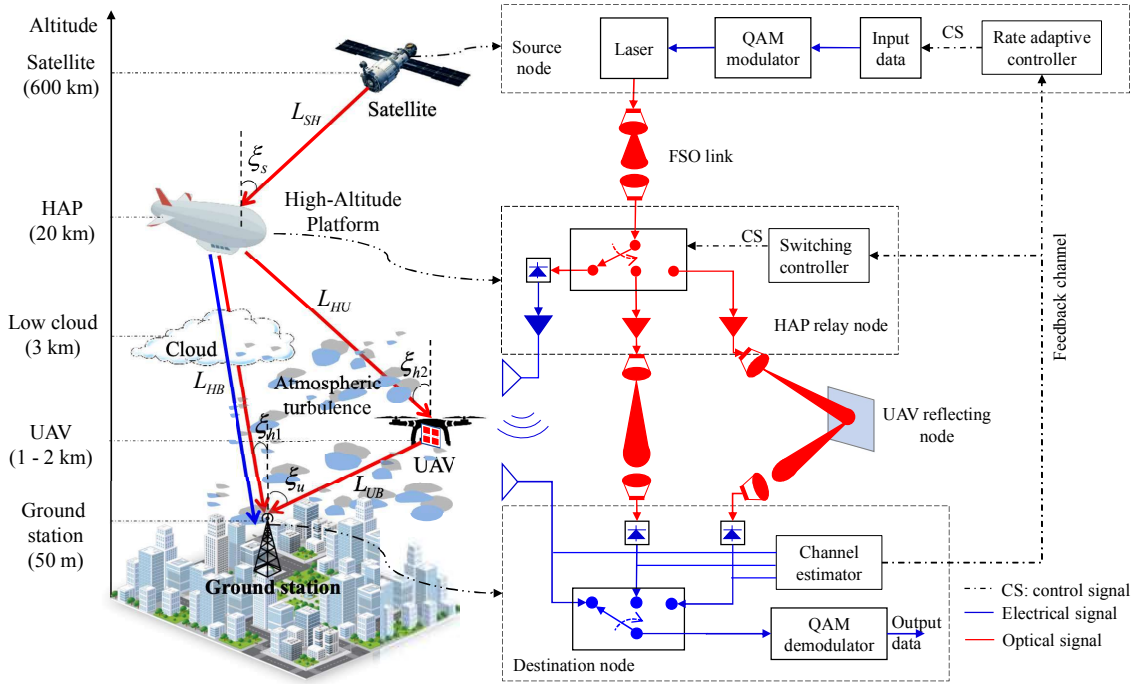


Figure 4.2: Integrated space-aerial-terrestrial hybrid FSO/RF system block diagram.

At the satellite, the modulated signal using a quadrature amplitude modulation (QAM) modulation is expressed as

$$s_n(t) = A_{nI}g(t) \cos(2\pi f_c t) - A_{nQ}g(t) \sin(2\pi f_c t), \quad (4.1)$$

where  $g(t)$  is the pulse shaping function,  $f_c$  is the QAM sub-carrier frequency, while  $A_{nI} = \{2n - 1 - I\}_{n=1}^I$  and  $A_{nQ} = \{2n - 1 - Q\}_{n=1}^Q$  are the in-phase and quadrature components of amplitude, respectively. The QAM signal is then used to modulate the laser intensity; as a result, the transmitted optical signal can be expressed as

$$s(t) = P_t[1 + m s_n(t)], \quad (4.2)$$

where  $P_t$  is the satellite's transmitted power,  $m$  is the modulation index, and  $s_n(t)$  is given in (4.1).

At the HAP relay, the received optical signal is amplified and forwarded to the GS. Here, hybrid FSO/RF transmission is considered for forwarding the signals, by which either the primary link of FSO or backup link of RF is selected based on the channel

state information (CSI) feedback from GS. Particularly, if the primary FSO link is chosen, the received optical signal from the satellite is amplified with a fixed-gain  $G_{\text{FSO}}$  so that the output at the HAP is given as

$$r_{\text{H}}^f(t) = G_{\text{FSO}}[h_{\text{SH}}s(t) + n_1^f], \quad (4.3)$$

where  $h_{\text{SH}}$  is the channel coefficient of the FSO-based satellite-to-HAP link,  $s(t)$  is given in (4.2), and  $n_1^f$  is the additive white Gaussian noise (AWGN) with variance  $\sigma_{n_1^f}^2$ . Besides, if the backup RF link is activated, the received optical signal is first converted to the electrical by a photodetector followed by a fixed-gain ( $G_{\text{RF}}$ ) amplifier. The output RF signal is thus expressed as

$$r_{\text{H}}^r(t) = G_{\text{RF}}[\eta h_{\text{SH}}P_t m s_n(t) + n_1^r], \quad (4.4)$$

where  $\eta$  is the electrical-to-optical conversion coefficient,  $n_1^r$  is the additive white Gaussian noise (AWGN) with variance  $\sigma_{n_1^r}^2$ , and  $s_n(t)$  is given in (4.1).

*At the GS destination*, if the FSO transmission is selected for HAP-to-GS link, the received signal at GS is given as

$$y_{\text{D}}^f = h_{\text{HG}}^f \eta h_{\text{SH}} G_{\text{FSO}} P_t m s_n(t) + h_{\text{HG}}^f \eta G_{\text{FSO}} n_1^f + n_2^f, \quad (4.5)$$

where  $h_{\text{HG}}^f$  is the FSO fading channel coefficient, and  $n_2^f$  is the AWGN with the variance  $\sigma_{n_2^f}^2$ . In addition, if the RF is used for HAP-to-GS link, the received signal at GS is written as

$$y_{\text{D}}^r = h_{\text{HG}}^r G_{\text{RF}} \eta h_{\text{SH}} P_t m s_n(t) + h_{\text{HG}}^r G_{\text{RF}} n_1^r + n_2^r, \quad (4.6)$$

where  $h_{\text{HG}}^r$  is the RF fading channel coefficient, and  $n_2^r$  is the AWGN with the variance  $\sigma_{n_2^r}^2$ .

From (4.5) and (4.6), the instantaneous received signal-to-noise ratios (SNRs) at GS,

denoted as  $\gamma_{e2e}^f$  for FSO-FSO link and  $\gamma_{e2e}^r$  for FSO-RF link, are expressed as

$$\gamma_{e2e}^f = \frac{\left(h_{\text{HG}}^f \eta h_{\text{SH}} G_{\text{FSO}} P_t m\right)^2}{\left(h_{\text{HG}}^f \eta G_{\text{FSO}} \sigma_{n_1^f}\right)^2 + \sigma_{n_2^f}^2} = \frac{\gamma_{\text{SH}}^f \gamma_{\text{HG}}^f}{\gamma_{\text{HG}}^f + 1}, \quad (4.7)$$

$$\gamma_{e2e}^r = \frac{\left(h_{\text{HG}}^r G_{\text{RF}} \eta h_{\text{SH}} P_t m\right)^2}{\left(h_{\text{HG}}^r \eta G_{\text{RF}} \sigma_{n_1^r}\right)^2 + \sigma_{n_2^r}^2} = \frac{\gamma_{\text{SH}}^f \gamma_{\text{HG}}^r}{\gamma_{\text{HG}}^r + 1}, \quad (4.8)$$

where  $\gamma_{\text{SH}}^f = (h_{\text{SH}} P_t m)^2 / \sigma_{n_1^f}^2$  and  $\gamma_{\text{HG}}^f = (\eta h_{\text{HG}}^f)^2 / \sigma_{n_2^f}^2$  are respectively the instantaneous SNRs of satellite-to-HAP and HAP-to-GS FSO links, while  $\gamma_{\text{RF}} = (\eta h_{\text{HG}}^r)^2 / \sigma_{n_2^r}^2$  is the instantaneous SNR of RF-based HAP-to-GS link. Additionally, we assume that the fixed-gain  $G_{\text{FSO}}$  can completely compensate the noise, where we can set  $G_{\text{FSO}}^2 = 1 / \sigma_{n_1^f}^2$  [117].

#### 4.2.2. Proposal of FSO-based RIS-UAV Relay

As reported in [25], the cloud coverage, especially with high cloud liquid water content (CLWC) values, may completely block the FSO-based HAP-to-GS link. To maintain the high-speed connection of the FSO link, a UAV equipped with a re-configurable intelligent surface (RIS) array is deployed to the positions with negligible (or without) cloud coverage. The UAV relay can diverse the FSO-based HAP-to-GS link, as depicted in Fig. 4.2. The RIS module mounted on the UAV serves as a reflector, which can reflect and forward the optical signals from HAP to GS [118]. It is worth noting that the position for UAV's deployment is based on the cloud forecast map and the actual monitoring data. Besides, the RIS-UAV relay is deployed when the CLWC value reaches a predefined CLWC threshold,  $M_c^{\text{th}}$ , which is determined by a targeted outage level of the FSO-based direct link from HAP to GS.

From the optical output signal at HAP given in (4.3), the received signal at GS, which is reflected and forwarded by RIS-UAV relay, can be expressed by

$$y_D^u = h_{\text{HG}}^u \eta G_{\text{FSO}} [h_{\text{SH}} P_t m s_n(t) + n_1^u] + n_2^u, \quad (4.9)$$



where  $h_{\text{HG}}^u$  is the composite fading channel coefficient of HAP-UAV-GS FSO link.  $n_1^u$  and  $n_2^u$  are the AWGN with the variance  $\sigma_{n_1^u}^2$  and  $\sigma_{n_2^u}^2$ , respectively. From (4.9), the instantaneous received SNR at GS in the case of RIS-UAV relay, denoted by  $\gamma_{e2e}^u$ , is given as

$$\gamma_{e2e}^u = \frac{(h_{\text{HG}}^u \eta G_{\text{FSO}} P_t m)^2}{(h_{\text{HG}}^u \eta G_{\text{FSO}} \sigma_{n_1^u})^2 + \sigma_{n_2^u}^2} = \frac{\gamma_{\text{SH}}^f \gamma_{\text{HG}}^u}{\gamma_{\text{HG}}^u + 1}, \quad (4.10)$$

where  $\gamma_{\text{SH}}^f = (h_{\text{SH}} P_t m)^2 / \sigma_{n_1^u}^2$  and  $\gamma_{\text{HG}}^u = (\eta h_{\text{HG}}^u)^2 / \sigma_{n_2^u}^2$  are the instantaneous SNRs of satellite-to-HAP and HAP-UAV-GS FSO links, respectively.

### 4.2.3. Link Switching and Multi-Rate Adaptation Design

#### 4.2.3.1. Link Switching Scheme

The proposal of a link switching scheme for our considered systems is illustrated in Table 4.1 with three transmission strategies. In particular, we consider the FSO-based satellite HAP-GS link, which employs FSO transmissions for both hops, is considered the primary one.

Table 4.1: The proposal of link switching scheme.

Priority Order	Transmission Link	Abbreviation	Description
1	Strategy 1: FSO-based Satellite-HAP- GS	FSO-FSO1	Primary link
2	Strategy 2: FSO-based Satellite-HAP- UAV-GS	FSO-FSO2	Use when high CLWC values on the primary link
3	Strategy 3: RF-based Satellite-HAP- GS	FSO-RF	Use when first two strategies are not available

When the clouds block the primary link of FSO-based HAP-to-GS, the system switches to transmission strategy 2, in which the FSO link from HAP to GS is reflected and

forwarded by the RIS-UAV relay. Suppose the first two transmission strategies are not available. In that case, e.g., cloud blockage on the primary link and strong turbulence on the RIS-UAV relay link, the 3rd transmission strategy is considered, where RF transmission is used for the direct link between HAP and GS. It is worth noting that the priority order considered in Table 4.1 is applicable in case of cloud blockage on the primary link, which is the main focus of the chapter. For example, in other scenarios, the outage occurs on the primary link due to the strong turbulence; the RF transmission is preferable to the RIS-UAV relay solution.

Table 4.2: An example of multi-rate adaptation design for different transmission links.

Mode	Outage		Backup link (FSO-RF): Active		Backup link (FSO-FSO2): Active		Primary link (FSO-FSO1): Active	
	1	2	1	2	1	2	1	2
Modulation	BPSK	QPSK	BPSK	QPSK	8-QAM	8-QAM	BPSK	QPSK
Data rate	$R_s^r$	$2R_s^r$	$R_s^u$	$2R_s^u$	$3R_s^u$	$3R_s^u$	$R_s^f$	$2R_s^f$
FSO-FSO1	$\gamma_{e2e}^f < \gamma_{th1}^f$		CLWC $\geq M_c^{th}$ and $\gamma_{e2e}^f < \gamma_{th1}^f$				$[\gamma_{th1}^f, \gamma_{th2}^f)$	$[\gamma_{th2}^f, \gamma_{th3}^f)$
FSO-FSO2	$\gamma_{e2e}^u < \gamma_{th1}^u$		$[\gamma_{th1}^u, \gamma_{th2}^u)$	$[\gamma_{th2}^u, \gamma_{th3}^u)$	$\gamma_{e2e}^u \geq \gamma_{th3}^u$			$\gamma_{e2e}^f \geq \gamma_{th3}^f$
FSO-RF	$\gamma_{e2e}^r < \gamma_{th1}^r$	$\gamma_{e2e}^r \geq \gamma_{th2}^r$						

### 4.2.3.2. Multi-Rate Adaptation Design

The objective of the multi-rate adaptation scheme is to maximize the data rate over turbulence fading channels while satisfying a pre-defined Quality of Service (QoS), i.e., a targeted bit error rate ( $\text{BER}_0$ ). For each transmission link, we adopt the subcarrier  $M$ -array QAM schemes as in [17] with a fixed symbol rate of  $R_s^*$  for  $N$  possible transmission modes. The transmission bit rate changes for every mode given as  $R_b^* = R_s^* \log_2(M)$ , where  $M$  is the constellation size. Let  $\gamma_{\text{th}_1}^* < \gamma_{\text{th}_2}^* < \dots < \gamma_{\text{th}_N}^*$  be the switching thresholds for different transmission modes, and  $\gamma_{e2e}^*$  be the instantaneous end-to-end SNR for the considered transmission link. The transmission mode  $i$ -th is chosen if  $\gamma_{\text{th}_i}^* \leq \gamma_{e2e}^* < \gamma_{\text{th}_{i+1}}^*$ , where  $i \in \{1, 2, \dots, N-1\}$ ; to avoid a high error rate, no transmission is allowed when  $\gamma_{e2e}^* < \gamma_{\text{th}_1}^*$ . These thresholds are obtained based on the fact that the average BER for each transmission mode satisfies the targeted  $\text{BER}_0$  as in [68]. In our study, the feedback channel carrying CSI information is supposed to be reliable, where a strong error correction code can be used [119]. Besides, the temporal coherence times of considered FSO and RF links (order of tens of milliseconds) are relatively long compared with the time slot duration, including the data transmission and feedback time (order of several milliseconds) [67]. Due to the slowly time-varying nature of fading channels, CSIs are still up-to-date information when arriving at the HAP and satellite.

For the sake of explicit clarity, the aforementioned parameters used for FSO-FSO1 link is  $\{M_1, R_s^f, N_1, R_b^f, \gamma_{\text{th}_i}^f, \gamma_{e2e}^f\}$ , for FSO-FSO2 link is  $\{M_2, R_s^u, N_2, R_b^u, \gamma_{\text{th}_i}^u, \gamma_{e2e}^u\}$ , and for FSO-RF link is  $\{M_3, R_s^r, N_3, R_b^r, \gamma_{\text{th}_i}^r, \gamma_{e2e}^r\}$ . An example of multi-rate adaptation design for different transmission links is illustrated in Table 4.2, in which  $N_1 = N_2 = 3$  transmission modes for FSO-FSO1 and FSO-FSO2 links, while  $N_3 = 2$  transmission modes for the FSO-RF link.

### 4.3. Channel Modeling

This section presents the considered channel models for each transmission hop, including FSO-based satellite-to-HAP, hybrid FSO/RF-based HAP-to-GS, and FSO-based HAP-UAV-GS.

#### 4.3.1. FSO-based Satellite-to-HAP Link

As for the FSO-based satellite-to-HAP link, the effect of atmospheric turbulence is generally small, which can be ignored as the laser beam goes through a non-atmospheric path (above 20 km compared to the ground level) [120]. In this chapter, we assume that HAP remains stable at its fixed position, and a fine-tracking system [121] with perfect alignment is deployed. It is, therefore, supposed that the beam spreading loss is a major impairment for this link. Besides, as reported in [18], the maximum frequency shift between an LEO satellite and a stable HAP is the order of several GHz. These values are, nonetheless, within the capability of the current receiver design for LEO satellite-based FSO systems (i.e., can deal with frequency shift up to more than 10 GHz [18]). As a result, we ignore the Doppler effect in the performance analysis.

Considering the Gaussian beam profile, the fraction of collected power at HAP's circular detector with an aperture radius  $D_{\text{HAP}}$  is approximated as [120]

$$h_{\text{SH}} \approx A_0 \exp\left(-\frac{2\rho^2}{w_{L,e(\text{eq})}^2}\right), \quad (4.11)$$

where  $A_0 = [\text{erf}(v)]^2$  is the fraction of the collected power at  $\rho = 0$  with  $v = \frac{D_{\text{HAP}}\sqrt{\pi}}{w_L\sqrt{2}}$  corresponding to the ratio of the aperture radius and beam-width, and  $w_L = w_0\sqrt{1 + \epsilon\left(\frac{\lambda L_{\text{SH}}}{\pi w_0^2}\right)^2}$  is the beam-waist at the distance  $L_{\text{SH}}$ , which is given by  $L_{\text{SH}} = (H_{\text{SAT}} - H_{\text{HAP}})/\cos(\xi_{\text{SAT}})$ , in which  $H_{\text{SAT}}$  is the altitude of the satellite,  $H_{\text{HAP}}$  is the altitude of the HAP, and  $\xi_{\text{SAT}}$  is the zenith angle of the satellite,  $w_0 = (2\lambda)/(\pi\theta_{\text{SAT}})$  is the beam-waist at  $L_{\text{SH}} = 0$  with  $\theta_{\text{SAT}}$  is the diver-

gence angle of the satellite,  $\epsilon = \left(1 + 2\frac{w_0^2}{\rho_0^2 L_{\text{SH}}}\right)$ , and  $\rho(L_{\text{SH}}) = (0.55C_n^2 k_w^2 L_{\text{SH}})^{-3/5}$  is the coherence length [101]. Besides, the equivalent beam-waist is determined as  $w_{L,\text{e(eq)}}^2 = w_L^2 \frac{\sqrt{\pi}\text{erf}(v)}{2v\exp(-v^2)}$ .

### 4.3.2. Hybrid FSO/RF-based HAP-to-GS Link

#### 4.3.2.1. RF Channel

For RF channel, we consider the major impairments, including path loss, cloud attenuation, and fading phenomenon. The channel coefficient of RF link can be expressed as  $h_{\text{HG}}^r = g_r h_r$ , where  $h_r$  is the channel fading coefficient, while  $g_1$  is the path-loss of the RF link, which can be expressed as [64]

$$g_r(\text{dB}) = G_{\text{T}} + G_{\text{R}} - \mathcal{L}_{\text{F}} - \mathcal{L}_{\text{A}} - \mathcal{L}_{\text{c}}, \quad (4.12)$$

where  $G_{\text{T}}$  and  $G_{\text{R}}$  are the transmitted and received antenna gains (in dB), respectively.  $\mathcal{L}_{\text{A}}$  (dB) is the gaseous atmospheric loss.  $\mathcal{L}_{\text{F}}(\text{dB}) = 92.45 + 20\log f_c + 20\log L_{\text{HG}}$  is the free space loss for HAP-to-GS RF link, in which  $f_c$  (GHz) is the frequency for RF link, and  $L_{\text{HG}} = (H_{\text{HAP}} - H_{\text{GS}})/\cos(\xi_{\text{HG}})$  is the transmission distance from HAP to the ground station with HAP's zenith angle  $\xi_{\text{HG}}$  and  $H_{\text{GS}}$  is the height of the ground station.

*Regarding the cloud attenuation*, as recommended by ITU-P840 [102], Rayleigh scattering model is suitable for modeling the attenuation with frequencies up to 200 GHz, in which the attenuation on RF link due to cloud can be given as [102]

$$\mathcal{L}_{\text{c}} = \frac{d_{\text{c}}^r \alpha_r}{\cos(\xi_{\text{HG}})}, \quad (4.13)$$

where  $d_{\text{c}}^r$  is the vertical extent of cloud,  $\xi_{\text{HG}}$  is the HAP's zenith angle for HAP-GS beam, and  $\alpha_r = K_{\text{c}} M_{\text{c}}$  is the specific attenuation within clouds in which  $K_{\text{c}}$  ((dB/km)/(g/m<sup>3</sup>)) is the specific attenuation coefficient,  $M_{\text{c}}$  (g/m<sup>3</sup>) is the cloud liquid water content (CLWC) [102].

As for fading channel, due to the line-of-sight (LOS) of vertical link from HAP to GS, the small-scale fading is widely described by the Rician distribution [103]. Therefore, the probability density function (PDF) and cumulative density function (CDF) of the instantaneous received SNR can be given as [103]

$$f_{\gamma_{\text{HG}}^r}(\gamma_{\text{HG}}^r) = \frac{K+1}{\bar{\gamma}_{\text{HG}}^r} I_0 \left( 2\sqrt{\frac{K(K+1)\gamma_{\text{HG}}^r}{\bar{\gamma}_{\text{HG}}^r}} \right) \times \exp \left[ -\frac{(K+1)\gamma_{\text{HG}}^r}{\bar{\gamma}_{\text{HG}}^r} - K \right], \quad (4.14)$$

$$F_{\gamma_{\text{HG}}^r}(\gamma_{\text{HG}}^r) = 1 - Q_1 \left( \sqrt{2K}, \sqrt{\frac{2(K+1)\gamma_{\text{HG}}^r}{\bar{\gamma}_{\text{HG}}^r}} \right), \quad (4.15)$$

where  $Q_1(\cdot, \cdot)$  is the Marcum  $Q_1$ -function,  $K$  is the Rician factor, and  $\bar{\gamma}_{e2e}^r$  is the average SNR of the FSO-RF link. From (4.8) and (4.15), the CDF of end-to-end FSO-RF link is given as

$$F_{\gamma_{e2e}^r}(\gamma) = \Pr \left( \frac{\gamma_{\text{SH}}^f \gamma_{\text{HG}}^r}{\gamma_{\text{HG}}^r + 1} < \gamma \right) = F_{\gamma_{\text{HG}}^r} \left( \frac{\gamma}{\gamma_{\text{SH}}^f - \gamma} \right). \quad (4.16)$$

#### 4.3.2.2. FSO Channel

We take into account the major impairments on the FSO-based HAP-to-GS link, including cloud attenuation  $h_c^f$ , atmospheric turbulence  $h_a^f$ , and beam spreading loss  $h_s^f$ . The composite channel coefficient, denoted by  $h_{\text{HG}}^f$ , hence, can be expressed by  $h_{\text{HG}}^f = h_c^f h_a^f h_s^f$ . We now describe these major impairments, as follows.

*Regarding the cloud attenuation*, the liquid water particles in clouds cause the scattering phenomenon of the FSO beam propagation, leading to a decrease of visibility and significant attenuation of received signal's power. Here, we consider low cloud types (1-3 km), e.g., Stratus and Cumulus, which is the most challenging for FSO

communications [25]. The attenuation due to clouds can be expressed as [68]

$$h_c^f = \exp(-\alpha_f d_c^f), \quad (4.17)$$

where  $\alpha_f$  is the attenuation coefficient, which is given as [67]

$$\alpha_f = \frac{3.91}{V[\text{km}]} \left( \frac{\lambda[\text{nm}]}{550} \right)^{-q}, \quad (4.18)$$

where  $V$  is the visibility, which is a function of the number cloud droplet concentration ( $N_c$ ) [25]. Additionally,  $q$  is the size distribution of the scattering particles, and by using the Kim model, it can be found in [57].

*As for the atmospheric turbulence*, this phenomenon causes the scintillation effect leading to the signal power fluctuations at the GS. As reported in [57], Gamma-Gamma (GG) is one of the most suitable models for describing a wide range of turbulence conditions in FSO-based satellite communications. The PDF of  $h_a^f$  is given as [118]

$$f_{h_a^f}(h_a^f) = \frac{2(\alpha\beta)^{\frac{\alpha+\beta}{2}}}{\Gamma(\alpha)\Gamma(\beta)} (h_a^f)^{\frac{\alpha+\beta}{2}} K_{\alpha-\beta} \left( 2\sqrt{\alpha\beta h_a^f} \right), \quad (4.19)$$

where  $\Gamma(\cdot)$  is the gamma function, and  $K_v(\cdot)$  is the  $v$ -th order modified Bessel function of the second kind. Additionally,  $\alpha$  and  $\beta$  are respectively the effective number of large-scale and small-scale eddies of scattering environment found in [118] and are the functions of Rytov variance ( $\sigma_R^2$ ), which is given as

$$\sigma_R^2 = 2.25 k_w^{7/6} \text{sec}^{11/6} (\xi_{\text{HG}}) \int_{H_{\text{GS}}}^{H_{\text{HAP}}} C_n^2(h) (h - H_{\text{GS}})^{5/6} dh, \quad (4.20)$$

where  $k_w = 2\pi/\lambda$  is the optical wave number corresponding to the optical wavelength  $\lambda$ . Besides, the variation of refractive index structure parameter,  $C_n^2(h)$ , according to the altitude  $h$  can be described by the most widely used Hufnagel-Valley model and is given as [57], i.e.,  $C_n^2(h) = 0.00594 \left( \frac{v_{\text{wind}}}{27} \right)^2 (10^{-5}h) \exp\left(-\frac{h}{1000}\right) + 2.7 \times$



$10^{-16} \exp\left(-\frac{h}{1500}\right) + C_n^2(0) \exp\left(-\frac{h}{100}\right)$ , where  $C_n^2(0)$  is the ground turbulence level varying from  $10^{-17} \text{m}^{-2/3}$  to  $10^{-13} \text{m}^{-2/3}$ , and  $v_{wind}$  (m/s) is the root mean squared wind speed.

For the beam spreading loss, similar to (4.11), the fraction of the power collected by GS with aperture radius of  $D_{\text{HAP}}$  can be approximated as [120]

$$h_s^f \approx A_0^f \exp\left(-2 \left(\frac{\rho^f}{\omega_{L,e(\text{eq})}^f}\right)^2\right), \quad (4.21)$$

where  $\rho^f$  is the radial displacement between centers of HAP beam footprint and GS's detector,  $\omega_{L,e(\text{eq})}^f$  is the equivalent beam waist, and  $A_0^f = [\text{erf}(v^f)]^2$  with  $v^f = \sqrt{\pi} D_{\text{HAP}} / (\sqrt{2} \omega_{L,e}^f)$ . Additionally,  $\omega_{L,e}^f \approx \theta_{\text{HG}} L_{\text{HG}}$ , where  $\theta_{\text{HG}}$  is the divergence angle for the HAP-GS beam, and  $L_{\text{HG}}$  is the propagation distance from HAP to GS, i.e.,  $L_{\text{HG}} = (H_{\text{HAP}} - H_{\text{GS}}) \sec(\xi_{\text{HG}})$ .

Given  $h_{\text{HG}}^f = h_c^f h_a^f h_s^f$ , where  $h_c^f$ ,  $h_a^f$ , and  $h_s^f$  are found in respectively (4.17), (4.19), and (4.21), and by using a simple transformation, the CDF of instantaneous SNR for FSO-based HAP-to-GS link, denoted by  $\gamma_{\text{HG}}^f$ , can be expressed as

$$F_{\gamma_{\text{HG}}^f}(\gamma_{\text{HG}}^f) = \frac{1}{\Gamma(\alpha) \Gamma(\beta)} G_{1,3}^{2,1} \left[ \alpha \beta \sqrt{\frac{\gamma_{\text{HG}}^f}{\bar{\gamma}_{\text{HG}}^f}} \left| \begin{matrix} 1 \\ \alpha, \beta, 0 \end{matrix} \right. \right], \quad (4.22)$$

where  $\bar{\gamma}_{\text{HG}}^f$  is the average SNR for FSO-based HAP-to-GS link, and  $G_{p,q}^{m,n}(\cdot)$  is the MeijerG function. From (4.7) and (4.22), the CDF of end-to-end instantaneous SNR of the primary FSO-FSO1 link can be derived as

$$F_{\gamma_{e2e}^f}(\gamma) = \Pr\left(\frac{\gamma_{\text{SH}}^f \gamma_{\text{HG}}^f}{\gamma_{\text{HG}}^f + 1} < \gamma\right) = F_{\gamma_{\text{HG}}^f}\left(\frac{\gamma}{\gamma_{\text{SH}}^f - \gamma}\right). \quad (4.23)$$

#### 4.3.3. UAV-Assisted HAP-to-GS FSO Link

Figure 4.3(a) depicts the structure and perspective view of RIS-based liquid crystal (LC) materials for the UAV-assisted HAP-to-GS FSO link. In this chapter, for the

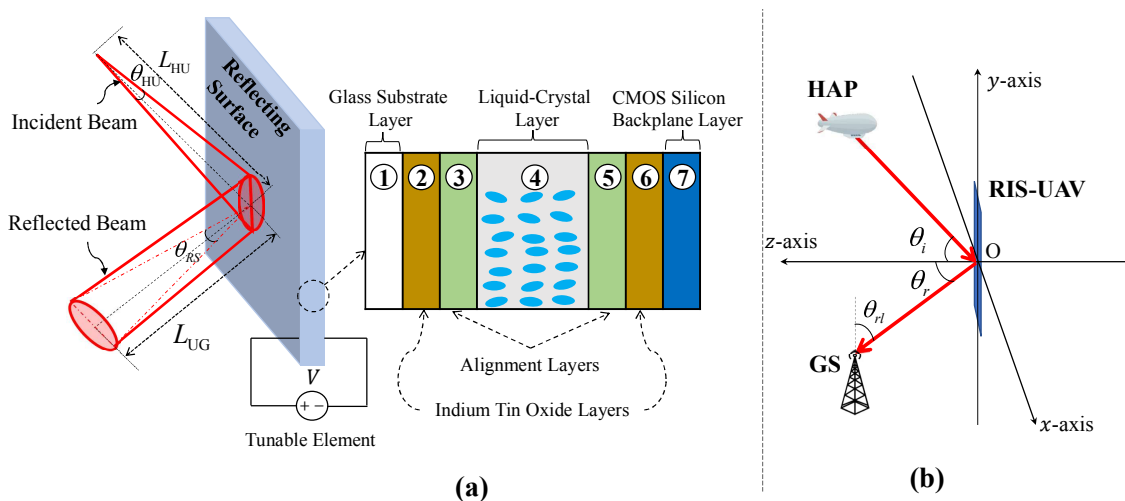


Figure 4.3: Beam reflect-and-forward by RIS mounted on UAV.

sake of simplicity, we adopt RIS-based LC structure<sup>6</sup> in [122] using a single element (large size) to illustrate our proposed network scenario. For this structure, there are seven layers of thin materials, including a glass substrate layer, two indium tin oxide (ITO) layers, two alignment layers, the LC material, and a CMOS silicon backplane layer.

Particularly, the incident beam, which faces refraction on the glass substrate, propagates through the RIS-layer structure. The glass substrate layer is also in charge of generating the director, which defines the final light orientation. Here, in a cell, LC's molecules tend to point toward a predefined direction called the director. In addition, the ITO is a thin conductive coating material realized with a fair trade-off between conductivity and transparency. Its primary role is to assist with heat generation and control of the LC cell. The alignment layers guide light arrays through the predefined direction in the LC cell. The CMOS silicon backplane, which represents the bottom layer as depicted in Figure 4.3(a), is made of a material with a high reflection coefficient. The RIS depth and crystal orientation can be adjusted by a tunable element so that the light reflected on the CMOS silicon backplane is oriented in the receiver's direction.

A schematic of the considered optical RIS-UAV-assisted HAP-to-GS links is illus-

<sup>6</sup>Interested readers can refer to [116] for other structures of optical RIS-based materials.

trated in Fig. 4.3(b), wherein the Cartesian coordinate system  $[x, y, z] \in \mathbb{R}^3$  is considered. Without loss of generality, we assume that the RIS array lies on the  $x - y$  plane and its center is at  $[0, 0, 0]$ , which is the intersection of the incident beam (from HAP) and reflected beam (at RIS). Here,  $\theta_i$  and  $\theta_r$  are the incident and reflected angles at the RIS array, respectively. Additionally,  $\theta_{rl}$  is the angle between the reflected beam and the normal vector of the lens at GS. In this chapter, we take into account the major impairments on the links, including (i) atmospheric attenuation  $h_1^u$ , (ii) RIS-UAV hovering-induced misalignment  $h_m^u$ , and (iii) atmospheric turbulence  $h_a^u$ . The composite channel fading coefficient is, then, formulated as  $h_{\text{HG}}^u = h_1^u h_m^u h_a^u$ . The attenuation  $h_1^u$ , which can be found in [19, (7)], is considered in clear sky conditions. *As for the RIS-UAV hovering-induced misalignment*, since the RIS-UAV relay receives a sufficiently large beam footprint from HAP, the beam truncation can be ignored. As a result, the position fluctuations of the RIS array within its plane, i.e., the  $x - y$  plane, can be neglected. In other words, only the fluctuations along the  $z$  axis, denoted by  $\epsilon_r^z \sim \mathcal{N}(0, \sigma_{\text{ris}}^2)$ , are considered. The misalignment due to the UAV hovering results in the misalignment between center of reflected beam footprint from the RIS-UAV relay and the center of the GS's detector, denoted by  $u$ . Using Fig. 4.3(b), if the UAV position fluctuation of  $\epsilon_r^z$ , the misalignment  $u$  at GS can be computed as  $u = \frac{1}{\cos \theta_{rl}} \frac{\sin(\theta_i + \theta_r)}{\cos \theta_i} \epsilon_r^z$ . As  $\epsilon_r^z \sim \mathcal{N}(0, \sigma_{\text{ris}}^2)$ , the misalignment also follows a zeros mean Gaussian distribution, i.e.,  $u \sim \mathcal{N}(0, \sigma_u^2)$  with the variance of  $\sigma_u^2 = \frac{1}{\cos^2 \theta_{rl}} \frac{\sin^2(\theta_i + \theta_r)}{\cos^2 \theta_i} \sigma_{\text{ris}}^2$ . On the other hand, as the Gaussian beam profile is considered, the fraction of collected power at the GS's detector with aperture radius of  $D_{\text{GS}}$  can be approximated as [70]

$$h_m^u \approx A_0^u \exp\left(-\frac{2u^2}{tw_L^2}\right), \quad (4.24)$$

where  $A_0^u = [\text{erf}(v)]^2$ ,  $t = \frac{\sqrt{\pi} \text{erf}(v)}{2v \exp(-v^2) \cos^2(\theta_{rl})}$ , and  $v = \frac{\sqrt{2} \cos(\theta_{rl}) D_{\text{GS}}}{w_L}$ . Besides,  $w_L = w_u \sqrt{\left(1 - \frac{L_{\text{UG}}}{F_0}\right)^2 + \left(\frac{\lambda L_{\text{UG}}}{\pi w_u^2}\right)^2}$  is the optical beam waist at the GS's detector. Here,  $F_0$  is the radius of curvature ( $F_0 = \infty$ , for a collimated Gaussian beam), and  $L_{\text{UG}}$  is the propagation distance from UAV to GS, i.e.,  $L_{\text{UG}} = (H_{\text{UAV}} - H_{\text{GS}}) \sec(\xi_{\text{UG}})$  with  $\xi_{\text{UG}}$

the UAV's zenith angle. Additionally,  $w_u = \frac{2\lambda}{\pi\theta_{\text{RIS}}}$  with  $\theta_{\text{RIS}} = \theta_{\text{HU}}(1 + L_{\text{HU}}/L_{\text{UG}})$ , where  $L_{\text{HU}} = (H_{\text{HAP}} - H_{\text{UAV}})\sec(\xi_{\text{HU}})$  with  $\xi_{\text{HU}}$  is the HAP's zenith angle for the HAP-UAV beam. It is worth noting that this chapter considers the power amplifying-RIS structure as depicted in Figure 4.3(a), in which the geometric loss at RIS array can be compensated as reported in [122].

From (4.24) and by assuming that  $u$  follows a zero mean Gaussian distribution, the PDF of  $h_m^u$  is given as [123]

$$f_{h_m^u}(h_m^u) = \frac{\sqrt{\varpi}}{A_0^u\sqrt{\pi}} \left[ \ln \left( \frac{A_0^u}{h_m^u} \right) \right]^{-\frac{1}{2}} \left( \frac{h_m^u}{A_0^u} \right)^{\varpi-1}, \quad (4.25)$$

where  $0 \leq h_m^u \leq A_0^u$  and  $\varpi = \frac{tw_u^2}{4\sigma_u^2}$ .

Regarding the atmospheric turbulence, it can be expressed as  $h_a^u = h_{a_1}^u h_{a_2}^u$ , in which the PDF of  $h_{a_z}^u$ ,  $z \in \{1, 2\}$  can be modeled by the GG distribution as

$$f_{h_{a_z}^u}(h_{a_z}^u) = \frac{2(\alpha_z\beta_z)^{\frac{\alpha_z+\beta_z}{2}}}{\Gamma(\alpha_z)\Gamma(\beta_z)} (h_{a_z}^u)^{\frac{\alpha_z+\beta_z-1}{2}} K_{\alpha_z-\beta_z} \left( 2\sqrt{\alpha_z\beta_z h_{a_z}^u} \right), \quad (4.26)$$

where  $\alpha_z$  and  $\beta_z$  are respectively the effective number of large-scale and small-scale eddies of scattering environment. From (4.26), the PDF of  $h_a^u$  can be expressed as  $f_{h_a^u}(h_a^u) = \int f_{h_{a_1}^u|h_{a_2}^u}(h_{a_1}^u|h_{a_2}^u) f_{h_{a_2}^u}(h_{a_2}^u) dh_{a_2}^u$ . With the help of [124, (9.31.2), (8.4.23.1)], [109, (8.4.23.1)], and [110, (21)], along with some mathematical manipulations, the PDF of  $h_a^u$  can be derived as

$$f_{h_a^u}(h_a^u) = \frac{1}{\Gamma(\alpha_1)\Gamma(\beta_1)\Gamma(\alpha_2)\Gamma(\beta_2)h_a^u} \times G_{0,4}^{4,0} \left[ \alpha_1\beta_1\alpha_2\beta_2h_a^u \middle| \alpha_1 \quad \beta_1 \quad \alpha_2 \quad \beta_2 \right]. \quad (4.27)$$

*Composite Channel Statistical Model:* The PDF of composite channel coefficient, i.e.,

$h_{\text{HG}}^u = h_1^u h_m^u h_a^u$ , is given as

$$\begin{aligned}
 f_{h_{\text{HG}}^u}(h_{\text{HG}}^u) &= \int_0^\infty \frac{1}{h_a^u h_1^u} f_{h_m^u}\left(\frac{h_{\text{HG}}^u}{h_a^u}\right) f_{h_a^u}(h_a^u) dh_a^u, \\
 &= \frac{\sqrt{\varpi}}{A_0^u h_1^u \sqrt{\pi} \Gamma(\alpha_1) \Gamma(\beta_1) \Gamma(\alpha_2) \Gamma(\beta_2)} \\
 &\quad \times \int_{\frac{h_{\text{HG}}^u}{A_0^u h_1^u}}^\infty \frac{1}{(h_a^u)^2} \frac{1}{\sqrt{\ln\left(\frac{A_0^u h_1^u h_a^u}{h_{\text{HG}}^u}\right)}} \left(\frac{h_{\text{HG}}^u}{A_0^u h_1^u h_a^u}\right)^{\varpi-1} \\
 &\quad \times G_{0,4}^{4,0} \left[ \alpha_1 \beta_1 \alpha_2 \beta_1 h_a^u \middle| \begin{matrix} \alpha_1 & \beta_1 & \alpha_2 & \beta_2 \end{matrix} \right] dh_a^u. \tag{4.28}
 \end{aligned}$$

By using a transformation  $\delta = \sqrt{\ln\left(\frac{A_0^u h_1^u h_a^u}{h_{\text{HG}}^u}\right)}$ ,  $x^2 = \varpi \delta^2$  and applying the Gauss-Hermit quadrature integration [125, (25.4.46)] along with several mathematical manipulations, the closed-form of (4.28) can be obtained as

$$\begin{aligned}
 f_{h_{\text{HG}}^u}(h_{\text{HG}}^u) &= \sum_{i=1}^n \frac{2w_i}{\sqrt{\pi} \Gamma(\alpha_1) \Gamma(\beta_1) \Gamma(\alpha_2) \Gamma(\beta_2)} \left(\frac{1}{h_{\text{HG}}^u}\right) \\
 &\quad \times G_{0,4}^{4,0} \left[ \frac{\alpha_1 \beta_1 \alpha_2 \beta_2 h_{\text{HG}}^u}{A_0^u h_1^u} \exp\left(\frac{x_i^2}{\varpi}\right) \middle| \begin{matrix} \alpha_1 & \beta_1 & \alpha_2 & \beta_2 \end{matrix} \right], \tag{4.29}
 \end{aligned}$$

where  $w_i$  is the weighting factor and  $x_i$  is the zeros of the Hermite polynomial found in [125]. It is noted that the Gauss-Hermite used in (4.28) quickly converges for finite values of  $N$  (e.g.,  $N = 90$  terms).

#### 4.3.4. End-to-End Channel Statistical Model

We now analyze the end-to-end statistical models, i.e., cumulative density function (CDF), which is then used to obtain the performance metrics. The CDFs shown at the top of next page are derived for each link in the considered HAP-based SAGIN, including FSO-FSO1, FSO-FSO2, and FSO-RF (refer to Table 4.1 for the definition), as follows:

$$\begin{aligned}
F_{\gamma_{e2e}^f}(\gamma) &= \Pr\left(\frac{\gamma_{\text{SH}}^f \gamma_{\text{HG}}^f}{\gamma_{\text{HG}}^f + 1} < \gamma\right) \\
&= F_{\gamma_{\text{HG}}^f}\left(\frac{\gamma}{\gamma_{\text{SH}}^f - \gamma}\right) = \frac{1}{\Gamma(\alpha)\Gamma(\beta)} G_{1,3}^{2,1}\left[\alpha\beta\sqrt{\frac{\gamma}{\bar{\gamma}_{\text{HG}}^f(\gamma_{\text{SH}}^f - \gamma)}} \mid \alpha, \beta, 0\right].
\end{aligned} \tag{4.30}$$

$$\begin{aligned}
F_{\gamma_{e2e}^u}(\gamma) &= \Pr\left(\frac{\gamma_{\text{SH}}^f \gamma_{\text{HG}}^u}{\gamma_{\text{HG}}^u + 1} < \gamma\right) \\
&= F_{\gamma_{\text{HG}}^u}\left(\frac{\gamma}{\gamma_{\text{SH}}^f - \gamma}\right) = \sum_{i=1}^n \frac{w_i}{\sqrt{\pi}\Gamma(\alpha_1)\Gamma(\beta_1)\Gamma(\alpha_2)\Gamma(\beta_2)} \\
&\quad \times G_{1,5}^{4,1}\left[\frac{\alpha_1\beta_1\alpha_2\beta_2}{\sqrt{\bar{\gamma}_{\text{HG}}^u}}\left(\frac{\varpi}{\varpi+2}\right)^{\frac{1}{4}}\exp\left(\frac{x_i^2}{\varpi}\right)\sqrt{\frac{\gamma}{\gamma_{\text{SH}}^f - \gamma}} \mid \alpha_1 \ \beta_1 \ \alpha_2 \ \beta_2 \ 0\right].
\end{aligned} \tag{4.31}$$

$$\begin{aligned}
F_{\gamma_{e2e}^r}(\gamma) &= \Pr\left(\frac{\gamma_{\text{SH}}^f \gamma_{\text{HG}}^r}{\gamma_{\text{HG}}^r + 1} < \gamma\right) \\
&= F_{\gamma_{\text{HG}}^r}\left(\frac{\gamma}{\gamma_{\text{SH}}^f - \gamma}\right) = 1 - Q_1\left[\sqrt{2K}, \sqrt{\frac{2(K+1)}{\bar{\gamma}_{\text{HG}}^r}\left(\frac{\gamma}{\gamma_{\text{SH}}^f - \gamma}\right)}\right].
\end{aligned} \tag{4.32}$$

- FSO-FSO1 Link:** From (4.7) and (4.22), the CDF of end-to-end instantaneous SNR of the primary FSO-FSO1 link can be derived in (4.30). Here,  $\bar{\gamma}_{\text{HG}}$  is the average SNR for FSO-based HAP-to-GS link, and  $G_{p,q}^{m,n}(\cdot)$  is the MeijerG function.
- FSO-FSO2 Link:** From (4.29), we can derive the CDF of  $h_{\text{HG}}^u$ , i.e.,  $F_{h_{\text{HG}}^u}(h_{\text{HG}}^u)$ , and then the CDF of  $\gamma_{\text{HG}}^u$ , i.e.,  $F_{\gamma_{\text{HG}}^u}(\gamma_{\text{HG}}^u)$ , by using a variable transformation  $\gamma_{\text{HG}}^u = (\eta h_{\text{HG}}^u)^2 / \sigma_{n_y}^2$ . Here, the average SNR  $\bar{\gamma}_{\text{HG}}^u = \eta^2 \mathbb{E}[(h_{\text{HG}}^u)^2] / \sigma_{n_y}^2$ , where  $\mathbb{E}[(h_{\text{HG}}^u)^2] = (A_0^u h_1^u)^2 \sqrt{\frac{\varpi}{\varpi+2}}$  is derived in the Appendix A. From (4.10) and using the CDF of  $F_{\gamma_{\text{HG}}^u}(\gamma_{\text{HG}}^u)$ , the CDF of end-to-end SNR of the FSO-FSO2 link can be computed in (4.31).
- FSO-RF Link:** From (4.8) and (4.15), the CDF of end-to-end FSO-RF link can be obtained in (4.32).

Here, it is noted that PDFs of end-to-end instantaneous SNR for each link can be easily obtained from the derived CDFs by the following expression, i.e.,  $f_{\gamma_{e2e}}(\gamma) = \frac{\partial}{\partial \gamma} F_{\gamma_{e2e}}(\gamma)$ .

## 4.4. Performance Analysis

This section focuses on the performance analysis of the proposed system with rate adaptation transmission over atmospheric turbulence channels. In particular, the probability of transmission mode selection for the rate adaptation scheme is investigated, then used to analytically derive the performance metrics, including outage probability, average transmission rate, and spectrum efficiency.

### 4.4.1. Transmission Mode Selection Probability

As mentioned in section 4.2-C, to determine the mode selection probability for the system's performance analysis, we need to determine the switching SNR threshold levels. As reported in [67], these threshold levels are obtained based on the condition that the average BER for each transmission mode satisfies the targeted  $BER_0$ . As a result, the switching SNR threshold level for the transmission mode  $i$ -th can be given as

$$\gamma_{th_i}^* = \frac{-2(M-1)}{3} \ln(5BER_0), \quad (4.33)$$

where  $M$  is the modulation order [67]. In addition, the mode selection for each transmission link can be formulated as

$$\text{Mode Selection} = \begin{cases} \text{Mode } i\text{-th for FSO-FSO1} & \text{if } \gamma_{th_i}^f \leq \gamma_{e2e}^f < \gamma_{th_{i+1}}^f, \\ \text{Mode } j\text{-th for FSO-FSO2} & \text{if } \gamma_{th_j}^u \leq \gamma_{e2e}^u < \gamma_{th_{j+1}}^u, \\ \text{Mode } k\text{-th for FSO-RF} & \text{if } \gamma_{th_k}^r \leq \gamma_{e2e}^r < \gamma_{th_{k+1}}^r, \end{cases} \quad (4.34)$$

where  $i \in \{1, 2, \dots, N_1 - 1\}$ ,  $j \in \{1, 2, \dots, N_2 - 1\}$ , and  $k \in \{1, 2, \dots, N_3 - 1\}$  with  $N_1$ ,  $N_2$ , and  $N_3$  are the number of transmission modes for FSO-FSO1, FSO-FSO2, and FSO-RF links, respectively.

From (4.33) and (4.34), the probability that FSO-FSO1 link using the mode  $i$ -th for transmission can be given as

$$p_i^f = \int_{\gamma_{\text{th}_i}^f}^{\gamma_{\text{th}_{i+1}}^f} f_{\gamma_{e2e}}^f(\gamma) d\gamma = F_{\gamma_{e2e}}^f(\gamma_{\text{th}_{i+1}}^f) - F_{\gamma_{e2e}}^f(\gamma_{\text{th}_i}^f), \quad (4.35)$$

where  $f_{\gamma_{e2e}}^f(\cdot)$  and  $F_{\gamma_{e2e}}^f(\cdot)$  are respectively the PDF and CDF of FSO-FSO1 link found in (4.30). Regarding the FSO-FSO2 link, the probability of selecting the transmission mode  $j$ -th, given the outage occurs on the FSO-FSO1 link, can be expressed as

$$\begin{aligned} p_j^u &= \int_0^{\gamma_{\text{th}_1}^f} f_{\gamma_{e2e}}^f(\gamma) d\gamma \int_{\gamma_{\text{th}_j}^u}^{\gamma_{\text{th}_{j+1}}^u} f_{\gamma_{e2e}}^u(\gamma) d\gamma, \\ &= F_{\gamma_{e2e}}^f(\gamma_{\text{th}_1}^f) \left[ F_{\gamma_{e2e}}^u(\gamma_{\text{th}_{j+1}}^u) - F_{\gamma_{e2e}}^u(\gamma_{\text{th}_j}^u) \right], \end{aligned} \quad (4.36)$$

where  $\gamma_{\text{th}_1}^f$  is the outage threshold level of the FSO-FSO1 link, while  $f_{\gamma_{e2e}}^u(\cdot)$  and  $F_{\gamma_{e2e}}^u(\cdot)$  are respectively the PDF and CDF of the FSO-FSO2 link found in (4.31).

In addition, the FSO-RF link is activated when either (i) *outage of the FSO-FSO1 link due to strong turbulence (without UAV deployment)* or (ii) *both FSO-FSO1 and FSO-FSO2 links are not available (cloud blockage at the FSO-FSO1 link and strong turbulence at the FSO-FSO2 link)*. Then, the probability that FSO-RF link using the



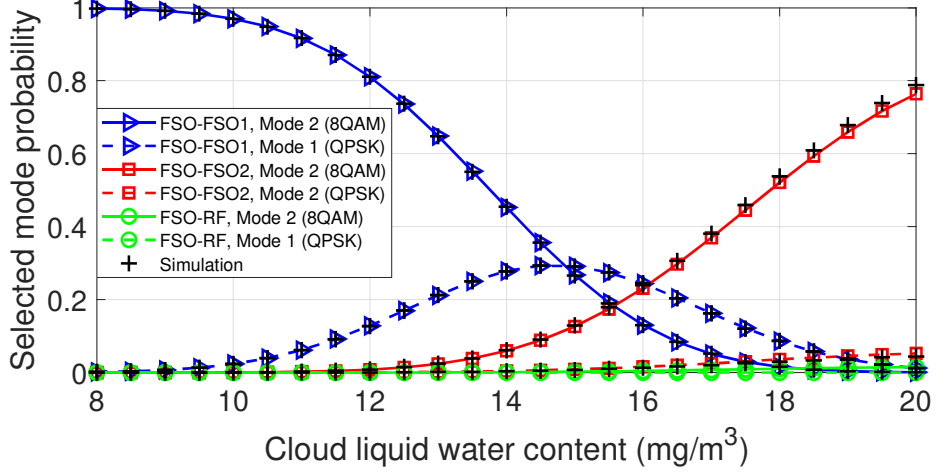


Figure 4.4: Selected mode probability vs. CLWC values for different transmission links with  $P_t = 11$  dBm,  $M_c^{\text{th}} = 10.3$  mg/m<sup>3</sup>, and  $N_1 = N_2 = N_3 = 2$  modes.

mode  $k$ -th for transmission can be formulated as

If  $\text{CWLC} < M_c^{\text{th}}$  : without the UAV deployment

$$\begin{aligned} p_k^r &= \int_0^{\gamma_{\text{th}_1}^f} f_{\gamma_{e2e}}^f(\gamma) d\gamma \int_{\gamma_{\text{th}_k}^r}^{\gamma_{\text{th}_{k+1}}^r} f_{\gamma_{e2e}}^r(\gamma) d\gamma, \\ &= F_{\gamma_{e2e}}^f(\gamma_{\text{th}_1}^f) \left[ F_{\gamma_{e2e}}^r(\gamma_{\text{th}_{k+1}}^r) - F_{\gamma_{e2e}}^r(\gamma_{\text{th}_k}^r) \right], \end{aligned} \quad (4.37)$$

If  $\text{CLWC} > M_c^{\text{th}}$  : with the UAV deployment

$$\begin{aligned} p_k^r &= \int_0^{\gamma_{\text{th}_1}^f} f_{\gamma_{e2e}}^f(\gamma) d\gamma \int_0^{\gamma_{\text{th}_1}^u} f_{\gamma_{e2e}}^u(\gamma) d\gamma \int_{\gamma_{\text{th}_k}^r}^{\gamma_{\text{th}_{k+1}}^r} f_{\gamma_{e2e}}^r(\gamma) d\gamma, \\ &= F_{\gamma_{e2e}}^f(\gamma_{\text{th}_1}^f) F_{\gamma_{e2e}}^u(\gamma_{\text{th}_1}^u) \left[ F_{\gamma_{e2e}}^r(\gamma_{\text{th}_{k+1}}^r) - F_{\gamma_{e2e}}^r(\gamma_{\text{th}_k}^r) \right], \end{aligned} \quad (4.38)$$

where  $\gamma_{\text{th}_1}^u$  is the outage threshold level of the FSO-FSO2 link, while  $f_{\gamma_{e2e}}^r(\cdot)$  and  $F_{\gamma_{e2e}}^r(\cdot)$  are the respectively PDF and CDF of FSO-RF link found in (4.32).

An example of the mode selection probability for different transmission links over a range of CLWC values is depicted in Fig 4.4. Using this figure, we can investigate the possibility of using transmission modes and links for different values of CLWC.

Specifically, with low CLWC values, the primary link (FSO-FSO1) can select the highest mode for the transmission. In addition, when the CLWC value increases, lower transmission modes are chosen for the primary link to satisfy the predefined QoS. The probability of using the primary link starts decreasing at high CLWC values, e.g.,  $\text{CLWC} = 14 \text{ mg/m}^3$  and higher, in which the system switches to the backup options, i.e., FSO-FSO2 and FSO-RF links.

#### 4.4.2. Performance Metrics

Using the transmission mode probabilities derived in section 4.4, we now investigate different performance metrics for our proposed system, including outage probability, average transmission rate, and spectrum efficiency.

##### 4.4.2.1. Outage Probability

The outage probability, denoted as  $P_{\text{out}}$ , is defined as the probability that the system moves to the zero-rate mode, where no data is transmitted to avoid the high error rate. It is computed as

$$\begin{aligned} P_{\text{out}} &= \int_0^{\gamma_{\text{th1}}^f} f_{\gamma_{e2e}}^f(\gamma) \int_0^{\gamma_{\text{th1}}^u} f_{\gamma_{e2e}}^u(\gamma) \int_0^{\gamma_{\text{th1}}^r} f_{\gamma_{e2e}}^r(\gamma) d\gamma, \\ &= F_{\gamma_{e2e}}^f(\gamma_{\text{th1}}^f) F_{\gamma_{e2e}}^u(\gamma_{\text{th1}}^u) F_{\gamma_{e2e}}^r(\gamma_{\text{th1}}^r), \end{aligned} \quad (4.39)$$

where  $f_{\gamma_{e2e}}^*(\cdot)$  and  $F_{\gamma_{e2e}}^*(\cdot)$  are the corresponding PDF and CDF, while  $\gamma_{\text{th1}}^f$ ,  $\gamma_{\text{th1}}^u$ , and  $\gamma_{\text{th1}}^r$  are the outage threshold levels for the FSO-FSO1, FSO-FSO2, and FSO-RF links, respectively.

#### 4.4.2.2. Average Transmission Rate

The average data bit rate for each transmission link can be calculated as

$$\begin{cases} \bar{R}_b^f = \sum_{i=1}^{N_1} p_i^f R_{b_i}^f, & \text{for the FSO-FSO1 link,} \\ \bar{R}_b^u = \sum_{j=1}^{N_2} p_j^u R_{b_j}^u, & \text{for the FSO-FSO2 link,} \\ \bar{R}_b^r = \sum_{k=1}^{N_3} p_k^r R_{b_k}^r, & \text{for the FSO-RF link,} \end{cases} \quad (4.40)$$

where  $p_i^f$  and  $p_j^u$  are given in corresponding (4.35) and (4.36), while  $p_k^r$  can be found in (4.37) and (4.38) [68]. Additionally,  $\{N_1, R_{b_i}^f\}$ ,  $\{N_2, R_{b_j}^u\}$ , and  $\{N_3, R_{b_k}^r\}$  represents for total number of transmission modes and data bit rate of the FSO-FSO1, FSO-FSO2, and FSO-RF links, respectively. From (4.40), the average system's transmission rate can be given as

$$\bar{R}_b = \bar{R}_b^f + \bar{R}_b^u + \bar{R}_b^r. \quad (4.41)$$

#### 4.4.2.3. Spectral Efficiency

It is supposed that a Nyquist pulse shaping filter with the bandwidth  $B = 1/R_s^*$ , where  $R_s^*$  is the symbol rate. The achievable spectral efficiency for different transmission links is, then, determined as

$$\begin{cases} \bar{S}_E^f = \frac{1}{R_s^f} \sum_{i=1}^{N_1} p_i^f R_{b_i}^f, & \text{for the FSO-FSO1 link,} \\ \bar{S}_E^u = \frac{1}{R_s^u} \sum_{j=1}^{N_2} p_j^u R_{b_j}^u, & \text{for the FSO-FSO2 link,} \\ \bar{S}_E^r = \frac{1}{R_s^r} \sum_{k=1}^{N_3} p_k^r R_{b_k}^r, & \text{for the FSO-RF link,} \end{cases} \quad (4.42)$$

where  $R_s^f$ ,  $R_s^u$ , and  $R_s^r$  are the fixed symbol rates of the FSO-FSO1, FSO-FSO2, FSO-RF links, respectively [67]. From (4.42), the average system's spectral efficiency can

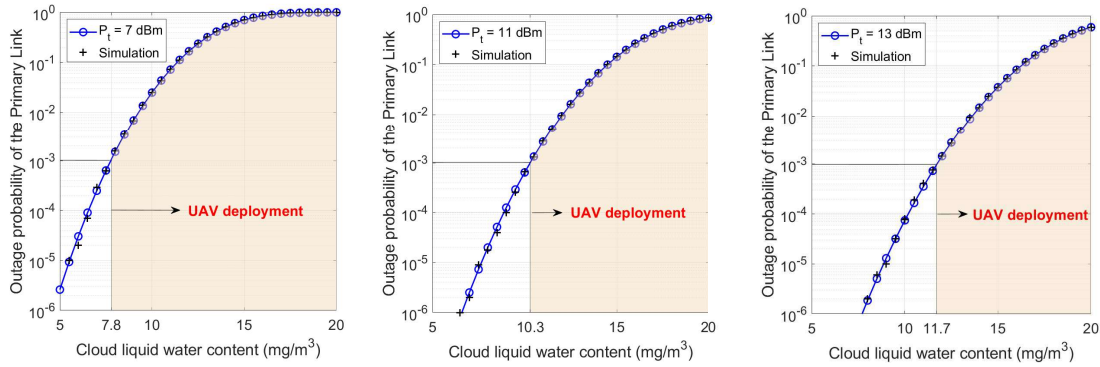


Figure 4.5: Outage performance of the primary FSO-FSO1 link versus CLWC for different satellite's transmitted powers.

be given as

$$\bar{S}_E = \bar{S}_E^f + \bar{S}_E^u + \bar{S}_E^r. \quad (4.43)$$

## 4.5. Numerical Results and Discussions

In this section, we present the performance evaluation for our proposed system analyzed in section 4.4 with different parameter settings. We also comparatively discuss the performance of our proposed system with the existing state-of-the-art systems, including all-optical HAP-assisted SAGIN and the hybrid FSO/RF-based HAP-assisted SAGIN proposed in [67], which highlights the effectiveness of our proposed system in the presence of cloud coverage. Regarding the rate adaptation design,  $N_1 = N_2 = N_3 = 3$  transmission modes, i.e., BPSK, QPSK, 8-QAM. In addition, the parameters, unless otherwise noted, are shown in Table 4.3. Monte Carlo simulations using MATLAB are also performed to validate the correctness of analytical results and good match can be confirmed.

### 4.5.1. Outage Performance

First, we investigate the time for deploying the RIS-UAV relay in our proposed system, which is determined by the CLWC threshold,  $M_c^{\text{th}}$ . To that purpose, the rule of thumb here is that we want to maximize the achievable data rate while saving the energy

Table 4.3: System Parameters

Name	Symbol	Value
<b>LEO Satellite</b>		
LEO satellite altitude	$H_{\text{SAT}}$	600 km
Divergence angle	$\theta_{\text{SAT}}$	15 $\mu\text{rad}$
Satellite's zenith angle	$\xi_{\text{SAT}}$	10°
<b>High Altitude Platform (HAP)</b>		
HAP altitude	$H_{\text{HAP}}$	20 km
HAP's aperture radius	$D_{\text{HAP}}$	10 cm
Divergence angle (HAP-GS beam)	$\theta_{\text{HG}}$	3 mrad
Divergence angle (HAP-UAV beam)	$\theta_{\text{HU}}$	4 mrad
HAP's zenith angle (HAP-GS beam)	$\xi_{\text{HG}}$	15°
HAP's zenith angle (HAP-UAV beam)	$\xi_{\text{HU}}$	20°
<b>Unnamed Aerial Vehicle (UAV)</b>		
UAV altitude	$H_{\text{UAV}}$	2.5 km
RIS jitter variance	$\sigma_{\text{RIS}}$	1 cm
UAV's zenith angle	$\xi_{\text{UAV}}$	60°
<b>Ground Station (GS)</b>		
GS altitude	$H_{\text{GS}}$	50 m
GS's aperture radius	$D_{\text{GS}}$	10 cm
<b>Other Parameters</b>		
Optical wavelength	$\lambda$	1550 nm
RF frequency	$f_c$	2 GHz
FSO symbol rate	$R_s^f, R_s^u$	500 Msps
RF symbol rate	$R_s^r$	50 Msps
Targeted BER	BER <sub>0</sub>	10 <sup>-5</sup>
Number of cloud concentrations	$N_c$	250 cm <sup>-3</sup>
Vertical extent of cloud	$d_c^f, d_c^r$	2 km
Turbulent factors (HAP-GS link)	$\alpha - \beta$	7.5 - 6.5
Turbulent factors (HAP-UAV link)	$\alpha_1 - \beta_1$	7.2 - 6.2
Turbulent factors (UAV-GS link)	$\alpha_2 - \beta_2$	5.6 - 4.1
Rician factor	$K$	6 dB
Noise spectral density	$\sigma_n^2$	$2 \times 10^{-23}$ A <sup>2</sup> /Hz

consumption of the UAV. As a result, the UAV needs to deploy when the outage performance of the primary link (FSO-FSO1) is about to happen, which is decided by a predefined outage level. Specifically, Fig. 4.5 analyzes the outage performance of the primary FSO link over a range of CLWC values. Also, different satellite's powers, i.e.,  $P_t = 7$  dBm,  $P_t = 11$  dBm, and  $P_t = 13$  dBm, are considered. We could find the CLWC thresholds from a predefined outage level that the UAV should be deployed using this figure. For example, with the predefined outage level of 10<sup>-3</sup>, the

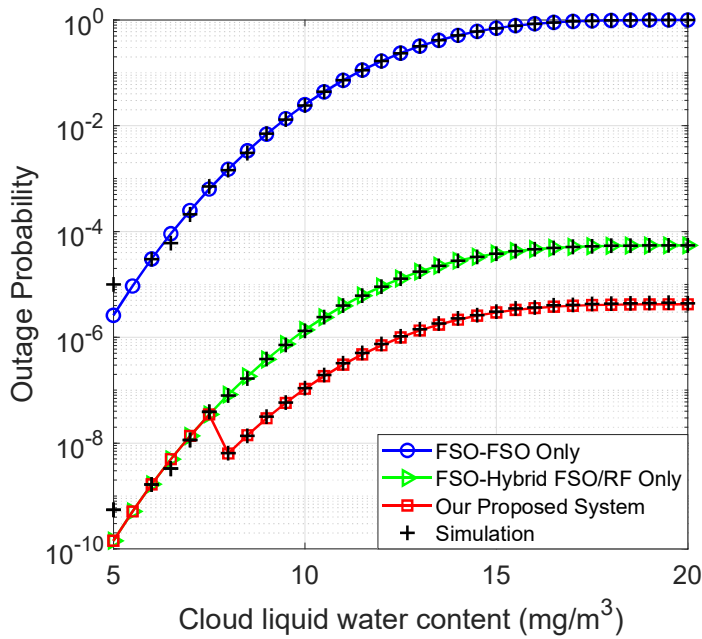


Figure 4.6: Outage performance of different systems versus CLWC, when  $P_t = 7$  dBm.

UAV should be deployed at the time that  $CLWC = 7.8 \text{ mg/m}^3$ ,  $10.3 \text{ mg/m}^3$ , and  $11.7 \text{ mg/m}^3$  for the transmitted power levels of 7 dBm, 11 dBm, and 13 dBm, respectively. Next, we highlight the effectiveness of our proposed system in comparison with (i) all-optical HAP-assisted SAGIN (FSO-FSO Only) and (ii) the hybrid FSO/RF-based HAP-assisted SAGIN (FSO-Hybrid FSO/RF Only) proposed in [67]. Particularly, Fig. 4.6 investigates the system's outage performance for different CLWC values, when  $P_t = 7$  dBm and CLWC threshold  $M_c^{\text{th}} = 7.8 \text{ mg/m}^3$ . As is expected, in the presence of clouds, our proposed system outperforms the existing ones in terms of outage performance. The reason is that when the CLWC increases, the outage performance of the system with FSO-FSO only is significantly deteriorated. In contrast, our proposed system can maintain a better performance than the FSO-hybrid FSO/RF system in [67] because it can attain spatial diversity with the aid of RIS-UAV relay. For instance, to retain the outage level of  $10^{-6}$ , our proposed system can operate under the CLWC value of  $12.5 \text{ mg/m}^3$ , while they are  $5 \text{ mg/m}^3$  and  $10 \text{ mg/m}^3$  for the system with FSO-FSO only and one with FSO-hybrid FSO/RF only, respectively. Figure 4.7 focuses on the selection of GS's aperture size to maintain a required out-

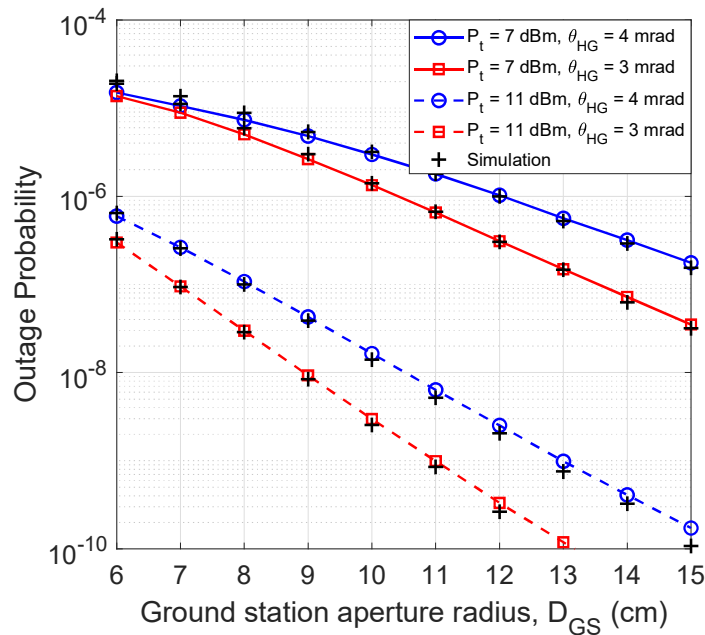


Figure 4.7: Outage performance versus GS's aperture radius for different satellite's transmitted powers and HAP's zenith angles.

age performance for the proposed system under the impact of cloud, e.g.,  $M_c = 13$  mg/m<sup>3</sup>. Also, different satellite's transmitted powers, i.e.,  $P_t = 7$  dBm ( $M_c^{\text{th}} = 7.8$  mg/m<sup>3</sup>) and 11 dBm ( $M_c^{\text{th}} = 10.3$  mg/m<sup>3</sup>), are taken into account. Additionally, different divergence angles for HAP-GS beam, i.e.,  $\theta_{HG} = 3$  mrad and 4 mrad, are considered. Using this figure, we can select a proper GS's aperture size for the given satellite's transmitted power and divergence angle for HAP-GS beam to retain a specific system's outage level. For example, when  $P_t = 7$  dBm (or  $P_t = 11$  dBm), the GS's aperture size should be 14 cm (or 7 cm) to maintain an outage level of  $10^{-7}$  for the corresponding HAP-GS beam's divergence angles, i.e.,  $\theta_{HG} = 3$  mrad.

#### 4.5.2. Average Transmission Rate and Spectral Efficiency

We are now able to analyze the other essential system performance metrics, including average transmission rate and spectral efficiency under the impact of clouds.

We further highlight the effectiveness of our proposed system in terms of average transmission rate performance. Figure 4.8 analyzes the average transmission rate over a range of CLWC values. Also,  $P_t = 11$  dBm and  $M_c^{\text{th}} = 10.3$  mg/m<sup>3</sup>. As is

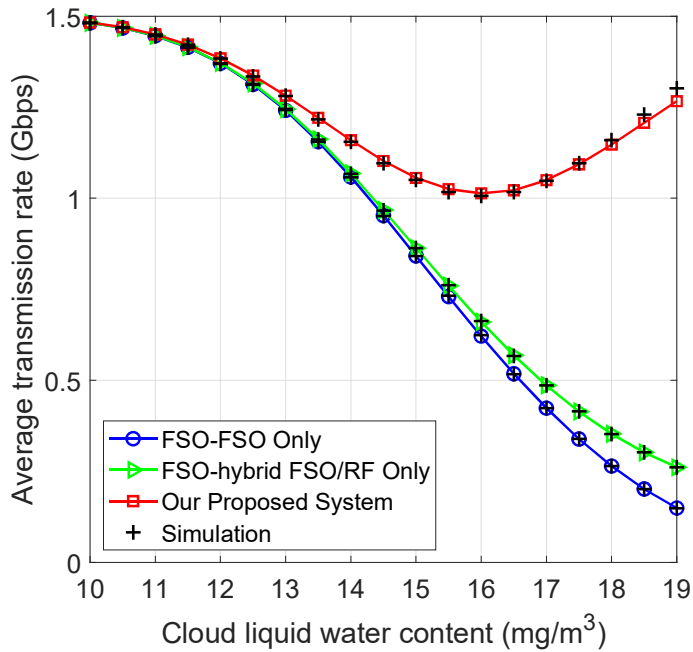


Figure 4.8: Average transmission rate of different systems versus CLWC, when  $P_t = 11$  dBm.

expected, our proposed system can achieve a considerable enhancement in terms of achievable rate in comparison with the systems with FSO-FSO only as well as with FSO-hybrid FSO/RF only as in [67]. At high CLWC values, while the achievable data rates significantly decrease in systems with FSO-FSO only (deteriorated by clouds) and with FSO-hybrid FSO/RF only (switching to the lower-rate mode of RF link), our proposed system can even attain a higher data rate due to the fact that the UAV-assisted FSO-FSO2 link can have more chance to select higher data-rate modes for transmission. For example, when  $CLWC = 18 \text{ mg/m}^3$ , our proposed system can maintain the achievable data rate of 1.15 Gbps, while they are merely 264 Mbps and 352 Mbps for the systems with FSO-FSO only and with FSO-hybrid FSO/RF only, respectively.

In Fig. 4.9, we analyze the achievable data rate of the proposed multi-rate adaptation design for the backup FSO-FSO2 link in comparison with the fixed-rate schemes. Also,  $P_t = 7$  dBm,  $M_c^{\text{th}} = 7.8 \text{ mg/m}^3$ , and different fixed-rate schemes, i.e.,  $M_2 = 2$  (BPSK),  $M_2 = 4$  (QPSK), and  $M_2 = 8$  (8-QAM), are taken into account. As



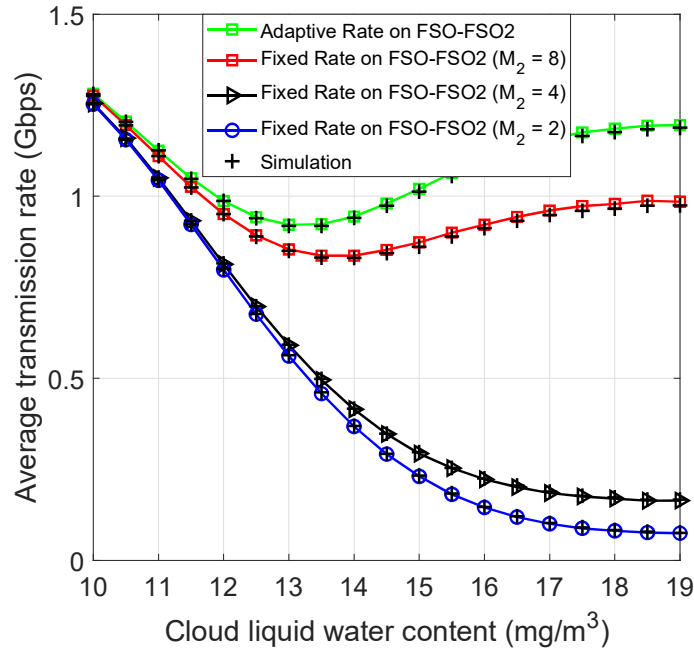


Figure 4.9: Average transmission rate versus CLWC for (i) fixed rate and (ii) adaptive rate on FSO-FSO2 link, when  $P_t = 11$  dBm.

is expected, the proposed system with FSO-FSO2 link using the rate adaptation scheme offers considerably better achievable data rate than the one using the fixed-rate scheme. For instance, when  $CLWC = 18$  mg/m<sup>3</sup>, the system with FSO-FSO2 link using the rate adaptation scheme can achieve 1.17 Gbps, while that using the fixed-rate scheme can maintain only 83 Mbps, 173 Mbps, and 0.96 Gbps for  $M_2 = 2$ ,  $M_2 = 4$ , and  $M_2 = 8$ , respectively.

Figure 4.10 investigates altitudes for the deployment of RIS-UAV relay in terms of achievable data rate over a range of CLWC. We set the satellite's transmitted power  $P_t = 11$  dBm. Also, different HAP's altitude, i.e.,  $h_{HAP} = 20$  and 24 km, are considered. As seen, when the CLWC value increases, the system has more chance to select the UAV-assisted FSO-FSO2 link for transmission, resulting in an increase in achievable data rate. In addition, using this figure, we can decide the altitude for deploying the RIS-UAV relay and HAP. A higher achievable data rate can be achieved with lower UAV and HAP altitudes due to smaller RIS's virtual divergence angle for the UAV-GS beam, defined by a ratio between HAP-UAV and UAV-GS distances.

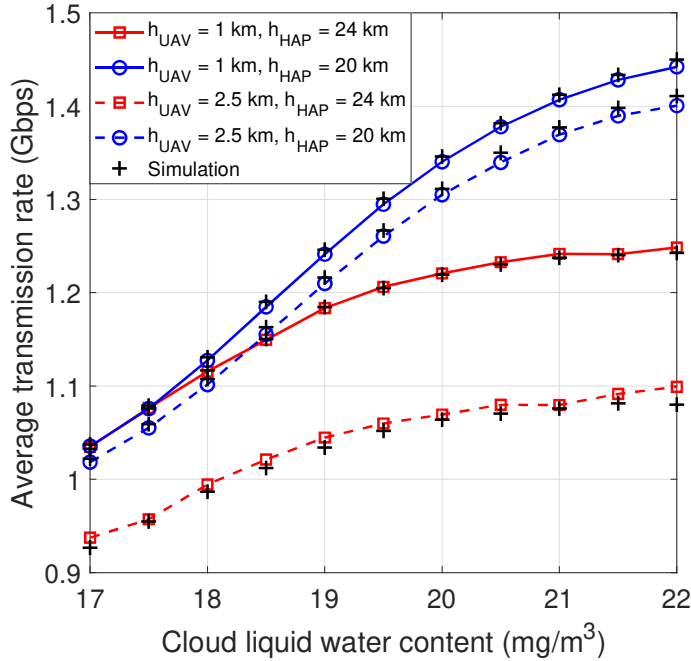


Figure 4.10: Average transmission rate versus CLWC for different UAV's altitudes, when  $P_t = 11$  dBm.

The rule of thumb here is to maintain a targeted achievable data rate while quickly deploying the RIS-UAV relay. As a result, for example, when  $CLWC = 19$  mg/m<sup>3</sup>, the HAP and RIS-UAV relay should be deployed at the altitude of 20 km and 1 km, respectively, to retain a targeted achievable data rate of 1.25 Gbps.

Finally, we highlight the effectiveness of our proposed system in terms of average spectral efficiency. Figure 4.11 investigates the average spectral efficiency of different systems over a range of CLWC values. This figure shows a considerable achievable spectral efficiency improvement of the proposed system compared to those with FSO-FSO only and with FSO-hybrid FSO/RF only. For instance, when  $CLWC = 19$  mg/m<sup>3</sup>, the achievable spectral efficiency of our proposed system is 2.5 bits/symbol. In comparison, they are 0.29 bits/symbol and 0.52 bits/symbol for the systems with FSO-FSO only and with FSO-hybrid FSO/RF only.

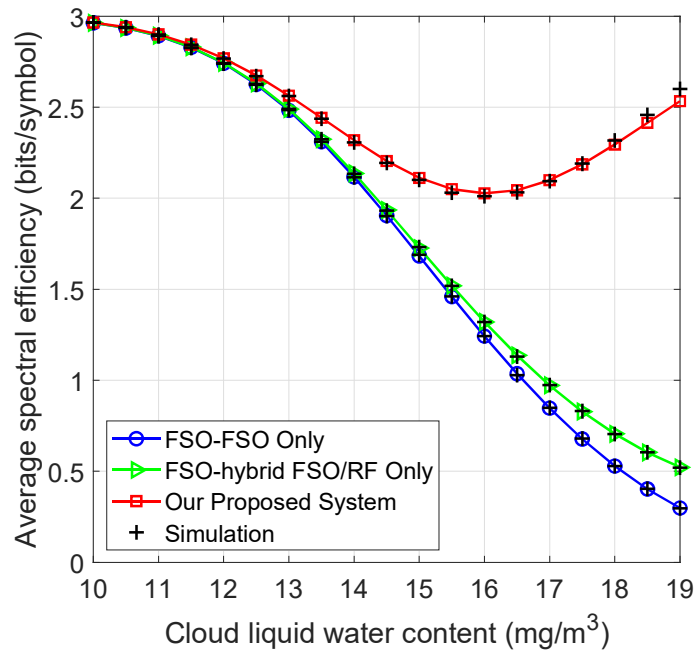


Figure 4.11: Average spectral efficiency of different systems versus CLWC, when  $P_t = 11$  dBm.

### 4.5.3. Design Guidelines

From the obtained insightful numerical results, we now provide the design guidelines recommended for effectively designing our proposed system in the presence of cloud coverage, as follows.

- Given a predefined outage level of  $10^{-3}$  for the primary FSO-FSO1 link, the CLWC thresholds for deploying RIS-UAV relay are  $M_c^{\text{th}} = 7.8$  mg/m<sup>3</sup>, 10.3 mg/m<sup>3</sup>, and 11.7 mg/m<sup>3</sup> for the satellite's transmitted power levels of 7 dBm, 11 dBm, and 13 dBm, respectively.
- When  $P_t = 7$  dBm and  $M_c^{\text{th}} = 7.8$  mg/m<sup>3</sup>, to maintain the outage level of  $10^{-6}$ , our proposed system can operate under the CLWC value of 12.5 mg/m<sup>3</sup>, while they are 5 mg/m<sup>3</sup> and 10 mg/m<sup>3</sup> for respectively the system with FSO-FSO only and one with FSO-hybrid FSO/RF only, which highlights the effectiveness of our proposed system.
- When  $P_t = 7$  dBm (or  $P_t = 11$  dBm), the GS's aperture size should be 14 cm

(or 7 cm) to maintain an outage level of  $10^{-7}$  for the corresponding HAP-GS beam's divergence angles, i.e.,  $\theta_{\text{HG}} = 3$  mrad.

- At higher CLWC values, our proposed system can achieve a higher data rate (more chance to select higher transmission modes). In contrast, achievable data rates significantly decrease in systems with FSO-FSO only and with FSO-hybrid FSO/RF only. For example, when  $P_t = 11$  dBm and  $\text{CLWC} = 18$  mg/m<sup>3</sup>, our proposed system can maintain the achievable data rate of 1.15 Gbps, while they are merely 264 Mbps and 352 Mbps for the systems with FSO-FSO only and with FSO-hybrid FSO/RF only, respectively.
- The effectiveness of multi-rate adaptation scheme is confirmed, in which, for example, when  $P_t = 7$  dBm and  $\text{CLWC} = 18$  mg/m<sup>3</sup>, the system with FSO-FSO2 link using the rate adaptation scheme can achieve 1.17 Gbps, while that using the fixed-rate scheme can maintain only 83 Mbps, 173 Mbps, and 0.96 Gbps for  $M_2 = 2, 4, 8$ , respectively.
- The higher achievable data rate can be achieved with higher UAV altitudes due to smaller RIS's virtual divergence angle for the UAV-GS beam, defined by a ratio between HAP-UAV and UAV-GS distances. When  $\text{CLWC} = 19$  mg/m<sup>3</sup>, for the quick deployment, the HAP and RIS-UAV relay should be deployed at the altitude of 20 km and 1 km to retain a targeted achievable data rate of 1.25 Gbps.
- The effectiveness of our proposed system in terms of achievable spectral efficiency is confirmed, in which, for instance, when  $\text{CLWC} = 19$  mg/m<sup>3</sup>, our proposed system can achieve 2.5 bits/symbol. In comparison, they are 0.29 bits/symbol and 0.52 bits/symbol for respectively systems with FSO-FSO only and with FSO-hybrid FSO/RF only.

It is worthy that the above design guidelines are useful for practical deployment of network scenarios, e.g, space-assisted vertical backhaul/fronthaul solutions for wire-

less mobile networks. Our network could be complementary to the terrestrial backhaul/fronthaul networks in some situations. For instance, it is deployed in case of failure in the terrestrial networks or temporary demand for backhaul/fronthaul during a social event such as sporting events. Moreover, our network is capable of offering backhaul/ fronthaul to the small-cell base stations that are located in hard-to-reach areas where fiber or microwave links may not be readily available and expensive to deploy. Examples of these locations could be in rural/remote or urban areas.

## 4.6. Conclusions

In this Chapter, we have proposed to deploy the additional UAV equipped with a RIS array in the HAP-based SAGIN to enhance the system performance under the impact of weather conditions. We also proposed a link switching scheme and rate adaptation design. Several performance metrics, including outage probability, average transmission rate, and spectral efficiency, were analytically obtained. Numerical results illustrated the outperformance of the proposed system compared to the existing state-of-the-art ones over the turbulence fading channels. We also provided the design guidelines that can be helpful for the practical system design of RIS-UAV relay-assisted HAP-based SAGIN. Future work would be interesting to investigate the deployment of multiple RIS-UAV relays. The spatial diversity can be attained using selection combining, equal-gain combining, and maximum ratio combining schemes.

# Chapter 5

## Site Diversity Technique

This chapter<sup>7</sup> address the link availability in satellite-based free-space optical (FSO) communications. In particular, we present an accurate analysis for the estimation of the link availability in the presence of clouds and atmospheric turbulence. For this purpose, a 5-years reanalysis meteorological ERA-Interim database, produced by European Center for Medium-Range Weather Forecast (ECMWF), is investigated. The cloud liquid water content (CLWC) obtained from ECMWF database is used to analyze the link availability for several regions in Japan. In addition, the site diversity scheme is also investigated to enhance the system availability.

### 5.1. Introduction

In recent years, broadband satellite networks using free-space optical (FSO) communications have attracted considerable attention from both academia and industry thanks to the combined advantage of global coverage and huge bandwidth connectivity [126]. The primary concerns of FSO are the atmospheric turbulence and cloud blockage [57], which can severely deteriorate the system performance and link avail-

---

<sup>7</sup>The content of this Chapter was presented in part in

1. Thang V. Nguyen *et. al.*, “Link availability of satellite based FSO communications in the presence of clouds and turbulence,” IEICE Communications Express, Vol. 10, No. 5, pp. 206-211, Feb. 2021.

## 5.1 Introduction

ability. For this reason, an investigation of the link availability in particular sites of interest should be performed in planning and designing a satellite-based FSO communications system.

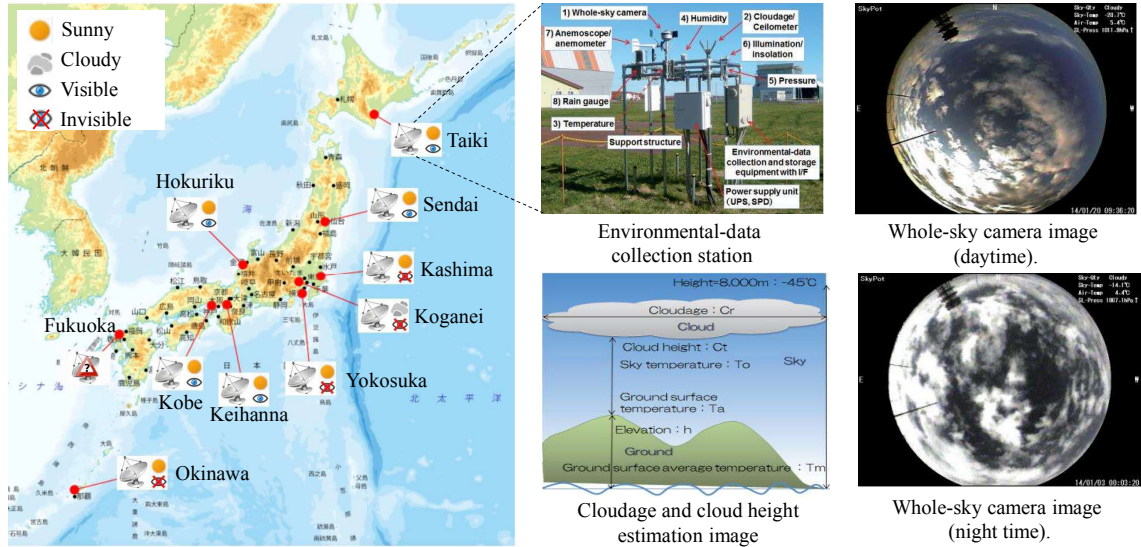


Figure 5.1: Site diversity implementation in Japan [8].

Driven by the recent development of the satellite-based FSO networks, there are number of works focus on investigating the site diversity scheme to avoid the effects of clouds [8,127–130]. In [8,127], the motivation of these works is to verify the site diversity taking actual satellite orbits into account through on-site long-term acquisition, storage, and analysis of cloud data such as the altitude, cloudage, and the distribution of clear sky region. Figure 5.1 depicts optical ground stations where collects the cloud data. An example of a field installation of an environmental-data collection station is illustrated in Fig. 5.1. At that location, a whole-sky camera is implemented to measure the cloudage/ceilometer for estimating the height of clouds, temperature, and various other weather sensors. The data is acquired from the whole-sky camera for identifying clear-sky regions during daytime and nighttime as shown in Fig. 5.1. The observed data is sent to the sever (central station) via the terrestrial network, stored in the database, statistically processed and analyzed. However, to confirm the effectiveness of the site-diversity as proposed in [8,127], the data needs to collect, store, and analyze during a long period, i.e., at least three years. Besides, for the large-scale network consideration, the complex facilities are required for all of stations.

There is an alternative approach that is cost-efficient, easy implementation, and has good accuracy. That approach is based on CLWC data from the available databases observed by satellites, e.g., the European Center for Medium-Range Weather Forecast (ECMWF) database [27]. There are several studies on the investigation of the site diversity scheme based on the CLWC data analysis approach [128–130]. In those works, authors proposed an ON/OFF channel and investigated a methodology for the calculation of cloud-free line-of-sight (CFLOS) probability based on the CLWC for the optical satellite systems. Those works highlighted the use of monthly statistics of cloud coverage for the design of FSO-based satellite links. Based on monthly variation of cloud coverage statistics, the site diversity technique is used to investigate the minimum number of ground station satisfying the link availability requirement.

This letter, therefore, aims to provide a more accurate analysis for the estimation of the link availability considering the impact of both clouds and atmospheric turbulence. First, we obtain the CLWC data from the meteorological ERA Interim database produced by the European Center for Medium Range Weather Forecast (ECMWF) [27]. Based on the cloud attenuation statistical model developed in [25], the data is, then, used to derive the link availability for several regions in Japan. In addition, site diversity scheme is also investigated to improve the link availability.

## 5.2. Network Descriptions

A satellite-based FSO network is illustrated in Fig. 5.2, in which we consider laser downlinks from a satellite to multiple ground stations (GSs)<sup>8</sup>. During the downlink transmission, FSO links may experience (a) cloud blockage, (b) clouds with low CLWC values that the connection is still maintained, and (c) clear sky. In the following, we focus on the two major impairments on the FSO links, namely cloud attenuation and atmospheric turbulence.

---

<sup>8</sup>The optical ground stations shown in Fig. 5.2 are developed by NICT, Japan.



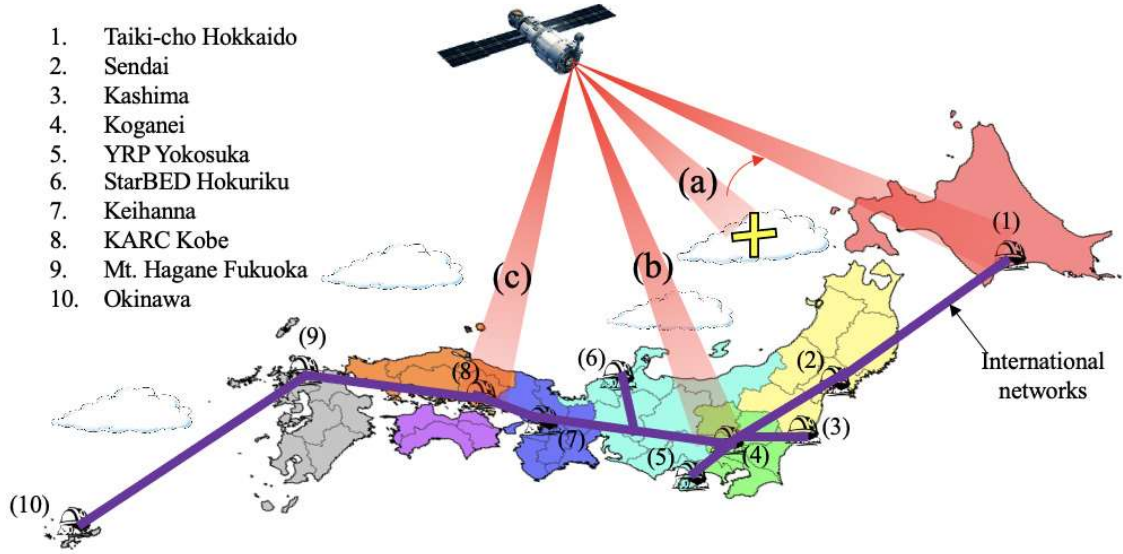


Figure 5.2: Satellite downlinks with multiple ground stations.

### 5.2.1. Cloud Attenuation

The liquid water particles in clouds cause the scattering phenomenon of the laser beam propagation, leading to the decrease of visibility and significant attenuation of signal power. Based on the CLWC data obtained from the ERA Interim database [27], the visibility (km) can be estimated as

$$V = \frac{1.002}{(L \times N_c)^{0.6473}}, \quad (5.1)$$

where  $L$  (g/m<sup>3</sup>) is the CLWC value and  $N_c$  (cm<sup>-3</sup>) is the cloud droplet number concentration. Using Mie theory, the visibility is then used to derive the cloud attenuation, which can be found in [25].

According to [25], the log-normal distribution can be used to accurately model the cloud attenuation whose the probability density function (PDF) is given as

$$f_{A_c}(A_c) = \frac{1}{\sqrt{2\pi}\sigma A_c} \exp\left[-\frac{(\ln A_c - \mu)^2}{2\sigma^2}\right], \quad (5.2)$$

where  $A_c$  is the cloud attenuation expressed in dB while  $\sigma$  and  $\mu$  are obtained based on the maximum likelihood estimation of the curve-fitting method.

### 5.2.2. Atmospheric Turbulence

The atmospheric turbulence phenomenon causes the scintillation effect, which results in fluctuations in the received signal power. The turbulence strength is determined by the Rytov variance, denoted as  $\sigma_R^2$ , where weak, moderate and strong turbulence conditions correspond to  $\sigma_R^2 < 1$ ,  $\sigma_R^2 \approx 1$  and  $\sigma_R^2 > 1$ , respectively [57]. For the satellite-to-ground optical channels, the Rytov variance in the case of plane wave propagation is given as

$$\sigma_R^2 = 2.25 \left( \frac{2\pi}{\lambda} \right)^{7/6} \sin^{-11/6}(\theta) \int_{H_G}^{H_{sat}} C_n^2(h) (h - H_G)^{5/6} dh, \quad (5.3)$$

where  $\lambda$  (nm) is the optical wavelength,  $\theta$  is the satellite elevation angle, while  $H_G$  and  $H_{sat}$  are the receiver and satellite altitudes, respectively. In addition,  $C_n^2(h)$  is the altitude-dependent index structure parameter, which can be found in [57].

## 5.3. Performance Analysis

This Section focusses on an estimation of the link availability. Specifically, we first analyze the power loss due to the cloud attenuation and atmospheric turbulence. The link availability is, then, estimated based on the obtained power loss. In addition, site diversity scheme is also investigated to improve the link availability.

### 5.3.1. Power Loss

The power loss due to the cloud attenuation and atmospheric turbulence, denoted as  $A_{loss}$  (dB), can be expressed as

$$A_{loss} = A_c + A_t, \quad (5.4)$$

where  $A_t$  is the power loss caused by the turbulence-induced fading.

Let  $d_{fso}$  be the distance from the satellite to the ground station,  $A_t$  (dB) is then given

by

$$A_t = 4.343 \left[ \operatorname{erfcinv}(2p_{\text{th}}) \sqrt{2 \ln(\sigma_P^2 + 1)} - \frac{1}{2} \ln(\sigma_P^2 + 1) \right], \quad (5.5)$$

where  $\sigma_P^2 = \sigma_R^2 \left[ 1 + 0.33 \left( \frac{\pi D^2}{2\lambda d_{\text{fso}}} \right)^{5/6} \right]^{-7/5}$  is the power scintillation index with  $D$  being the receiver aperture diameter and  $p_{\text{th}} = 10^{-2}$  [131]. On the other hand, the cloud attenuation  $A_c$  can be written as

$$A_c = \sum_{k=1}^M 4.343 \left[ \frac{3.91}{V_k} \left( \frac{\lambda}{550} \right)^{-\delta_k} \right] \frac{\Delta h_k}{\sin(\theta)}, \quad (5.6)$$

where  $M$  is the total cloud layers considered while  $V_k$  and  $\Delta h_k$  are the visibility and the vertical extent of the  $k$ -th layer, respectively [25]. In addition,  $\delta_k$  depends on  $V_k$ , which can be found in [57].

### 5.3.2. Link Availability

Given the power loss in (5.4), the link availability can be estimated by

$$P_{\text{avai}} = \Pr[A_{\text{loss}} \leq A_{\text{budget}}] = \Pr[A_c \leq A_{\text{budget}} - A_t], \quad (5.7)$$

where  $A_{\text{budget}}$  (dB) is the total link budget for the cloud attenuation and turbulence loss. Based on (5.2) and given  $A_{\text{th}} = A_{\text{budget}} - A_t$  (dB), (5.7) is rewritten as

$$P_{\text{avai}} = \int_0^{A_{\text{th}}} f_{A_c}(A_c) dA_c = \frac{1}{2} + \frac{1}{2} \operatorname{erf} \left[ \frac{\ln(A_{\text{th}}) - \mu}{\sqrt{2}\sigma} \right]. \quad (5.8)$$

### 5.3.3. Site Diversity Technique

To improve the link availability, we consider site diversity technique. Let  $K$  denote the total number of sites that are available for communications. By applying the technique, the link availability, which is defined when at least one station is available

at any time, can be determined as

$$A = 1 - \prod_{i=1}^K \Pr[A_{\text{loss}}(i) > A_{\text{budget}}] = 1 - \prod_{i=1}^K P_{\text{non}}(i), \quad (5.9)$$

where  $P_{\text{non}}(i) = 1 - P_{\text{avai}}(i)$ , with  $P_{\text{avai}}$  being given in (5.8), is the probability that the  $i$ -th station is not available at a given time.

## 5.4. Results and Discussions

In this Section, numerical results of the link availability during rainy season (i.e., July) in a 5-year period (2015-2019) for several regions in Japan are presented. The CLWC data are collected with one sample every hour over a spatial resolution of  $0.25^\circ \times 0.25^\circ$  latitude/longitude grid and with  $M = 5$  cloud layers within 1-3 km above sea level. For simulations of the atmospheric turbulence, the optical wavelength of  $\lambda = 1550$  nm, satellite elevation angle  $\theta = 40^\circ$ , satellite altitude  $H_{\text{sat}} = 36,000$  km, receiver aperture diameter  $D = 10$  cm, and receiver altitude  $H_G = 10$  m are chosen.

### 5.4.1. Impact of Clouds on Link Availability

Firstly, we investigate the impact of clouds without considering the atmospheric turbulence. In this scenario, Fig. 5.3 illustrates the link availability for 47 prefectures in Japan when the link budget for the cloud attenuation is 30 dB. It is observed that Hokkaido and Shikoku achieve the highest and lowest levels of link availability during the rainy season, respectively. In addition, the link availability decreases from the north to the south of Japan. From the network design perspective, the obtained results are useful in deciding the optical GSs that can communicate reliably with the satellite.

### 5.4.2. Joint Impact of Clouds and Atmospheric Turbulence

Next, Fig. 5.4(a) depicts the link availability in Tokyo over a range of link budgets under the joint impact of clouds and atmospheric turbulence. Here, the total link

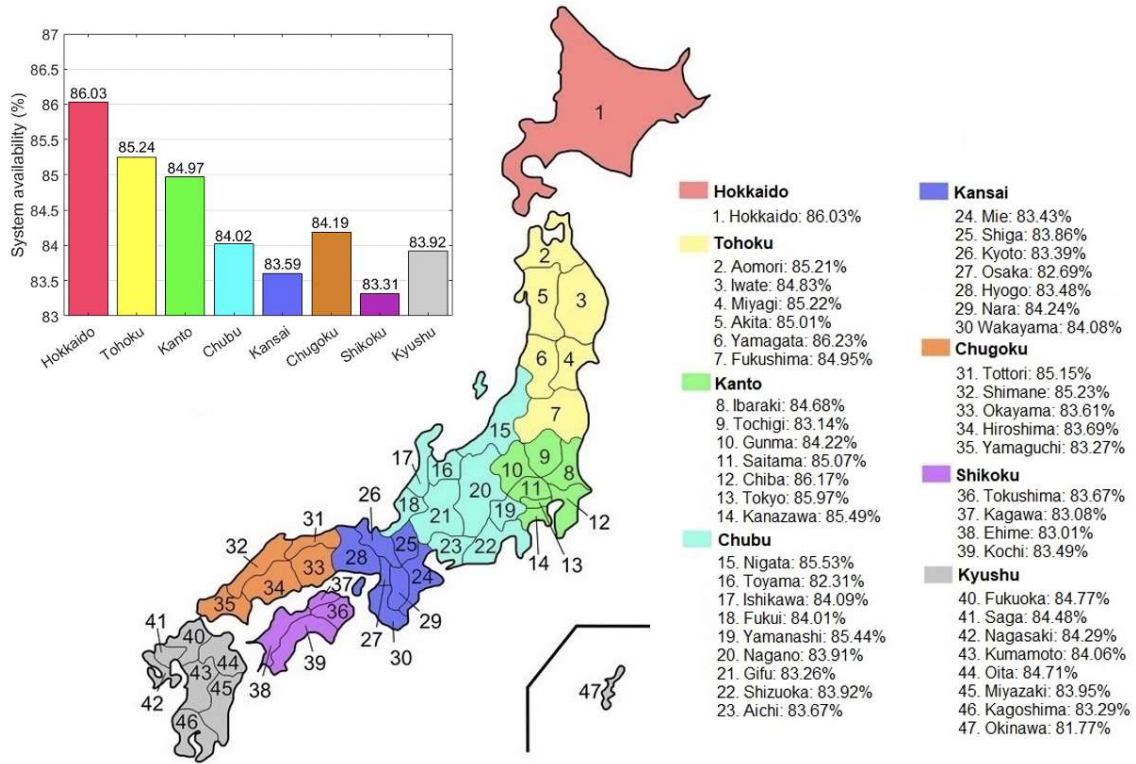


Figure 5.3: Link availability in Japan during rainy season.

budget,  $A_{\text{budget}}$ , for the cloud attenuation and turbulence loss is considered. As seen from the figure, severe clouds combined with the atmospheric turbulence significantly deteriorate the link availability. For instance, when  $A_{\text{budget}} = 30$  dB, the link availability are 86%, 83%, and 82% in no turbulence, weak turbulence, and strong turbulence cases, respectively.

Finally, we highlight the advantage of site diversity technique in improving the link availability in Fig. 5.4(b) when  $A_{\text{budget}} = 30$  dB and  $C_n^2(0) = 10^{-13}$ . It is evident that the link availability increases with the number of GSs. For example, the link availability reaches 99.29% when using three GSs.

## 5.5. Conclusions

This letter has presented an estimation for the link availability of satellite-based FSO communications in the presence of clouds and atmospheric turbulence. The 5-year reanalysis meteorological ECMWF ERA Interim database for Japan was used for the

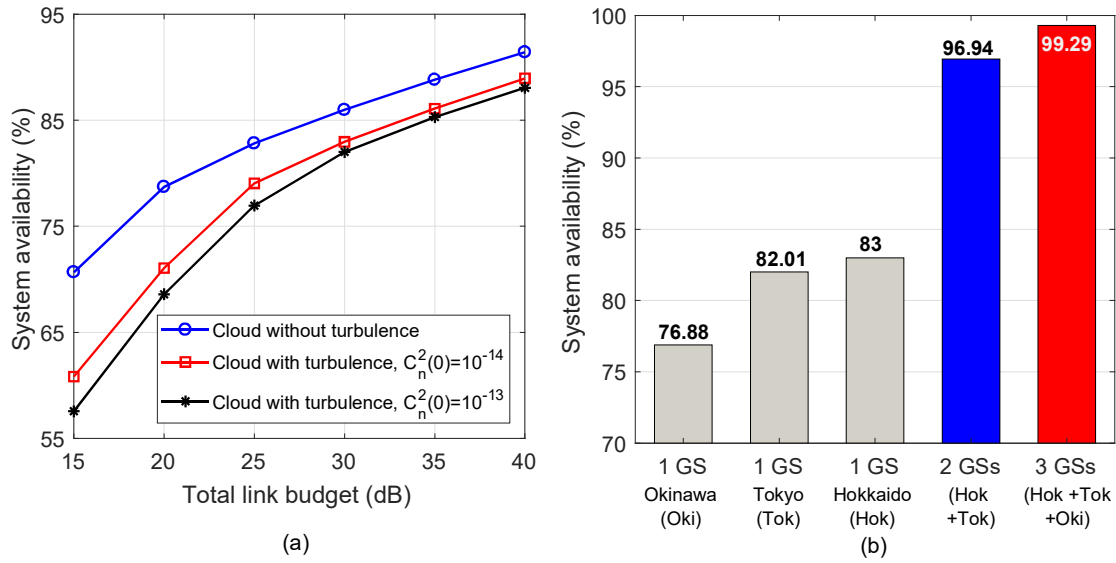


Figure 5.4: Link availability (a) without site diversity, (b) with site diversity.

investigation. Site diversity technique was employed to improve the link availability. Comprehensive numerical results were presented to show the link availability during rainy season and to confirm the effectiveness of using site diversity technique.

# Chapter 6

## Summaries and Future Research

### 6.1. Summaries

A mission of the next-generation network is to connect the remaining half of the world due to nearly 50% of the population being unconnected to the Internet nowadays. Two main barriers that restrict connectivity are the lack of infrastructure and affordability. To address these issues, optical satellite communications have recently emerged as a complementary solution to bridge the gap by offering Internet connectivity at a reasonable cost and ubiquitous coverage. On the one hand, the advantage of satellite communication is expanding connectivity to uncovered and under-served regions. On the other hand, FSO communication has been considered as an alternative for low-cost, energy-efficiency, and effective broadband wireless connectivity thanks to the use of a new and vast unlicensed optical spectrum. The combination of satellite and FSO communication, therefore, is a potential technology for the development of the next-generation network.

The optical links from space are subject to atmospheric-related issues, such as atmospheric attenuation, atmospheric turbulence-induced fading, and weather-induced disruption. Besides, misalignment loss is a critical problem in satellite-based FSO communication since it could arise due to many reasons such as UAV hovering, ground

station fluctuation, etc. From this perspective, this dissertation focuses on the design and performance evaluation of satellite-based FSO communications, considering the adverse issues. To do so, we propose several mitigation techniques to improve the system performance. Firstly, to provide broader coverage and flexible deployment, both high and low-altitude UAVs are proposed as a relay node to avoid cloud coverage. High altitude UAV, also known as HAP, can be an airship, aircraft, or balloon, is a low-cost solution that inherits most of the advantages of the satellite. Besides, the mirror array, also known as RIS, is mounted on the UAV to quickly reflect and forward the signal from HAP to the user terminal. Secondly, the hybrid FSO/RF system is used in optical satellite communication to improve the overall system availability. In a hybrid system, the lower data rate RF link is considered as a backup link when the optical channel condition is insufficient to maintain the high data rate. Moreover, the rate adaptation design is applied to the hybrid system to avoid frequently switching between FSO and RF links. Finally, we apply the site diversity technique to enhance the optical satellite system in the presence of the cloud and atmospheric turbulence. In this dissertation, we also provide insightful discussions that can be helpful for the practical system design of satellite-based FSO communications.

## 6.2. Future Research

For future directions, we aim at expanding the current research to explore new mitigation techniques that address the challenging issues of optical satellite communication in the new space era. In recent years, space organizations, i.e., OneWeb, SpaceX, have started a project, Global Information Grid (GIG), built on a space-aerial-ground integrated network (SAGIN). Thanks to the inherent advantages in terms of large coverage, high throughput, and strong resilience, SAGIN can be used in many practical fields, including earth observation and mapping, the intelligent transportation system (ITS), military mission, disaster rescue, and so on. Unlike traditional terrestrial networks, SAGIN is affected by limitations simultaneously from all three segments, from the aspects of traffic distribution, load balancing, mobility management, power allo-



cation, route scheduling, end-to-end quality of service (QoS) requirements, etc. Thus, it is critically necessary for system design to achieve optimal performance in end-to-end data transmission given various practical network resource constraints from each segment. Based on current achievements, future research can be expanded to the following areas:

- Acquisition, tracking, and pointing (ATP) mechanism is a critical component for a wide variety of use cases of mobile FSO communications. ATP mechanisms are used to align an FSO transmitter and receiver to attain line-of-sight, which is required for the effective operation of FSO communications. In the context of SAGIN, ATP mechanisms are expected to decrease in size and complexity to save energy consumption for moving terminals (e.g., battery-powered drones). To advance this research direction, we plan to address two critical questions: (1) among many mechanisms types: gimbal-based, mirror-based, adaptive-optics, RIS-based, hybrid FSO/RF-based, what are the effective mechanisms for ATP system? And (2) how can those mechanisms be used to design efficient solutions for SAGIN.
- Reinforcement learning (RL) is a promising technique for SAGIN due to does not require labeled datasets like machine learning (supervised and unsupervised). RL can learn from prior experience and seems more suitable for a dynamic wireless network like SAGIN. In SAGIN, the channel state information (CSI) is importation information that describes how the signal propagates through the environmental conditions. The accuracy of CSI estimation can help limit bit error rate and select modulation schemes, especially in SAGIN using rate adaptation for hybrid FSO/RF systems. In particular, the transmitter (satellite) transmits a pilot signal for estimating the CSI and uses the estimated CSI dataset to train and estimate the remaining channels and future CSI using RL. In this context, several promising uses-cases to investigate the application of the RL technique include: (i) adaptive data rate/power for the hybrid FSO/RF in SAGIN, (ii) adaptive beamforming to enhance the performance of multi-beam

satellites, and (iii) monitoring applications.

# Bibliography

- [1] Y. Shi and J. Liu, “Inter-segment gateway selection for transmission energy optimization in space-air-ground converged network,” in *2018 IEEE International Conference on Communications (ICC)*, pp. 1–6, 2018.
- [2] J. Takashi, “Optical inter-orbit communication experiment between oicets and artemis.” Accessed: May 24, 2022. [Online]. Available: <https://www.nict.go.jp>.
- [3] F. Fidler, M. Knappek, J. Horwath, and W. R. Leeb, “Optical communications for high-altitude platforms,” *IEEE J. Sel. Topics. Quantum Electron.*, vol. 16, no. 5, pp. 1058–1070, Sept.-Oct. 2010.
- [4] J. A. E. Agency, N. I. of Information, C. Technology, and S. C. S. Laboratories, “Small optical link for international space station (soliss) succeeds in bidirectional laser communication between space and ground station-optical ground station receives high-definition images from the international space station via ethernet-.” Accessed: May 24, 2022. [Online]. Available: <https://global.jaxa.jp>.
- [5] H. Hemmati, *Near-Earth Laser Communications*. Boca Raton, FL: CRC Press, 2nd ed., 2021.
- [6] A. Carrasco-Casado and R. Mata-Calvo, *Free-space optical link for space communication network*. Springer, 1st ed., 2020.

- [7] T. V. PHAM and A. T. PHAM, “Performance of apd-based amplify-and-forward relaying fso systems over atmospheric turbulence channels,” *IEICE Transactions on Fundamentals of Electronics, Communications and Computer Sciences*, vol. E99.A, no. 7, pp. 1455–1464, 2016.
- [8] K. Suzuki, D. R. Kolev, A. Carrasco-Casado, and M. Toyoshima, “Environmental-data collection system for satellite-to-ground optical communications,” *Trans. JSASS Aerospace Tech. Japan*, vol. 16, no. 1, pp. 35–39, 2018.
- [9] M. Handley, “Delay is not an option: Low latency routing in space,” in *Proc. 17th ACM Workshop Hot Topics Netw. (HotNets)*, pp. 85 – 91, Association for Computing Machinery, New York, United States, 2018.
- [10] I. del Portillo, B. G. Cameron, and E. F. Crawley, “A technical comparison of three low earth orbit satellite constellation systems to provide global broadband,” in *Acta Astronautica*, vol. 159, pp. 123 – 135, Association for Computing Machinery, New York, United States, 2019.
- [11] R. Fields, C. Lunde, R. Wong, J. Wicker, D. Kozlowski, J. Jordan, B. Hansen, G. Muehlnikel, W. Scheel, U. Sterr, R. Kahle, and R. Meyer, “NFIRE-to-TerraSAR-X laser communication results: satellite pointing, disturbances, and other attributes consistent with successful performance,” in *Sensors and Systems for Space Applications III*, vol. 7330, pp. 211 – 225, International Society for Optics and Photonics, SPIE, 2009.
- [12] S. Seel, H. Kämpfner, F. Heine, D. Dallmann, G. Muehlnikel, M. Gregory, M. Reinhardt, K. Saucke, J. Muckherjee, U. Sterr, B. Wandernoth, R. Meyer, and R. Czichy, “Space to ground bidirectional optical communication link at 5.6 gbps and edrs connectivity outlook,” in *2011 Aerospace Conference*, pp. 1–7, 2011.

- [13] I. Mcketta, “How starlink’s satellite internet stacks up against hughesnet and viasat aound the globe.” Global speeds, Aug. 04, 2021.
- [14] B. S. Robinson, D. M. Boroson, C. M. Schieler, F. I. Khatri, O. Guldner, S. Constantine, T. Shih, J. W. Burnside, B. C. Bilyeu, F. Hakimi, A. Garg, G. Allen, E. Clements, and D. M. Cornwell, “Terabyte infrared delivery (tbird): a demonstration of large-volume direct-to-earth data transfer from low-earth orbit,” in *Free-Space Laser Communication and Atmospheric Propagation XXX*, vol. 10524, pp. 253 – 258, International Society for Optics and Photonics, SPIE, 2018.
- [15] L. D. Hoang, P. V. Trinh, T. V. Pham, D. Kolev, C.-C. Alberto, K.-O. Toshihiro, M. Toyoshima, and A. T. Pham, “Throughput analysis for tcp over the fso-based satellite-assisted internet of vehicles,” *IEEE Transactions on Vehicular Technology*, pp. 1–1, 2021.
- [16] A. U. Chaudhry and H. Yanikomeroglu, “Free space optics for next-generation satellite networks,” *IEEE Consumer Electronics Magazine*, vol. 10, no. 6, pp. 21–31, 2021.
- [17] T. V. Nguyen, T. V. Pham, N. T. Dang, and A. T. Pham, “Performance of generalized qam/fso systems with pointing misalignment and phase error over atmospheric turbulence channels,” *IEEE Access*, vol. 8, pp. 203631–203644, 2020.
- [18] H. D. Le and A. T. Pham, “Level crossing rate and average fade duration of satellite-to-uav fso channels,” *IEEE Photonics Journal*, vol. 13, no. 1, pp. 1–14, 2021.
- [19] T. V. Nguyen, T. V. Pham, N. T. Dang, and A. T. Pham, “Uav-based fso systems using sc-qam signaling over fading channels with misalignment,” in *2020 IEEE 92nd Vehicular Technology Conference (VTC2020-Fall)*, pp. 1–5, 2020.

- [20] 3GPP, “3rd generation partnership project; technical specification group radio access network; study on new radio access technology: Radio access architecture and interfaces, v14.0.0.” 3rd Generation Partnership Project, Sophia Antipolis, France, Mar., 2017.
- [21] I. T. U. (ITU), “Strategic plan for the union for 2020-2023.” ITU, Dubai, May, 2018.
- [22] ESA, “A world first data transmission between european satellites using laser light.” Accessed, Sept, 14 2020.
- [23] B. Thompson, “Falcon fast, far, and first.” Accessed, Sept, 14 2020.
- [24] F. S. et al, “Lasercube optical communication terminal for nano and micro satellites,” *Acta Astronautica*, vol. 173, pp. 310–319, Aug., 2020.
- [25] H. D. Le, T. V. Nguyen, and A. T. Pham, “Cloud attenuation statistical model for satellite-based FSO communications,” *IEEE Antennas Wireless Propag. Lett.*, vol. 20, no. 5, pp. 643–647, Feb. 2021.
- [26] L. C. Andrews and R. L. Phillips, *Laser Beam Propagation through Random Media*. Bellingham, WA: SPIE Press, 2nd ed., 2005.
- [27] ECMWF, “ERA-interim database.” Accessed: 19-11-2020. [Online]. Available: <https://apps.ecmwf.int/datasets/data/interim-full-daily>.
- [28] Cisco, “Cisco global cloud index: Forecast and methodology, 2015-2020.” White paper, 2016.
- [29] K.-C. Chen, T. Zhang, R. D. Gitlin, and G. Fettweis, “Ultra-low latency mobile networking,” *IEEE Network*, vol. 33, no. 2, pp. 181–187, 2019.
- [30] U. N. O. of Outer Space Affairs, “Online index of objects launched into outer space.” Accessed: May 24, 2022. [Online]. Available: <https://www.unoosa.org/oosa/osoindex/search-ng.jsp>.

- [31] U. of Concerned Scientists (UCS), “Ucs satellite database.” Accessed: May 24, 2022. [Online]. Available: <https://www.ucsusa.org/resources/satellite-database>.
- [32] A. Murtaza, S. J. H. Pirzada, T. Xu, and L. Jianwei, “Orbital debris threat for space sustainability and way forward (review article),” *IEEE Access*, vol. 8, pp. 61000–61019, 2020.
- [33] I. F. Akyildiz, A. Kak, and S. Nie, “6g and beyond: The future of wireless communications systems,” *IEEE Access*, vol. 8, pp. 133995–134030, 2020.
- [34] G. MARAL, M. BOUSQUET, and Z. SUN, *Satellite Communications Systems: Systems, Techniques and Technology*. John Wiley & Sons Ltd., 6th ed., 2020.
- [35] O. Kodheli, E. Lagunas, N. Maturo, S. K. Sharma, B. Shankar, J. F. M. Montoya, J. C. M. Duncan, D. Spano, S. Chatzinotas, S. Kisseleff, J. Querol, L. Lei, T. X. Vu, and G. Goussetis, “Satellite communications in the new space era: A survey and future challenges,” *IEEE Communications Surveys Tutorials*, vol. 23, no. 1, pp. 70–109, 2021.
- [36] J. Farserotu and R. Prasad, “A survey of future broadband multimedia satellite systems, issues and trends,” *IEEE Communications Magazine*, vol. 38, no. 6, pp. 128–133, 2000.
- [37] A. Gharanjik, B. Shankar M. R., P.-D. Arapoglou, and B. Ottersten, “Multiple gateway transmit diversity in q/v band feeder links,” *IEEE Transactions on Communications*, vol. 63, no. 3, pp. 916–926, 2015.
- [38] G. Avdikos, G. Papadakis, and N. Dimitriou, “Overview of the application of high altitude platform (hap) systems in future telecommunication networks,” in *2008 10th International Workshop on Signal Processing for Space Communications*, pp. 1–6, 2008.
- [39] V. Cazaubiel, G. Planche, V. Chorvalli, L. L. Hors, B. Roy, E. Giraud, L. Vailon, F. Carre, and E. Decourbey, “LOLA: a 40.000 km optical link between

- an aircraft and a geostationary satellite,” in *International Conference on Space Optics — ICSSO 2006* (E. Armandillo, J. Costeraste, and N. Karafolas, eds.), vol. 10567, pp. 527 – 533, International Society for Optics and Photonics, SPIE, 2017.
- [40] J. Horwath, M. Knapek, B. Epple, M. Brechtelsbauer, and B. Wilkerson, “Broadband backhaul communication for stratospheric platforms: the stratospheric optical payload experiment (STROPEX),” in *Free-Space Laser Communications VI* (A. K. Majumdar and C. C. Davis, eds.), vol. 6304, pp. 436 – 447, International Society for Optics and Photonics, SPIE, 2006.
- [41] M. Mozaffari, W. Saad, M. Bennis, Y.-H. Nam, and M. Debbah, “A tutorial on uavs for wireless networks: Applications, challenges, and open problems,” *IEEE Communications Surveys Tutorials*, vol. 21, no. 3, pp. 2334–2360, 2019.
- [42] A. Fotouhi, H. Qiang, M. Ding, M. Hassan, L. G. Giordano, A. Garcia-Rodriguez, and J. Yuan, “Survey on uav cellular communications: Practical aspects, standardization advancements, regulation, and security challenges,” *IEEE Communications Surveys Tutorials*, vol. 21, no. 4, pp. 3417–3442, 2019.
- [43] M. Li, Y. Hong, C. Zeng, Y. Song, and X. Zhang, “Investigation on the uav-to-satellite optical communication systems,” *IEEE Journal on Selected Areas in Communications*, vol. 36, no. 9, pp. 2128–2138, 2018.
- [44] C.-C. Chen and J. R. Lesh, “Overview of the Optical Communications Demonstrator,” in *Free-Space Laser Communication Technologies VI* (G. S. Mecherle, ed.), vol. 2123, pp. 85 – 94, International Society for Optics and Photonics, SPIE, 1994.
- [45] A. Biswas, F. Khatri, and D. Boroson, “Near-sun free-space optical communications from space,” in *2006 IEEE Aerospace Conference*, pp. 9 pp.–, 2006.



- [46] Z. Sodnik, B. Furch, and H. Lutz, “Optical intersatellite communication,” *IEEE Journal of Selected Topics in Quantum Electronics*, vol. 16, no. 5, pp. 1051–1057, 2010.
- [47] J. M. Perdignes, Z. Sodnik, H. Hauschildt, P. Sarasa, F. Porte-Proust, M. Wiegand, C. Rochow, D. Troendle, and F. Heine, “The ESA’s optical ground station for the EDRS-A LCT in-orbit test campaign: upgrades and test results,” in *International Conference on Space Optics — ICSO 2016* (B. Cugny, N. Karafolas, and Z. Sodnik, eds.), vol. 10562, pp. 833 – 841, International Society for Optics and Photonics, SPIE, 2017.
- [48] C. Chen, A. Grier, M. Malfa, E. Booen, H. Harding, C. Xia, M. Hunwardsen, J. Demers, K. Kudinov, G. Mak, B. Smith, A. Sahasrabudhe, F. Patawaran, T. Wang, A. Wang, C. Zhao, D. Leang, J. Gin, M. Lewis, B. Zhang, D. Nguyen, D. Jandrain, F. Haque, and K. Quirk, “Demonstration of a bidirectional coherent air-to-ground optical link,” in *Free-Space Laser Communication and Atmospheric Propagation XXX* (H. Hemmati and D. M. Boroson, eds.), vol. 10524, pp. 120 – 134, International Society for Optics and Photonics, SPIE, 2018.
- [49] N. Perlot, T. Dreischer, C. M. Weinert, and J. Perdignes, “2012 future network mobile summit (futurenetw),” pp. 1–8, 2012.
- [50] B. L. Edwards, B. Robinson, A. Biswas, and J. Hamkins, “An overview of nasa’s latest efforts in optical communications,” in *2015 IEEE International Conference on Space Optical Systems and Applications (ICSOS)*, pp. 1–8, 2015.
- [51] N. Perlot, “Turbulence-induced fading probability in coherent optical communication through the atmosphere,” *Appl. Opt.*, vol. 46, pp. 7218–7226, Oct 2007.
- [52] A. Carrasco-Casado, H. Takenaka, D. Kolev, Y. Munemasa, H. Kunimori, K. Suzuki, T. Fuse, T. Kubo-Oka, M. Akioka, Y. Koyama, and M. Toyoshima, “Leo-to-ground optical communications using sota (small optical transponder)

- payload verification results and experiments on space quantum communications,” *Acta Astronautica*, vol. 139, pp. 377–384, 2017.
- [53] A. S. Hamza, J. S. Deogun, and D. R. Alexander, “Classification framework for free space optical communication links and systems,” *IEEE Communications Surveys Tutorials*, vol. 21, no. 2, pp. 1346–1382, 2019.
- [54] Z. Ghassemlooy, W. Popoola, and S. Rajbhandari, *Optical Wireless Communications: System and Channel Modelling with MATLAB*. FL, USA: CRC Press, Inc.: Boca Raton, 1st ed., 2012.
- [55] H. A. Willebrand and B. S. Ghuman, *Free Space Optics: Enabling Optical Connectivity in Today’s Networks*. USA: Sams publishing, 1st ed., 2001.
- [56] O. Bouchet, H. Sizun, C. Boisrobert, F. de Fornel, and P.-N. Favennec, *Free-Space Optics: Propagation and Communication*. John Wiley & Sons, Ltd, 1st ed., 2006.
- [57] H. Kaushal and G. Kaddoum, “Optical communication in space: Challenges and mitigation techniques,” *IEEE Communications Surveys Tutorials*, vol. 19, no. 1, pp. 57–96, 2017.
- [58] M. A. Khalighi and M. Uysal, “Survey on free space optical communication: A communication theory perspective,” *IEEE Commun. Surveys Tuts.*, vol. 16, no. 4, pp. 2231–2258, 2014.
- [59] I. E. Lee, Z. Ghassemlooy, W. P. Ng, and M.-A. Khalighi, “Joint optimization of a partially coherent gaussian beam for free-space optical communication over turbulent channels with pointing errors,” *Opt. Lett.*, vol. 38, pp. 350–352, Feb 2013.
- [60] A. G. Kanatas and A. D. Panagopoulos, *Radio Wave Propagation and Channel Modeling for Earth-Space Systems*. Taylor & Francis Group: CRC Press, 1st ed., 2016.

- [61] A. Al-Habash, L. C. Andrews, and R. L. Phillips, “Mathematical model for the irradiance probability density function of a laser beam propagating through turbulent media,” *Optical Engineering*, vol. 40, no. 8, pp. 1554 – 1562, 2001.
- [62] S. Karapantazis and F. Pavlidou, “Broadband communications via high-altitude platforms: A survey,” *IEEE Communications Surveys Tutorials*, vol. 7, no. 1, pp. 2–31, 2005.
- [63] R. Swaminathan, S. Sharma, and A. S. MadhuKumar, “Performance analysis of haps-based relaying for hybrid fso/rf downlink satellite communication,” in *2020 IEEE 91st Vehicular Technology Conference (VTC2020-Spring)*, pp. 1–5, 2020.
- [64] S. R., S. Sharma, N. Vishwakarma, and A. Madhukumar, “Haps-based relaying for integrated space-air-ground networks with hybrid fso/rf communication : A performance analysis,” *IEEE Transactions on Aerospace and Electronic Systems*, pp. 1–1, 2021.
- [65] S. Shah, M. Siddharth, N. Vishwakarma, R. Swaminathan, and A. S. Madhukumar, “Adaptive-combining-based hybrid FSO/RF satellite communication with and without HAPS,” *IEEE Access*, vol. 9, pp. 81492–81511, Jun. 2021.
- [66] O. Ben yahia, E. Erdogan, G. Karabulut Kurt, I. Altunbas, and H. Yanikomeroglu, “Haps selection for hybrid rf/fso satellite networks,” *IEEE Transactions on Aerospace and Electronic Systems*, pp. 1–1, 2022.
- [67] T. V. Nguyen, H. D. Le, N. T. Dang, and A. T. Pham, “On the design of rate adaptation for relay-assisted satellite hybrid fso/rf systems,” *IEEE Photonics Journal*, pp. 1–1, 2021.
- [68] T. V. Nguyen, H. D. Le, N. T. Dang, and A. T. Pham, “Average transmission rate and outage performance of relay-assisted satellite hybrid FSO/RF systems,” in *Proc. IEEE Int. Conf. Adv. Technol. Commun.*, pp. 1–6, 2021.

- 
- [69] H. Jia, J. Zhong, M. N. Janardhanan, and G. Chen, "Ergodic capacity analysis for FSO communications with UAV-equipped IRS in the presence of pointing error," in *IEEE Int. Conf. Commun. Technol.*, pp. 949–954, 2020.
- [70] S. Malik, P. Saxena, and Y. H. Chung, "Performance analysis of a UAV-based IRS-assisted hybrid RF/FSO link with pointing and phase shift errors," *IEEE/OSA J. Opt. Commun. Netw.*, vol. 14, no. 4, pp. 303–315, Apr. 2022.
- [71] P. Saxena and Y. H. Chung, "On the performance of all-optical RORIS dual hop UAV based FSO systems," *KICS ICT Exp.*, Apr. 2022 (Accepted).
- [72] T. V. Nguyen, H. D. Le, and A. T. Pham, "On the design of ris-uav relay-assisted hybrid fso/rf satellite-aerial-ground integrated network." Available: <https://doi.org/10.36227/techrxiv.19761493.v1>.
- [73] Y. Kaymak, R. Rojas-Cessa, J. Feng, N. Ansari, M. Zhou, and T. Zhang, "A survey on acquisition, tracking, and pointing mechanisms for mobile free-space optical communications," *IEEE Communications Surveys Tutorials*, vol. 20, no. 2, pp. 1104–1123, 2018.
- [74] F. Nadeem, V. Kvicera, M. S. Awan, E. Leitgeb, S. S. Muhammad, and G. Kandalus, "Weather effects on hybrid FSO/RF communication link," *IEEE J. Sel. Areas Commun.*, vol. 27, no. 9, pp. 1687–1697, 2009.
- [75] M. Usman, H.-C. Yang, and M.-S. Alouini, "Practical switching-based hybrid FSO/RF transmission and its performance analysis," *IEEE Photonics Journal*, vol. 6, no. 5, pp. 1–13, 2014.
- [76] H. Wu and M. Kavehrad, "Availability evaluation of ground-to-air hybrid FSO/RF links," *J. Wireless Inf. Netw. (Springer)*, vol. 14, no. 1, pp. 1572–8129, 2007.
- [77] M. Usman, H.-C. Yang, and M.-S. Alouini, "Practical switching-based hybrid fso/rf transmission and its performance analysis," *IEEE Photonics Journal*, vol. 6, no. 5, pp. 1–13, 2014.

- [78] S. Sharma, A. S. Madhukumar, and R. Swaminathan, "Switching-based cooperative decode-and-forward relaying for hybrid fso/rf networks," *Journal of Optical Communications and Networking*, vol. 11, no. 6, pp. 267–281, 2019.
- [79] R. Swaminathan, S. Sharma, and A. S. MadhuKumar, "Performance analysis of HAPS-based relaying for hybrid FSO/RF downlink satellite communication," in *Proc. IEEE Veh. Technol. Conf.*, pp. 1–5, 2020.
- [80] T. Rakia, H.-C. Yang, M.-S. Alouini, and F. Gebali, "Outage analysis of practical fso/rf hybrid system with adaptive combining," *IEEE Communications Letters*, vol. 19, no. 8, pp. 1366–1369, 2015.
- [81] T. Rakia, H.-C. Yang, F. Gebali, and M.-S. Alouini, "Power adaptation based on truncated channel inversion for hybrid fso/rf transmission with adaptive combining," *IEEE Photonics Journal*, vol. 7, no. 4, pp. 1–12, 2015.
- [82] W. M. R. Shakir, "Performance evaluation of a selection combining scheme for the hybrid fso/rf system," *IEEE Photonics Journal*, vol. 10, no. 1, pp. 1–10, 2018.
- [83] T. Rakia, H.-C. Yang, M.-S. Alouini, and F. Gebali, "Outage analysis of practical FSO/RF hybrid system with adaptive combining," *IEEE Commun. Lett.*, vol. 19, no. 8, pp. 1366–1369, 2015.
- [84] V. Singh, S. Solanki, P. K. Upadhyay, D. B. da Costa, and J. M. Moualeu, "Performance analysis of hardware-impaired overlay cognitive satellite-terrestrial networks with adaptive relaying protocol," *IEEE Syst. J.*, vol. 15, no. 1, pp. 192–203, Mar. 2021.
- [85] "Measuring digital development. facts and figures 2019." Technical Report International Telecommunication Union (ITU), 2019.
- [86] I. del Portillo, S. Eiskowitz, E. F. Crawley, and B. G. Cameron, "Connecting the other half: Exploring options for the 50% of the population unconnected to the internet," *Telecomm. Policy*, vol. 45, no. 3, pp. 1–34, Apr. 2021.

- [87] SpaceX, “Starlink.” Accessed: Aug. 2021. [Online]. Available: <https://en.wikipedia.org/wiki/Starlink>.
- [88] J. Ye, S. Dang, B. Shihada, and M.-S. Alouini, “Space-air-ground integrated networks: Outage performance analysis,” *IEEE Trans. Wireless Commun.*, vol. 19, no. 12, pp. 7897–7912, Dec. 2020.
- [89] N. Saeed, H. Almorad, H. Dahrouj, T. Y. Al-Naffouri, J. S. Shamma, and M.-S. Alouini, “Point-to-point communication in integrated satellite-aerial 6G networks: State-of-the-art and future challenges,” *IEEE Open J. Commun. Soc.*, pp. 1–1, Jun. 2021.
- [90] S. C. Arum, D. Grace, and P. D. Mitchell, “A review of wireless communication using high-altitude platforms for extended coverage and capacity,” *Comput. Commun.*, vol. 157, pp. 232–256, May 2020.
- [91] Softbank, “HAPS mobile.” Accessed: Aug. 2021. [Online]. Available: <https://www.hapsmobile.com>.
- [92] L. Gupta, R. Jain, and G. Vaszkun, “Survey of important issues in UAV communication networks,” *IEEE Commun. Surveys Tutorials*, vol. 18, no. 2, pp. 1123–1152, Secondquarter 2016.
- [93] M. Li, Y. Hong, C. Zeng, Y. Song, and X. Zhang, “Investigation on the UAV-to-satellite optical communication systems,” *IEEE J. Sel. Areas Commun.*, vol. 36, no. 9, pp. 2128–2138, Sept. 2018.
- [94] J. Ma, K. Li, L. Tan, S. Yu, and Y. Cao, “Performance analysis of satellite-to-ground downlink coherent optical communications with spatial diversity over gamma gamma atmospheric turbulence,” *IEEE/OSA Appl. Opt.*, vol. 54, no. 25, pp. 7575–7585, Sept. 2015.
- [95] M. Usman, H.-C. Yang, and M.-S. Alouini, “Practical switching-based hybrid FSO/RF transmission and its performance analysis,” *IEEE Photon. J.*, vol. 6, no. 5, pp. 1–13, Oct. 2014.

- [96] E. Zedini, H. Soury, and M.-S. Alouini, “Dual-hop FSO transmission systems over gamma-gamma turbulence with pointing errors,” *IEEE Trans. Wireless Commun.*, vol. 16, no. 2, pp. 784–796, Feb. 2017.
- [97] S. Sharma, A. S. Madhukumar, and R. Swaminathan, “Switching-based cooperative decode-and-forward relaying for hybrid FSO/RF networks,” *IEEE/OSA J. Optical Commun. Netw.*, vol. 11, no. 6, pp. 267–281, Jun. 2019.
- [98] M. Siddharth, S. Shah, and S. R., “Outage analysis of adaptive combining scheme for hybrid FSO/RF communication,” in *Proc. Nat. Conf. Commun.*, pp. 1–6, 2020.
- [99] H. D. Le and A. T. Pham, “Level crossing rate and average fade duration of satellite-to-UAV FSO channels,” *IEEE Photon. J.*, vol. 13, no. 1, pp. 1–14, Feb. 2021.
- [100] J. Li, Y. Yao, G. Wu, J. Hou, W. Yu, B. Liu, and J. Liu, “Broadband laser doppler frequency shift emulator for satellite laser communication,” *IEEE Photon. J.*, vol. 11, no. 6, pp. 1–12, Nov. 2019.
- [101] F. Yang, J. Cheng, and T. A. Tsiftsis, “Free-space optical communication with nonzero boresight pointing errors,” *IEEE Transactions on Communications*, vol. 62, no. 2, pp. 713–725, 2014.
- [102] International Telecommunication Union (ITU), “Attenuation due to clouds and fog.” document Rec. ITU-R P-840-6, 2013.
- [103] M. Simon and M.-S. Alouini, *Digital Communication over Fading Channels, 2nd Edition*. Wiley Publishers, 2005.
- [104] P. V. Trinh, T. Cong Thang, and A. T. Pham, “Mixed mmwave rf/fso relaying systems over generalized fading channels with pointing errors,” *IEEE Photonics Journal*, vol. 9, no. 1, pp. 1–14, 2017.

- 
- [105] E. Erdogan, I. Altunbas, G. K. Kurt, M. Bellemare, G. Lamontagne, and H. Yanikomeroglu, "Site diversity in downlink optical satellite networks through ground station selection," *IEEE Access*, vol. 9, pp. 31179–31190, Feb. 2021.
- [106] T. V. Nguyen, H. D. Le, T. V. Pham, and A. T. Pham, "Link availability of satellite-based FSO communications in the presence of clouds and turbulence," *IEICE Commun. Exp.*, vol. 10, Feb. 2021.
- [107] M. Alzenad, M. Z. Shakir, H. Yanikomeroglu, and M.-S. Alouini, "FSO-based vertical backhaul/fronthaul framework for 5G+ wireless networks," *IEEE Commun. Mag.*, vol. 56, no. 1, pp. 218–224, Jan. 2018.
- [108] M. Q. Vu, T. V. Pham, N. T. Dang, and A. T. Pham, "Outage performance of HAP-UAV FSO links with gaussian beam and UAV hovering," in *Proc. IEEE Veh. Technol. Conf.*, pp. 1–5, 2020.
- [109] A. Prudnikov, Y. Brychkov, and O. Marichev, *Integrals, and series: volume 3 more special function.*, vol. 3. Gordon and Breach Science Publishers, 1986.
- [110] V. Adamchik and O. Marichev, "The algorithm for calculating integrals of hypergeometric type functions and its realization in reduce system," in *Proc. Int. Conf. Symb. Algebraic Comput.*, pp. 212–224, 1990.
- [111] L. Paillier, R. Le Bidan, J.-M. Conan, G. Artaud, N. Vedrenne, and Y. Jaouen, "Space-ground coherent optical links: Ground receiver performance with adaptive optics and digital phase-locked loop," *J. Lightw. Technol.*, vol. 38, no. 20, pp. 5716–5727, Jun. 2020.
- [112] R. Shah and J. L. Garrison, "Application of the ICF coherence time method for ocean remote sensing using digital communication satellite signals," *IEEE J. Sel. Topics Appl. Earth Observations Remote Sens.*, vol. 7, no. 5, pp. 1584–1591, May 2014.



- [113] V. V. Mai and A. T. Pham, “Cross-layer designs and analysis of adaptive-rate transmission and ARQ for free-space optical communications,” *IEEE Photon. J.*, vol. 8, no. 1, pp. 1–15, Feb. 2016.
- [114] F. Peng, J. Zhang, and W. E. Ryan, “Adaptive modulation and coding for IEEE 802.11n,” in *Proc. IEEE Wireless Commun. Netw. Conf.*, pp. 656–661, 2007.
- [115] M. Z. Chowdhury, M. K. Hasan, M. Shahjalal, M. T. Hossan, and Y. M. Jang, “Optical wireless hybrid networks: Trends, opportunities, challenges, and research directions,” *IEEE Commun. Surveys Tuts.*, vol. 22, no. 2, pp. 930–966, Jan. 2020.
- [116] V. Jamali, H. Ajam, M. Najafi, B. Schmauss, R. Schober, and H. V. Poor, “Intelligent reflecting surface assisted free-space optical communications,” *IEEE Commun. Mag.*, vol. 59, no. 10, pp. 57–63, Oct. 2021.
- [117] E. Zedini, H. Soury, and M.-S. Alouini, “On the performance analysis of dual-hop mixed FSO/RF systems,” *IEEE Trans. Wireless Commun.*, vol. 15, no. 5, pp. 3679–3689, Feb. 2016.
- [118] A. R. Ndjiongue, T. M. N. Ngatched, O. A. Dobre, A. G. Armada, and H. Haas, “Analysis of ris-based terrestrial-fso link over g-g turbulence with distance and jitter ratios,” *Journal of Lightwave Technology*, vol. 39, no. 21, pp. 6746–6758, 2021.
- [119] V. Singh, S. Solanki, P. K. Upadhyay, D. B. da Costa, and J. M. Moualeu, “Performance analysis of hardware-impaired overlay cognitive satellite-terrestrial networks with adaptive relaying protocol,” *IEEE Syst. J.*, vol. 15, no. 1, pp. 192–203, 2021.
- [120] H. D. Nguyen, H. D. Le, C. T. Nguyen, and A. T. Pham, “Throughput and delay performance of cooperative HARQ in satellite-HAP-vehicle FSO systems,” in *Proc. IEEE Veh. Tech. Conf.*, pp. 1–6, 2021.

- [121] L. D. Hoang, P. V. Trinh, T. V. Pham, D. Kolev, C.-C. Alberto, K.-O. Toshihiro, M. Toyoshima, and A. T. Pham, “Throughput analysis for TCP over the FSO-based satellite-assisted internet of vehicles,” *IEEE Trans. Veh. Tech.*, pp. 1–1, Dec. 2021.
- [122] A. R. Ndjiongue, T. M. N. Ngatched, O. A. Dobre, and H. Haas, “Design of a power amplifying-RIS for free-space optical communication systems,” *IEEE Wireless Commun.*, vol. 28, no. 6, pp. 152–159, Dec. 2021.
- [123] M. Najafi, B. Schmauss, and R. Schober, “Intelligent reflecting surfaces for free space optical communication systems,” *IEEE Trans. Commun.*, vol. 69, no. 9, pp. 6134–6151, Sept. 2021.
- [124] I. S. Gradshteyn and I. M. Ryzhik, *Table of Integrals, Series, and Products, 7th Edition*. New York: Academic, 2007.
- [125] M. Abramowitz and I. A. Stegun, *Handbook of Mathematical Functions, With Formulas, Graphs, and Mathematical Tables*. New York, USA: Dover, 9th ed., 1972.
- [126] H. D. Le, V. V. Mai, C. T. Nguyen, and A. T. Pham, “Throughput analysis of incremental redundancy hybrid ARQ for FSO-based satellite systems,” in *IEEE Veh. Tech. Conf.*, pp. 1–5, 2019.
- [127] D. R. Kolev, A. Carrasco-Casado, K. Suzuki, and M. Toyoshima, “Environmental-data collection system testbed for site-diversity implementation in satellite-to-ground laser communications,” in *2017 IEEE International Conference on Space Optical Systems and Applications (ICSOS)*, pp. 286–289, 2017.
- [128] N. K. Lyras, C. N. Efrem, C. I. Kourogiorgas, and A. D. Panagopoulos, “Optimum monthly based selection of ground stations for optical satellite networks,” *IEEE Commun. Lett.*, vol. 22, no. 6, pp. 1192–1195, 2018.

- [129] N. K. Lyras, C. N. Efrem, C. I. Kourogiorgas, A. D. Panagopoulos, and P.-D. Arapoglou, “Optimizing the ground network of optical meo satellite communication systems,” *IEEE Systems Journal*, vol. 14, no. 3, pp. 3968–3976, 2020.
- [130] N. K. Lyras, C. I. Kourogiorgas, and A. D. Panagopoulos, “Cloud free line of sight prediction modeling for optical satellite communication networks,” *IEEE Communications Letters*, vol. 21, no. 7, pp. 1537–1540, 2017.
- [131] D. Giggenbach and F. Moll, “Scintillation loss in optical low earth orbit data downlinks with avalanche photodiode receivers,” in *IEEE Int. Conf. on Space Opt. Sys.*, pp. 115–122, 2017.